HZB Helmholtz Zentrum Berlin

SCHRIFTENREIHE DES HZB · EXAMENSARBEITEN

A study of charge transfer kinetics in dye-sensitized surface conductivity solar cells

Dennis Friedrich

Dissertation

Institut für Solare Brennstoffe und Energiespeichermaterialien E-I6

Mai 2011

HZB–B 13

ISSN 1868-5781

doi: 10.5442/d0007

Helmholtz-Zentrum Berlin für Materialien und Energie · Hahn-Meitner-Platz 1 · D-14109 Berlin · Telefon +49 30 8062 0 · Telefax +49 30 8062 42181 · www.helmholtz-berlin.de

A study of charge transfer kinetics in dye-sensitized surface conductivity solar cells

Dissertation zur Erlangung des akademischen Grades des Doktors der Naturwissenschaften (Dr. rer. nat.)

eingereicht im Fachbereich Biologie, Chemie, Pharmazie der Freien Universität Berlin

vorgelegt von

Dennis Friedrich
aus Giessen

Berlin, Mai 2011

HZB Helmholtz Zentrum Berlin

gefördert durch das Stipendienprogramm der Deutschen Bundesstiftung Umwelt
DBU
Deutsche Bundesstiftung Umwelt
www.dbu.de

Freie Universität Berlin

1. Gutachter: Prof. Dr. E. Rühl

2. Gutachter: Prof. Dr. H. Tributsch

Disputation am:

Erklärung der Selbstständigkeit

Hiermit versichere ich, die vorliegende Arbeit selbstständig verfasst und keine anderen als die angegebenen Quellen und Hilfsmittel benutzt zu haben.

Berlin, 31. Mai 2011 Dennis Friedrich

Contents

1 Introduction

Solar energy is a decentralized and unlimited natural resource, where the amount of energy reaching the surface of the earth in one hour (4.3 x 10^{20} J) is more than all energy consumed by humans in an entire year (4.1 x 10^{20} J) [1]. However, in 2010 the contribution of solar electricity to the final energy consumption in leading countries in solar energy, such as Germany was merely 2%, whereas the global share was even smaller [2].

Considering the rapid increase of the global carbon dioxide level in the atmosphere from 290 ppm to 390 ppm within the last 100 years and the effects on the world climate, measures to reduce greenhouse gas emissions have gained substantial attention within the last few years [3, 4]. The Intergovernmental Panel on Climate Change (IPCC) states in its latest report that the majority of additional CO_2 emissions is ascribed to the combustion of fossil fuels in the industry, in motor traffic, and in household heating [5]. Additionally, the rapidly increasing energy demands of newly industrialized countries such as China and India, as well as the population growth of many developing countries will lead to an increase of the world marketed energy consumption up to 50% by the year 2035 [6].

The continuous combustion of fossil fuels is not able to fulfill the requirements on a sustainable energy supply. Among renewable energy sources such as wind- and hydro power, photovoltaics (PV) is considered to be an innovative and trend-setting technology. Although the compound annual growth rate of the photovoltaic industry (44% in year 2002 - 2007) is impressive, especially in Germany, it requires further efforts in both science and industry to boost the contribution of solar energy to significant values.

Because of their complex and costly production methods, the currently used Si-based solar cells are not economically competitive at the moment and have to be subsidized extensively. Therefore, the development of cheaper alternatives to Si-based cell concepts is an incentive. Among the next generation solar cells,

Dye-Sensitized Solar Cells (DSC) have proven to be a promising new concept.

In contrast to conventionally used Si-based solar cells, the main advantages of DSC are the low-cost manufacturing process (non-purified starting material as compared to Si-cells), the use of titanium dioxide as a non-toxic supporting material, and the efficient generation of electricity even at diffuse light conditions.

Up to now, commercial implementation of this cell principle has failed due to (among others) the insufficient long term stability, which is particularly caused by the drying up and alteration of the liquid electrolyte, as well as the degradation of the dye.

One promising approach to overcome the stability problem and the intensive encapsulation cost of the cell involves the replacement of the liquid redox electrolyte by a solid-state electrolyte. However, so far these solid-state electrolytes limited the capabilities of kinetic charge separation and proved to be unstable as well [7]. A compromise with new prospects to optimization exists in the use of an electrolyte film on the nanoparticles for charge collection. With this alternative cell concept, the liquid electrolyte is replaced by a surface electrolyte film which at the same time avoids the use of toxic organic solvents (Nano Surface Conductivity Solar Cell (NSCSC), [8]).

Based on these previous studies, the aim of this work is to further develop and optimize the concept of the nano surface conductivity solar cell with the focus on a deepened understanding of the underlying kinetic processes within the cell.

2 Theoretical background

2.1 A brief history of photovoltaics

The process of converting sunlight directly into electricity is referred to as the photovoltaic effect. It was first observed by Becquerel in 1839, who found a light-dependent voltage between electrodes immersed in an electrolyte [9]. More than a century later, in 1954, the first silicon solar cell was fabricated incorporating the silicon p-n junction, with an initial efficiency of 6% [10].

The sensitization of a semiconductor electrode was first reported by Moser in 1887 [11]. Furthermore, the first photovoltaic effect in an organic crystal was observed by Kallman and Pope in 1959 [12]. The principle of power generation by dye-sensitized solar cells has been known since the pioneering work of Gerischer and Tributsch in the sixties and seventies [13, 14], wherein the introduction of nanoporous electrodes in 1990 by Grätzel improved the conversion efficiencies of the cell to about 7% [15]; thus, initiating extensive research activities on this cell concept.

2.2 Conventional solar cells

The conversion of light into electricity in a photovoltaic device relies on the formation of free electrons and holes upon light absorption. In a bulk crystalline semiconductor, the highest occupied and lowest unoccupied molecular orbitals (HOMO and LUMO) of constituent atoms or molecules converge into valence and conduction band (VB and CB). The Fermi level, E_F, is defined as the energy, at a given temperature, for which the probability of being occupied by an electron is 1/2. In the absence of dopants (*intrinsic* semiconductor), the energy level (Fermi level) of the semiconductor lies approximately half-way between the separation

gap of the valence and conduction band. Due to the low number of electrons in the CB as determined by the Fermi-Dirac distribution function, the conductivity is limited. However, the conductivity can be increased by doping. Doping with electron-donors (*n*-doping) makes the material electron-rich, and the Fermi level moves closer to the conduction band; since the majority carriers are in this case electrons, the semiconductor is then identified as *n*-type. Similarly, doping with electron-acceptors (*p*-doping) depletes the number of electrons available and the Fermi level moves closer to the valence band, rendering the semiconductor *p*-type. Optical excitation of the semiconductor with light of energy higher than the band gap leads to generation of free charge carriers, electrons (e^-) and holes (h^+).

When an *n*- and a *p*-type semiconductor are brought into contact, electrons diffuse from the *n*- to the *p*-type material; hence, leaving close to the junction a positive charge in the *n*-type semiconductor, and a negative charge in the *p*-type semiconductor. As a result of this displacement of charge, an electric field at the junction exists, which opposes the natural diffusion due to concentration gradients of charges in the materials. Consequently, a thermal equilibrium is reached where both Fermi levels are equal. In the dark, the Fermi level is the same for holes as for electrons. Under illumination, additional carriers are created, and the single Fermi level splits into two quasi-Fermi levels in the *n*-type or *p*-type region, where the higher the light intensity, the more they split. Close to the electrode, both quasi-Fermi levels collapse towards the majority quasi-Fermi level, where they are in contact. The shift of the Fermi levels in the electrodes represents the open circuit voltage, which can be approximated by the shift of the minority quasi-Fermi levels. Such separation of the charge carriers permits selective collection at the electrodes and a net conversion of sunlight into electric power [16–18].

The theoretical efficiency limit for an optimal single band gap photovoltaic device is 31%, because photons having energies lower than the absorption threshold of the semiconductor material are not absorbed, whereas photons with energies much higher than the band gap rapidly release heat to the lattice of the solid and therefore ultimately contain only a useful internal energy equal to that of the band gap [19].

In single-crystalline silicon solar cells, power conversion efficiencies of 25% on a laboratory scale were obtained [20]. However, for single-crystalline silicon solar cells to operate with high efficiency, photons have to be absorbed close to the

p-n interface. Charge carriers created farther away must diffuse to the p-n contact avoiding recombination. Therefore, the concentration of defects must be very small, imposing severe requirements on the purity of the material, making conventional type solid-state devices quite expensive. Although silicon is a relatively poor contestant for photovoltaic applications due to its small indirect band gap (1.1 eV), this material has been extensively applied, perhaps due to the knowledge gained from its wide application in semiconductor technology. The band gap value of a semiconductor is the first consideration in terms of its photovoltaic potential. A very small band gap will absorb many photons of a wide range of wavelengths, but with a low photovoltage. On the other hand, a large band gap allows a larger photovoltage, but since only photons with energies greater than the band gap are absorbed, the current will be lower. Since the purpose of a solar cell is to do electrical work, a compromise inherently exists between these two limiting cases [17].

Other materials with more favorable band gaps for photovoltaic applications include gallium arsenide, copper indium, indium phosphide and cadmium telluride. Due to their better absorptive properties, these materials can be manufactured into thinner films, which created the general term "thin-film solar cells" for any solar cell, which is not based on crystalline silicon. Thin films are typically prepared by methods such as physical or chemical vapor deposition, and electroplating. These preparation methods require lower energies than the ones to produce single crystalline solar cells; thus, the mass production of thin films may allow us to address the crucial issue of lowering production costs. However, there is a compromise between production costs and maximum efficiency, which is the lower quality of materials. Such materials present large amount of defects, which act as recombination centers. Thus, reducing the electron diffusion length and lifetime as well as increasing the resistivity. Furthermore, because of the complex defect chemistry available in thin film materials, most of them are not easily doped. Heterojunction thin-film solar cells contain an emitter made of a different material with a wider band gap, for example cadmium sulfide. The mismatch at the interface between the absorber and the emitter often creates additional recombination sites. Nonetheless, compared to the benchmark of single crystalline cells, Si (25%) and GaAs (27.6%) [20], thin-film solar cells with considerable efficiencies have been fabricated based on CdTe (16.7%) and Cu(In,Ga)(Se,S)$_2$ (19.6%).

2.3 Generations of photovoltaic solar cells

Based on the nature of the material, maximum conversion efficiency and associated cost of photovoltaic power, various photovoltaic solar cells have been grouped by Green in three major categories [21].

First generation photovoltaics apply the highest purity materials with few structural defects (such as single crystals). The highest power conversion efficiencies obtained to date are in first generation PV. However, the economics of this technology is dominated by the cost of its starting materials made in high volume and hence with little potential for cost reduction, such as silicon wafers, glass cover sheets, and other encapsulations. In addition to single component Si and layered semiconductors, binary semiconductors of II-IV and III-V have been examined.

Second generation of thin-film solar cell devices are based on low energy preparation techniques such as vapor deposition and electroplating. Regardless of the semiconductor involved, the thin-film technology offers prospects for a large reduction in material costs by eliminating the costs of the single crystalline silicon wafer preparation. However, the maximum power conversion is lower due to the presence of defects in the films.

Third generation photovoltaics refers to cell concepts that overcome the 31% theoretical upper limit of a single junction solar cell as defined by Shockley and Queisser [22]. For example, if photons having energies greater than the band gap of the absorbing material do not disspitate their excess energy as heat, but instead produce more voltage or generated multiple, low-energy, thermalized electrons from the energy of a single absorbed photon, theoretical efficiencies above 60% would, in principle, be attainable [19]. Based on theoretical analysis, several approaches have been proposed, such as hot carrier cells [23], multiple excitonic charge carrier generation [24] and multi-junction (tandem-type) solar cells [25]. Due to their excellent potential to deliver solar electric power at very low cost, solar cells based on dye sensitization are also referred to as third generation photovoltaics.

2.4 Dye sensitization of semiconductors

2.4.1 From sensitized bulk semiconductor electrodes to Dye-Sensitized Solar Cells (DSC)

The studies of dye sensitization of bulk semiconductor electrodes have laid the foundations for the development of dye-sensitized solar cells. Studies in this field include the pioneering work of Tributsch, Gerischer and Calvin who examined the photosensitization of ZnO using chlorophyll derivates as a model system for the primary process in photosynthesis [13, 14, 26]. Furthermore, the use of rose bengal dye onto a single crystal TiO_2 electrode by Spitler proved the excited-state charge injection between dye and semiconductor [27]. In general, photosensitization can occur via the transfer of the excitation energy to a suitable state/energy level of the acceptor or by electron transfer. The oxidation of the dye takes place via transfer of an electron from the excited energy level of the molecule to the conduction band of the semiconductor. When the semiconductor is used in an electrochemical cell as bulk electrodes, the excited-state charge injection is measured as photocurrent. Nonetheless, the currents generated by sensitization of single electrodes are very small because the dye is present only as a monolayer at the surface and light absorption is therefore very weak. An increase in surface area of a porous microcrystalline ZnO layer was demonstrated by Tsubomura et al. [28] to enable larger photocurrents compared to the flat surface of a single crystal. The use of a mesoporous layer of TiO_2 sensitized by a ruthenium dye reported by O'Regan and Grätzel triggered a boom in research activities on dye-sensitized solar cells by showing that an efficient ($> 7\%$) regenerative photoelectrochemical solar cell could be fabricated [15].

2.4.2 Efficiency parameters of a dye-sensitized solar cell

The spectral response of a dye-sensitized solar cell depends on the absorption properties of the dye. A DSC is characterized by a variety of experimental parameters, such as the photocurrent and photopotentials which are measured under different conditions (open and closed circuit): I_{OC}, V_{OC}, I_{SC} and V_{SC}. The term *incident photon to electrical conversion efficiency* (IPCE) is a quantum-yield term

for the overall charge injection collection process measured using monochromatic light (single wavelength source) excitation.

The photocurrent measured under closed circuit I_{SC} is the integrated sum of IPCE measured over the entire solar spectrum [17]:

$$I_{SC} = \int_0^\infty \text{IPCE}(\lambda) \cdot I_{\text{Sun}}(\lambda) \text{d}\lambda \tag{2.1}$$

Thus IPCE(λ) can be expressed as

$$\text{IPCE}(\lambda) = 1240(I_{SC}/\lambda\phi) \tag{2.2}$$

where I_{Sun} is the incident irradiance as a function of the wavelength λ, I_{SC} the current at short circuit (mA/cm^2), and ϕ is the incident radiant flux (W/m^2).

The overall sunlight to electric power conversion efficiency of a DSC is given by:

$$\eta = \frac{P_{\text{max}}}{P_{\text{in}}} = \frac{I_{SC} \cdot V_{OC} \cdot FF}{P_{\text{in}}} \tag{2.3}$$

The maximum power (P_{max}) obtainable in a photovoltaic device is the product of I_{max} and U_{max}. The value of I_{max} gives the maximum photocurrent at the "maximum power point". P_{in} is the solar power input into the PV cell. The fill factor FF is defined as the ratio of $I_{\text{max}}V_{\text{max}}/I_{SC}V_{OC}$. The four values I_{SC}, V_{OC}, FF, and the conversion efficiency η are the key performance parameters of the solar cell.

2.4.3 Key components of a dye-sensitized solar cell

Dye-sensitized solar cells consist of a variety of components that have to be optimized both individually and as a component of the whole assembly. This includes the glass substrate with the transparent conducting oxide (TCO) layer, a mesoporous titanium dioxide (TiO_2) layer, underlayers, dye, electrolyte (organic) solvent, redox couple, and a counter electrode. Ultimately, individual cells have to be interconnected (in an optimized way) in a solar module to guarantee the highest active area for power generation.

Substrates for dye-sensitized solar cells

The sandwich structure of the DSC includes two transparent conducting glass substrates. One requirement for the substrates is a low sheet resistance which should be temperature independent to the high temperatures (450 - 520 °C) used for the sintering process of the TiO_2 layer. Furthermore, a high transparency to solar radiation in the visible-IR region is necessary. Typical sheet resistance of the TCO used is 5 - 15 Ω/□, where the unit "ohms per square" is used to distinguish sheet resistance from *bulk* resistance, has no dimension units, and is independent of the size of the square. Both, indium-doped tin oxide (In:SnO_2, ITO) and fluorine-doped tin oxide (F:SnO_2, FTO) have been employed; however, due to poor thermal stability of the ITO layers, FTO glass is the preferred conducting substrate for the application in dye-sensitized solar cells.

Conducting oxide layers can also be deposited on a variety of substrates, including polymer-based plastics. Advantages of such DSC are low weight, flexibility and possible industrial preparation methods such as roll to roll printing. The disadvantages of plastic substrates include very limited temperature tolerance (max 150 - 160 °C), comparatively higher sheet resistance (60 Ω/□ for ITO-PET), and permeability of the plastics to humidity [18].

TiO_2 as the photoelectrode

Among the many wide-bandgap oxide semiconductors (TiO_2, ZnO, SnO_2,...) that have been examined as potential electron acceptors for DSC, TiO_2 is the most versatile. It delivers the highest efficiencies, is chemically stable, non-toxic, and available in large quantities. Under UV irradiation, it can be used as a photocatalyst to split water, as an anti-foggy coating on glass surfaces (mirror, window pane...) or as an anti-bacterial coating on various substrates [29–31]. Due to its sufficiently low potentials of holes in the valence band, it is widely employed in self-cleaning surfaces to oxidate organic compounds [32]. In contrast to other semiconductors of similar band gaps (e.g. ZnO), it does not photo-degrade upon excitation [33,34]. As it is the basic component of white paint, particulate dispersions of TiO_2, known as P25 (average particle size: 25 nm, 70% anatase and 30% rutile), is produced in large quantities by Degussa for the paint industry. Colloidal particles can be prepared by the controlled sol-gel hydrolysis of Ti-alkoxides [35];

however, in order to reduce preparation times commercially available powders such as P25 are used for the production of TiO_2 pastes [36]. In order to obtain optimal adhesive and rheological properties of a mesoporous film with the TCO substrate, suitable binders are added to the colloidal solution of TiO_2 prior to film deposition by doctor-blade techniques or screen-printing. Sintering of the oxide layers at 450 - 520 °C gives the film two important properties: the individual particles come into close contact so that the conductance and charge collection properties are improved; and the aerial oxidation at elevated temperatures removes organic matter from the mesoporous film that could act as potential trap sites.

TiO_2 has many crystalline forms, with anatase, rutile, and brookite being the most important ones [37]. The crystal structure of anatase and rutile are based on a tetragonal symmetry, in which the Ti^{4+} atoms are 6-fold coordinated to oxygen atoms. The main difference between both structures is the position of the oxygen atoms. In contrast to rutile, anatase has the smaller average distance between the Ti^{4+} atoms; thus, anatase is thermodynamically less stable. The phase transformation from anatase to rutile occurs in the temperature range of 700 - 1000 °C, depending on the crystallite size [38] and impurities [39]. Rutile has slightly lower indirect band gap (3.0 eV) as compared to anatase (3.2 eV), which is attributed to a negative shift of the conduction band in anatase by 0.2 eV [37]. The bonding within TiO_2 is partly covalent and partly ionic. Therefore, stoichiometric crystals are insulating. However, a significant amount of trap states are induced during most synthesis routes, which are due to oxygen vacancies. These vacancies can also be formed reversibly under reduced pressure [40] and/or elevated temperature [41], which can lead to a variation in conductivity by several orders of magnitude. The oxygen vacancies cause the formation of Ti^{3+}-state, which dope the crystal negatively (n-type).

In the standard version of DSC, the typical film thickness is 2 - 15 μm, and the films are deposited using nanosized particles of 10 - 30 nm. A double-layer structure can be fabricated, where an underlayer of thickness 2 - 4 μm is first deposited using larger (200 - 300 nm) size particles that acts as a light-scattering layer to induce a photo-trapping effect [42]. However, commercially TiO_2 pastes are also available with both nanosized and scattering particles that can be applied in one application step. The deposition of the mesoporous film can be performed by different experimental approaches, with doctor-blading or screen-printing (Section

3.1.1.2) being the most common ones.

Sensitizers for dye-sensitized solar cells

The photosensitizer ("dye") is a fundamental component of the DSC since its main function is to absorb the solar radiation and inject electrons into the conduction band of the oxide substrate. The desirable properties for an efficient photosensitizer are the following: strong light absorption in the visible and near-IR region (for efficient light harvesting); high solubility in organic solvents (to improve the deposition from stock solutions); the availability of suitable anchoring ligands such as carboxylic or phosphonic acid groups (to promote the effective interaction with the oxide surface and thus the coupling of donor and acceptor levels); the LUMO of the dye must be sufficiently high in energy for an efficient charge injection into the TiO_2, and the HOMO must be sufficiently low in energy for an efficient regeneration of the oxidized dye by the redox pair; high thermal and chemical stability (to assure a high turnover number and a corresponding lifetime of the device). Moreover, electron transfer from the dye to the TiO_2 must also be rapid in comparison with decay to the ground state of the dye.

A large variety of potential candidates has been examined over the last 20 years, which includes dyes based on metals such as Ru [43–46], Os [47, 48], Pt [49, 50], Re [51], Cu [52], and Fe [53]. Besides transition metal complexes, such as porphyrin [54, 55] and phtalocyanine dyes [56], a range of organic molecules have also been explored, including coumarins [57], squaraines [58], indolines [59], hemicyanines [60], and other conjugated donor-acceptor organic dyes [57, 61, 62].

Up to now, the best performing dyes are the polypyridine complexes of Ru(II) with one or more anchoring groups (carboxylic or phosphonic acid) as a peripheral substituent. Generally, metal complex photosensitizers consist of a central metal ion with ancillary ligands having at least one anchoring group. Light absorption in the visible part of the solar spectrum is due to a metal-to-ligand charge transfer (MLCT), which promotes an electron from the metal d orbitals to the ligand π^* orbitals, d(π)$\rightarrow$ π^* [63]. Charge injection occurs from the π^* orbitals of the anchoring group to the titanium 3d orbitals. The MLCT absorption of these complexes can be extended to longer wavelengths by introducing a ligand with a low-lying π^* molecular orbital and by destabilizing the metal t_{2g} orbital through

the introduction of a strong donor ligand. However, the extension of the spectral response into the near-infrared region is coupled to a shift of the LUMO to lower levels, hence the charge injection into the TiO_2 conduction band can no longer occur [64].

Upon adsorption, the dye transfers most of its protons to the TiO_2 surface; thus, charging it positively. At this point, the associated shift of the TiO_2 conduction band assists the electron injection; thereby, increasing the photocurrent whereas the open-circuit voltage is lowered due to the positive shift of the conduction band edge induced by the surface protonation. Therefore, the degree of protonation of the sensitizer needs to be optimized to maximize the power conversion efficiency [65].

The highest conversion efficiencies have been reached using the tetraprotonated *cis*-bis(isothiocyanato)*bis*(2,2'-bipyridyl-4,4'-dicarboxylate)ruthenium(II) complex ("N3") and its doubly deprotonated analogue "N719". While these sensitizing Ru-complexes are photochemically quite unstable in solution and only moderately stable when adsorbed on ZnO [66,67], remarkable stability is obtained when chemisorbed to titanium dioxide surfaces [68]. It has been suggested that, during photoinduced electron transfer to TiO_2, the Ru-complex is able to induce a back-bonding reaction via Ti^{3+} to form a temporary interfacial Ti^{3+}-ligand-Ru^{2+} charge-transfer complex [69]. Figure 2.1 presents the UV/Vis absorbance spectra of the "standard" sensitizer used in this work, the Ru-dye N719.

Electrolytes for dye-sensitized solar cells

Generally, the electrolyte for DSC consists of a a solvent based solution containing the redox couple and various additives, such as a lithium salt and tert-butylpyridine. The function of the redox couple is to reduce the dye cation, following charge injection, and to work as a shuttle, carrying the charge back and forth between the two electrodes. The crucial aspects is that the dye cation should be reduced faster than the back reaction with the injected electron, and that the electrolyte should be reduced slowly by the conduction band electrons in the TiO_2, and fast at the counter electrode.

Among many redox couples examined, the iodide/triiodide couple has been found to have the best performance. Electrolytes can be roughly divided into

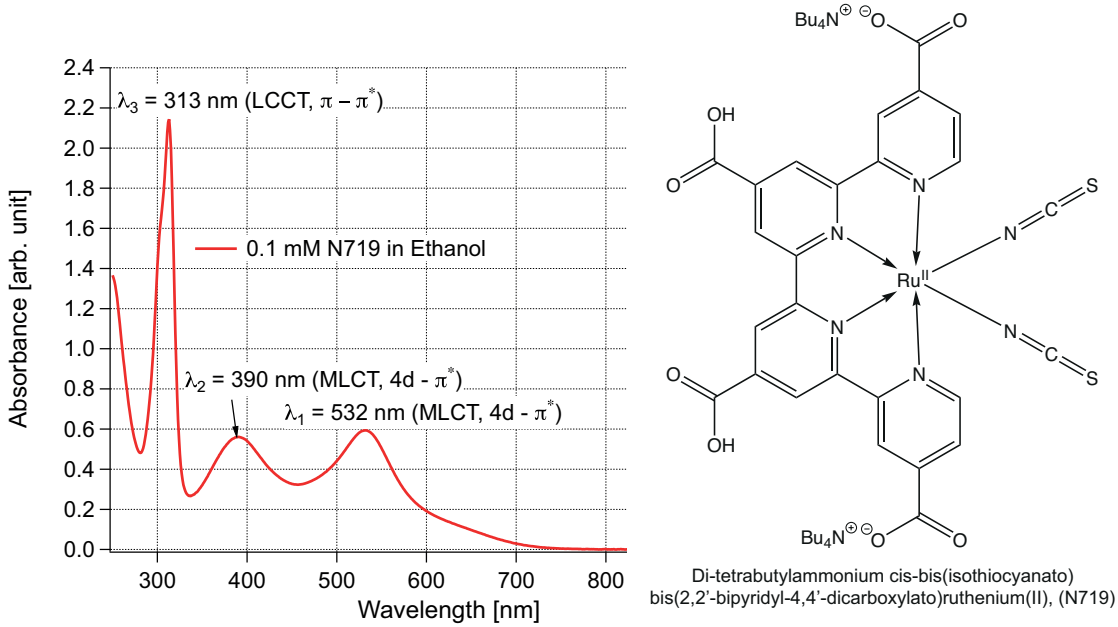

Figure 2.1: UV/Vis absorbance spectra and structure of the Ru-dye "N719" (0.1 mM solution in ethanol). Molecular structure adapted from [70].

three categories: *liquid electrolyte*, *quasi-solid-state electrolyte*, and *solid-state electrolyte*. Liquid electrolytes can be further divided according to the solvent used into organic solvent-based electrolytes and ionic liquid-based electrolytes. Organic solvent-based electrolytes have been widely used and investigated in DSC with high light to electricity conversion efficiencies since volatile organic solvent, such as acetonitrile, can easily dissolve a wide range of organic and inorganic compounds. However, their low boiling points and high vapor pressures provide significant complications regarding long-time sealing and encapsulation of the cell. In a closed environment, the local vapor pressure of the solvent rises to very high values when the boiling point is reached, and the ability of the solvents to extract components becomes very high. This effect causes a slow extraction of the sealing materials to the electrolyte; thereby, decreasing the performance of the device. Leakage of the solvent potentially leads to a point where the cell completely dries out and ceases to function [71, 72].

There have been efforts to find alternatives to the toxic, volatile solvents presently used in DSC. Among those, ionic liquids of the dialkyl imidazolium salts family (also known as room temperature molten salts) have been found to be suitable can-

didates [42, 73]. Ionic liquids have many desirable properties, such as high thermal stability, negligible vapor pressure, non-flammability and excellent environmental compatibility. However, due to their high viscosity (one to two orders higher than the volatile solvents) the diffusion current and the associated power-conversion efficiency is significantly reduced.

The category of *quasi-solid-state electrolytes* refers to both organic solvents and ionic liquids, which can be gelated, polymerized, or dispersed with polymeric materials. Both types of liquids have been used as starting materials, and the inclusion of gelating or polymeric agents transforms the electrolyte into a quasi-solid electrolyte [42, 74]. Unlike hole conductors, a redox couple is included (usually the iodide/triiodide couple) and charge transport occurs mainly by diffusion of molecules, rather than by hopping of charge.

One approach to overcome the problems associated with the use of volatile solvents was proposed by Junghänel and Tributsch [75], where no organic solvents were present and the iodide/iodine based electrolyte was reduced to a stable film on the surface of the TiO_2 particles (Section 2.5.3). This promising approach will be further pursued in this work.

The counter electrode

To complete the regenerative cycle in a DSC, the oxidized form of the redox couple has to be reduced at the counter electrode by the electrons flowing through the external circuit. In the case of the iodide/iodine redox couple, the oxidized form corresponds to triiodide and its reduction involves two electrons:

$$I_3^- + 2\,e^- \rightarrow 3\,I^- \tag{2.4}$$

The counter electrode must be catalytically active to ensure rapid reaction and low overpotential. Platinum has been the material of choice; deposited as Pt-metal clusters in low quantities ($\sim 5\ \mu g/cm^2$) on TCO glass [76]. However, the iodide/iodine redox electrolyte is highly corrosive and especially for high redox concentrations, clusters of Pt may be dissolved and consequently short-circuit the cell [77].

To avoid such problem, alternatives to platinum are needed. A prospective candidate is carbon, which is resistant to corrosion and also an inexpensive material,

which can be used as the counter electrodes in DSC [78, 79]. Different forms of carbon are applied, including graphite, pyrolytic carbon, carbon black, and single and multiwalled carbon nanotubes. The replacement of platinum by a carbon layer was carried out in the course of this work (Section 3.1.2.2) .

2.5 Dye-sensitized solar cells

In the following Section, a short overview of the cell concepts for dye-sensitized solar cells is given; namely the liquid DSC (Section 2.5.1) and the (quasi-) solid-state DSC (Section 2.5.2). The principle of the main solar cell device investigated in this work, the NSCSC, is presented (Section 2.5.3); similarities and differences in the device concepts are discussed.

2.5.1 The liquid nanostructured dye-sensitized solar cell

Dye-sensitized solar cells are based on a non-toxic semiconductor that is sensitized with a ruthenium containing dye molecule. A redox electrolyte and two conducting glass substrates provide the connector to the external circuit. The functional principle is similar to photosynthesis: Upon photoexcitation, the dye molecules inject an electron into the conduction band (E_C) of TiO_2, leaving the dye in its oxidized state (D^+, also referred to as dye cation). The dye is restored to its ground state by electron transfer from the redox pair. The regeneration of the sensitizer by iodide intercepts the recombination of the conduction band electron with the oxidized dye. Diffusion of $e^-_{TiO_2}$ through the nanocrystalline TiO_2 film to the substrate SnO_2 electrode and diffusion of the oxidized redox species (I_3^- ions formed by oxidation of I^-) through the solution to the counter electrode allow both charge carriers to be transferred to the external circuit, where useful work is performed and the regenerative cycle is completed by electron transfer to reduce I_3^- to I^- (Figure 2.2).

The main difference to Si-based solar cells lies in the separation between charge-generation (dye-molecule) and charge-transport (TiO_2) and the fact that charge separation occurs by means of kinetic irreversibility rather than by an built-in electrical field. Therefore, it is of critical importance for the functioning of the cell that the injection of electrons into the TiO_2 is many orders of magnitude faster

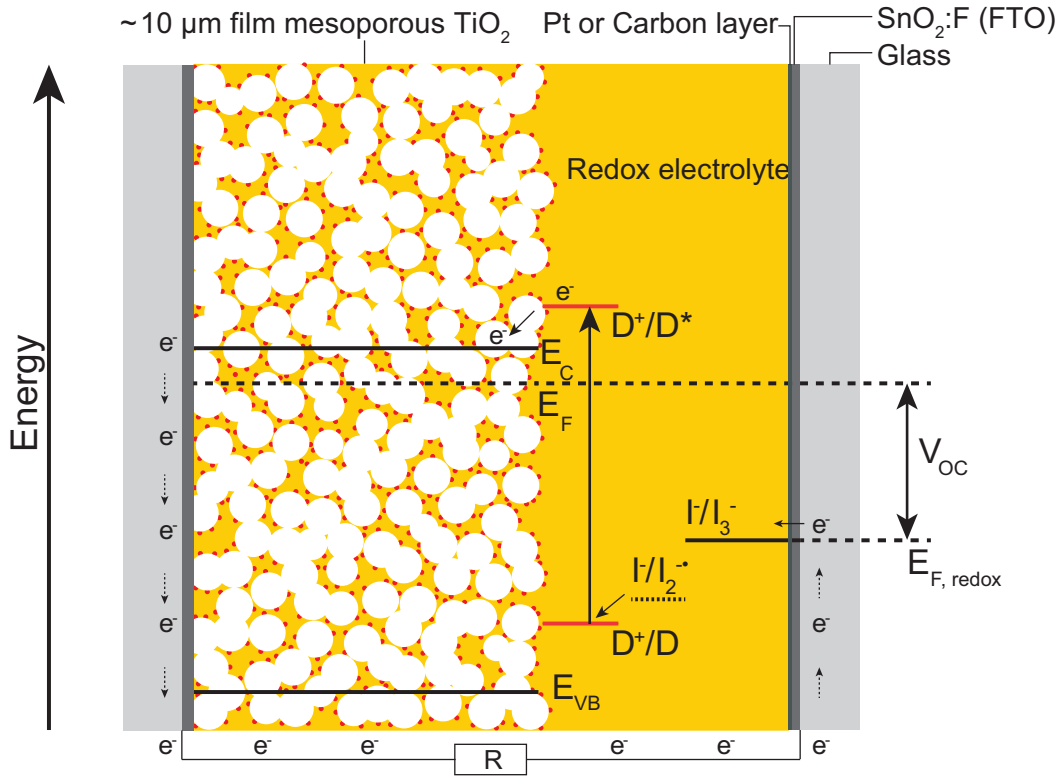

Figure 2.2: Schematic of the functional principle of a dye sensitized solar cell. E_{VB} and E_{C} are the position of the valence- and conduction band of the TiO_2, respectively. The open circuit voltage V_{OC} is defined by the difference between the Fermi level E_{F} and the redox potential $E^0_{\mathrm{F,redox}}$ of the iodide/iodine couple. D^+/D is the ground state and D^+/D^* is the excited state of the sensitizer from which electron injection into the TiO_2 conduction band occurs.

than any recombination (loss) of charge carriers. Moreover, the most important recombination process is the direct electron-transfer from the conduction band of TiO_2 to the redox electrolyte without passing the external circuit.

2.5.2 The solid-state dye-sensitized solar cell

In contrast to conventional DSC with a liquid electrolyte, solid-state dye sensitized solar cells use a solid-state organic hole conductor. Whereas in redox electrolytes the charge transport is due to movement of the redox molecules, the positive charge in a hole conductor moves between neighboring molecules or moieties [80]. Currently, the most effective hole transporter used is a methoxy triaryl

diamine substituted spiro centered molecule, namely 2,2',7,7'-tetrakis(N,N-di-*p*-methoxyphenyl-amine)-9,9'-spirobifluorene (spiro-OMeTAD), with an efficiency of 5% [81, 82]. The lower efficiency compared to liquid electrolyte DSC is primarily a consequence of incomplete light harvesting [81]. In order to fabricate efficient cells, the dye molecules have to be in contact with both the TiO_2 and the hole conductor. However, insufficient pore filling of the TiO_2 layer with the hole conductor limits the film thickness. Therefore, solid-state DSC are restricted to a 2 - 3 μm thick active layer, which is far thinner than needed to achieve good optical absorption for most of the currently used sensitizers [83].

Another limiting factor is the two orders of magnitude faster recombination of injected electrons with the compensating positive charge in the hole conductor when compared to the extraordinary slow recombination of electrons with the oxidized redox part in liquid DSC [84].

2.5.3 The Nano Surface Conductivity Solar Cell (NSCSC)

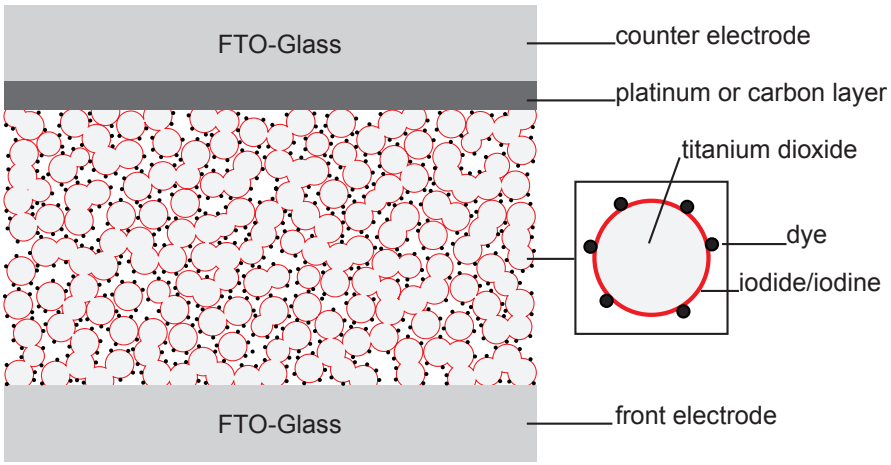

Figure 2.3: Scheme outlining the cell concept of a quasi-solid-state Nano Surface Conductivity Solar Cell (NSCSC). The mesoporous TiO_2 layer is covered by a film of iodide/iodine in a supersaturated state acting as the hole transporting medium towards the counter electrode. No additional solvent is present and the cell is in equilibrium with the ambient atmosphere.

The cell concept of the nano surface conductivity solar cell developed by Junghänel and Tributsch [75] also consists of sensitized TiO_2 nanoparticles; however,

the electrolyte is reduced to a stable film on the surface of the nanoparticles. In contrast to conventional dye-sensitized solar cells, the NSCSC works without any organic solvent. The redox pair (iodide/iodine in a supersaturated state) equilibrates with ambient humidity to form a quasi-solid-state gel. As an alternative to the platinum counter electrode, carbon particles can be placed directly by spraying with an airbrush on the front electrode to catalyze the reduction of triiodide.

Furthermore, due to the basic principle of the cell to be at equilibrium with the ambient atmosphere, the expensive and unstable encapsulation of the cell can be omitted. However, comparative measurements of the two cell concept revealed a higher recombination rate at the TiO_2/electrolyte-interface of the NSCSC [8]. Fortunately, the absence of a liquid electrolyte in this cell allows the application of highly performing transient techniques to the entire cell, such as transient photoconductance measurements in the microwave frequency range (TRMC, Section 4.1.1).

2.6 Charge transfer processes in the dye-sensitized solar cell

The following Section provides an overview of mechanisms assumed to be responsible for charge transfer processes in the DSC. This includes the kinetics of electron transfer and the origin of photovoltage (Section 2.6.1), electron trapping processes (Section 2.6.2), a description of electron transport based on the continuity equation under steady-state conditions (Section 2.6.3), and recombination processes that lead to a loss of charge carriers (Section 2.6.4).

2.6.1 Kinetics of electron transfer and the origin of photovoltage

Under illumination at open circuit, the net rate of electron injection into the mesoporous oxide must be balanced by the net rate of electron injection to I_3^- in the electrolyte and to the oxidized dye D^+. Back reaction to D^+ is assumed to be negligible due to an efficient dye regeneration by I^-. The local rate of electron injection, $\upsilon_{\mathrm{inj}}(x, \lambda)$, is determined by the product of the light intensity, I_0, the

absorption coefficient of adsorbed dye, α, and the injection efficiency, η_{inj} [18]:

$$\upsilon_{\text{inj}}(x,\lambda) = \eta_{\text{inj}}\,\alpha(\lambda) I_0\,\exp(-\alpha(\lambda)x) \tag{2.5}$$

An average global injection rate of electrons can be defined as the ratio of the wavelength-dependent light harvesting efficiency, η_{lh}, the incident photon flux, I_0, and the injection efficiency, η_{inj} to the film thickness d:

$$\upsilon_{\text{inj}} = \frac{\eta_{\text{lh}}\eta_{\text{inj}} I_0}{d} \tag{2.6}$$

The rate of the back reaction (Eq. 2.7) depends on the reactant concentration and the rate constants for electron transfer.

$$\mathrm{I_3^-} + 2\,e^- \rightarrow 3\,\mathrm{I^-} \tag{2.7}$$

At open circuit, since the system is in a stationary state, this injection rate must balance the rate of the back reaction via $\mathrm{I_3^-}$, which in the case of first-order reaction rates in electron concentration, is given by:

$$\upsilon_{\text{br}} = k_{\text{br}} n_c n_{\mathrm{I_3^-}} \tag{2.8}$$

where k_{br} is the rate constant for the back reaction, and n_c and $n_{\mathrm{I_3^-}}$ the concentration of electrons and I_3^-, respectively. Under the simplifying assumptions that electron transfer via surface states is neglected and the reaction orders with respect to electrons and triiodide are taken as one, the steady-state free electron density at open circuit under illumination is a linear function of light intensity, and is given by:

$$n_c = \frac{\eta_{\text{lh}}\eta_{\text{inj}} I_0}{k_{\text{br}} n_{\mathrm{I_3^-}} d} = \frac{\eta_{\text{lh}}\eta_{\text{inj}} I_0 \tau_0}{d} \tag{2.9}$$

where $\tau_0 = 1/k_{\text{br}} n_{\mathrm{I_3^-}}$ is the conduction band electron lifetime determined by the back reaction with $\mathrm{I_3^-}$.

The most important indirect measure of the conduction band electron density is the open circuit photovoltage, V_{OC}. The photovoltage in any solar cell, including the DSC, is the difference in the Fermi energy E_F (or electrochemical potentials) of electrons in the contacts on each side. In the dark (at equilibrium), E_F must

be the same in all phases in the DSC and equal to the Fermi energy of the redox system, $E_{F,\text{redox}}$. The occupancy of electronic energy levels is related to Fermi energy by the Fermi Dirac function [17]:

$$f(E) = \frac{1}{\exp\left(\frac{E-E_F}{k_B T}\right) + 1} \tag{2.10}$$

where k_B is the Boltzmann constant and T is the temperature. When $E - E_F$ is much greater than $k_B T$, corresponding to non-degenerate conditions, Eq. 2.6 reduces to the Boltzmann limit:

$$f(E) = \exp\left(-\frac{E - E_F}{k_B T}\right) \tag{2.11}$$

In the dark, the (very low) density of electrons in the conduction band is determined by the product of the density of states function N_c and the occupation probability:

$$n_c^0 = N_c \exp\left(-\frac{E_C - E_{F,\text{redox}}}{k_B T}\right) \tag{2.12}$$

Under illumination at open circuit, the concentration of electrons in the TiO_2 increases to a stationary value which is limited by the balance between electron injection and back reaction of electrons to I_3^- present in the electrolyte, and recombination with the oxidized dye D^+. This steady-state electron concentration defines ${}_nE_F$, the quasi-Fermi level of electrons. The density of free electrons in the conduction band of the TiO_2 is then given by:

$$n_c = N_c \exp\left(-\frac{E_C - {}_nE_F}{k_B T}\right) \tag{2.13}$$

The photovoltage of a DSC corresponds to the change of the Fermi level in the TiO_2 induced by illumination [85]:

$$\begin{aligned} qU_{\text{photo}} &= {}_nE_F - E_{F,\text{redox}} \\ &= (E_C - E_{F,\text{redox}}) - (E_C - {}_nE_F) \\ &= k_B T \ln\left(\frac{n_c}{n_c^0}\right) \end{aligned} \tag{2.14}$$

The energy difference between $E_{F,\mathrm{redox}}$ and the conduction band energy E_C in the dark is in the order of 1 eV [86], which corresponds to a very low equilibrium electron density n_c^0 of $\sim 10^3$ cm^{-3} in the conduction band. Under illumination, n_c increases to $\sim 10^{16}$ cm^{-3}.

Under the simplifying assumptions made above regarding ideality and reaction order with respect to electron density, it follows from Eq. 2.9 that the photovoltage is given by:

$$qU_{\mathrm{photo}} = k_B T \ln\left(\frac{\eta_{\mathrm{lh}}\eta_{\mathrm{inj}}}{n_c^0 d}\right) + k_B T \ln \tau_0 + k_B T \ln I_0 \tag{2.15}$$

Equation 2.15 predicts that plots of the light intensity versus the photovoltage should have slopes of 59 mV per every decade. However, since DSC are always non-ideal to some extent, the photovoltage varies with values as high as 110 mV/decade. An empirical non-ideality factor, m (> 1) is often employed to account for non-ideality, so that the intensity dependence of the photovoltage is given by:

$$\frac{dU_{\mathrm{photo}}}{d\log_{10} I_0} = m\frac{2.303\, k_B T}{q} \tag{2.16}$$

The origin of the non-ideality in the light intensity dependence of the photovoltage is not well understood. A possible explanation was proposed as the consequence of electron transfer from the TiO_2 to I_3^- ions via "surface states", surface energy levels located in some kind of energy distribution below the conduction band [87]. However, non-ideality has also been observed at short circuit conditions, when photoinjected electrons are collected at the anode and electron transfer to I_3^- via surface states cannot be responsible [88]. Peter suggested that "electron traps" in DSC may not be physical defects in the TiO_2 but rather the result of Coulombic trapping of electrons near the interface between the TiO_2 particles and the adjacent ionic solution which leads to the formation of a non-ideal 2-D electron gas with strong electron-electron repulsions [85].

2.6.2 Electron trapping

The observation that measurements of electron lifetimes in DSC by transient or periodic illumination methods revealed an intensity dependence [89, 90] was initially interpreted as an indication that the reaction of electrons with I_3^- was higher

order in electron density [91]. However, later it was explained as a consequence of trapping and detrapping of electrons at states located in the band gap of the TiO_2 [92].

When electrons are injected, they will fall into a available trapping state, from which they can escape by thermal activation. Therefore, the transport of electrons across the TiO_2 is slowed by the effect of trapping. Similarly, the electrons must be thermally released before they can recombine with I_3^-, unless they are within tunneling distance from the interface between the TiO_2 and the redox species. Thus, the traps act as a buffer, slowing all processes of transport and recombination. At steady state; however, since most trapping states up to the quasi Fermi level are filled, transport and recombination are not affected by trapping.

The origin of the electron traps is a subject of discussion. They could correspond to trapping of electrons at defects in the bulk or surface regions of the mesoporous oxide or to Coulombic trapping due to interaction of electrons with the cations of the electrolyte [85, 93].

Evidence for the existence of a high density of electron traps in the mesoporous TiO_2 comes from charge extraction technique, where the charge stored in the states under illumination is extracted in the dark [94, 95]. It has been observed that the energy distribution, $g(E_t)$, of electron trap states can often be described by an exponential function of the form [96]:

$$g(E_t) = \frac{N_{t,0}}{k_B T_0} \exp - \left(\frac{E_C - E_t}{k_B T_0} \right) \tag{2.17}$$

where $N_{t,0}$ is the total trap density (typically 10^{19}-10^{20}) and T_0 is a characteristic temperature that is generally considerably higher than ambient temperature (T_0 = 600 - 1500 K). This means that the density of trapped electrons increases more slowly than the conduction band electron density as the Fermi level moves up. It is generally assumed that electrons are exchanged between trap levels and the conduction band in such a way that the trap occupancy is determined by the Fermi-Dirac function. The upward movement of the electron quasi-Fermi level (due to illumination or applied voltage) increases the density of trapped electrons

by an amount Δn_t given by:

$$\Delta n_t = \int_{-\infty}^{-\infty} f_{FD}^{\text{light}}(E) g(E)\,\mathrm{d}E - \int_{-\infty}^{-\infty} f_{FD}^{\text{dark}}(E) g(E)\,\mathrm{d}E \tag{2.18}$$

where f_{FD}^{light} and f_{FD}^{dark} are the Fermi-Dirac functions:

$$f_{FD}^{\text{light}} = \frac{1}{1+\exp\left(\frac{E_C - {}_nE_F}{k_B T}\right)} \tag{2.19a}$$

$$f_{FD}^{\text{dark}} = \frac{1}{1+\exp\left(\frac{E_C - E_{\text{F,redox}}}{k_B T}\right)} \tag{2.19b}$$

In the zero Kelvin approximation, meaning that all states up to the quasi Fermi level are occupied, and all those above are empty, the two Fermi-Dirac functions can be replaced by step functions at $E_{\text{F,redox}}$ and ${}_nE_F$, which gives the simpler expression:

$$\Delta n_t = \int_{E_{\text{F,redox}}}^{E_{\text{F,redox}}+qU_{\text{photo}}} g(E)\,\mathrm{d}E \tag{2.20}$$

It follows from this discussion that the density of trapped electrons is generally many orders of magnitude higher than the density of electrons in the conduction band [18]. An important consequence of the exchange of electrons between trap states and the conduction band is that perturbation of a DSC changes the density of trapped electrons as well as that of electrons in the conduction band. For a small perturbation in light intensity at open circuit, the time it takes to reach a new steady state is determined by the time required to re-establish the condition $\partial f/\partial t = 0$ (where f represents the trap occupancy), in which the rate of electron trapping is balanced by the rate of thermal release of electrons from traps [92].

As a consequence of the buffering effect of traps, the measured relaxation time associated with electron transport and with electron transfer to I_3^- depends on the light intensity [91, 95, 97]. This problem has been addressed by Bisquert and Vikhrenko in the *quasi-static approximation*, which states that the time constant

for the relaxation of the conduction band electron density τ_n is given by [98]:

$$\tau_n = \left(1 + \frac{\partial n_t}{\partial n_c}\right) \tau_0 \tag{2.21}$$

where $\tau_0 = 1/k_{\mathrm{br}} n_{\mathrm{I}_3^-}$ (cf. Eq. 2.9). The $\partial n_t/\partial n_c$ term in Eq. 2.21 reflects that the densities of trapped and free electrons vary with changes in the quasi Fermi level (cf. Eqs. 2.13 and 2.17, respectively):

$$\frac{\partial n_t}{\partial n_c} = \frac{\partial n_t}{\partial_n E_F} \frac{\partial_n E_F}{\partial n_c} = g({}_nE_F) \frac{k_B T}{n_c} \tag{2.22}$$

Eqs. 2.21 and 2.22 explain the observation of the effective electron lifetime τ_n (i.e. the time constant for relaxation of the conduction band electron density) decreasing as the bias light intensity increases, since n_c varies more rapidly with ${}_nE_F$ than $g({}_nE_F)$ if the characteristic temperature of the trap distribution (T_0) is greater than the ambient temperature (T). Similarly, the effective diffusion coefficient, D_n, has been observed to increase with light intensity, which was explained by the relaxation of the density of trapped electrons that are exchanged with the mobile electrons in the conduction band; thus, D_n depends on trap occupancy and hence of the Fermi level and is related to the diffusion coefficient of free electrons, D_0, in the TiO_2 by the expression:

$$D_n = \left(1 + \frac{\partial n_c}{\partial n_t}\right) D_0 \tag{2.23}$$

The significance of Bisquert and Vikhrenko's work is that it simplified the multiple trapping model [92,99–101] (in which electrons go through trapping and detrapping events, and only contribute to the diffusion current when they are in the conduction band) and by applying the quasi-static approximation, reduced it to a simpler diffusion model, which accounts for trapping/detrapping.

2.6.3 Electron transport

The driving force for transport of electrons and holes (or any other species such as ions) in any solar cell is the gradient of free energy or electrochemical potential, $\partial \overline{\mu}_i/\partial x$, which is equivalent to the gradient of the Fermi energy, $\partial E_F/\partial x$ [17]. The electrochemical potential, $\overline{\mu}_i$ associated with a species i with charge $z_i q$ is defined

as:

$$\overline{\mu}_i = \mu_i^0 + k_B T \ln \frac{n_i}{n_i^0} + z_i q \varphi \tag{2.24}$$

where φ is the potential, n_i is the density of the species and n_i^0 is the concentration of some reference state for which the chemical potential takes its standard value μ_i^0. In general, the flux of any charged species is related to the gradient of electrochemical potential:

$$J_i = -\frac{z_i n_i u_i}{q} \frac{\partial \overline{\mu}_i}{\partial x} \tag{2.25}$$

where u_i is the mobility, and the gradient of electrochemical potential is given by (cf. 2.24):

$$\frac{\partial \overline{\mu}_i}{\partial x} = \frac{k_B T}{n_i} \frac{\partial n_i}{\partial x} + z_i q \frac{\partial \varphi}{\partial x} \tag{2.26}$$

The flux of species is then given by:

$$J_i = -\frac{u_i k_B T}{q} \frac{\partial n_i}{\partial x} - z_i u_i n_i \frac{\partial \varphi}{\partial x} \tag{2.27}$$

With the Einstein relation $D_i = \frac{k_B T}{q} u_i$, which relates the diffusion coefficient D_i to the mobility, it follows:

$$J_i = -D_i \frac{\partial n_i}{\partial x} - z_i u_i n_i \frac{\partial \varphi}{\partial x} \tag{2.28}$$

The first term is equivalent to Fick's first law of diffusion, and the second term represents the drift current due to a gradient of the electrical potential, i.e. an electric field.

The photo-injected electrons $e^-_{\mathrm{TiO_2}}$ must move through the interconnected TiO_2 particles to reach the anode. Due to the high density of ionic charges in the electrolyte, excess charges arising from the injected electrons in the mesoporous oxide are effectively shielded and electric fields are screened out over short distances. Therefore, it appears that charge transport occurs by diffusion of carriers down the concentration gradient rather than by field-driven drift [35, 102–104] (i.e., the second term in Eq. 2.28 is negligible). Under this assumption, the generation, collection, and transport of electrons in the DSC is described by the continuity

equation [85]:

$$\frac{\partial n_c}{\partial t} = \eta_{inj}\,\alpha(\lambda)\exp(-\alpha(\lambda)x)\,I_0 - N_{t,0}\langle\frac{\partial f}{\partial t}\rangle + D_0\frac{\partial^2 n_c}{\partial x^2} - \frac{(n_c - n_c^0)}{\tau_0} \tag{2.29}$$

n_c is the concentration of electrons in the conduction band, η_{inj} is the injection efficiency, α is the wavelength-dependent absorption coefficient, x is the distance from the anode, I_0 is the incident photon flux, $N_{t,0}$ is the concentration of electron traps, f is the probability of trap occupation, D_0 is the diffusion coefficient of conduction band electrons, n_c^0 is the concentration of electrons in the conduction band in the dark, and τ_0 is the free electron lifetime. The first term represents the local injection rate, the second term accounts for trapping and detrapping, the third term the time-dependent diffusion of free electrons, and the last term describes the loss of electrons by back-reaction with I_3^-. The angular brackets in the trapping/detrapping term indicate an average over the trap state energies, E_T, weighted by the trap density, $g(E_t)$. Solution of the continuity equation under steady-state conditions (i.e. $\partial f/\partial t$=0) for the free electron concentration requires two boundary conditions:

$$\left.\frac{\partial n_c}{\partial x}\right|_{x=d} = 0 \tag{2.30a}$$

$$-D_0\left.\frac{\partial n_c}{\partial x}\right|_{x=0} = k_{\text{ext}}\left(n_c - n_c^0\exp\frac{qU}{k_BT}\right) \tag{2.30b}$$

Eq. 2.30a implies that electrons are not able to exit the TiO_2 via the electrolyte side of the film and Eq. 2.30b that the flux of electrons extracted at the FTO contact with the electron extraction velocity k_{ext} is equal to the flux of electrons diffusing towards the contact from the film. The current density is given by:

$$J_{\text{ph}} = qD_0\left.\frac{\partial n_c}{\partial x}\right|_{x=0} \tag{2.31}$$

The solution of the continuity equation can be written in a form that resembles the diode equation describing a conventional p-n photodiode [102]:

$$j = qI_0(1 - \eta_{\text{inj}}\exp(-\alpha d)) - q\frac{D_0 n_c^0 d}{L_0^2}\left(\exp\left(\frac{qU}{k_BT}\right) - 1\right) \tag{2.32}$$

The first term in Eq. 2.32 represents the photo-generated current, which is determined by the amount of light I_0 absorbed and by the injection efficiency η_{inj}. The second term represents the dark current of the device associated with electron transfer from the TiO_2 to I_3^-. L_n is the diffusion length of electrons in the TiO_2, which is defined as:

$$L_n = \sqrt{D_0 \tau_0} \tag{2.33}$$

L_n is a measure of how far an electron diffuses toward the anode before it is lost by electron transfer to I_3^-. Thus, the diffusion length has to be larger than the film thickness, with good DSC having L_n values that are 2 - 3 times the film thickness. In the limit $\exp(qU_{\text{photo}}/k_BT) \gg 1$ and for strong light absorption ($\exp(-\alpha d) \ll 1$), the open circuit voltage follows from the condition $j = 0$ [96]:

$$qU_{\text{photo}} = k_BT \ln\left(\frac{I_0\tau_0}{n_c^0 d}\right) = k_BT \ln\left(\frac{n_c}{n_c^0}\right) \tag{2.34}$$

which is identical to the result obtained in Eq. 2.14.

2.6.4 Charge recombination

There are three major energy-wasting recombination pathways inside the cell. One involves recombination of $e^-_{TiO_2}$ with the oxidized dye before the dye can be regenerated by the redox couple:

$$e^-_{TiO_2} + D^+ \rightarrow D \tag{2.35}$$

This process is remarkably slow (microseconds to milliseconds for Ru-dyes) at short-circuit and thus does not limit the short-circuit photocurrent density [105–108]. However, when the potential of the substrate electrode becomes more negative (e.g., as the cell voltage changes from short-circuit (0V) to its open-circuit photovoltage, V_{OC}), the rate of reaction (2.35) increases [109]. At open circuit, no current flows and the rate of charge photogeneration equals the total rate of charge recombination.

The two other recombination reactions are the recombination of $e^-_{TiO_2}$ with the

oxidized redox species:

$$e^-_{\mathrm{TiO_2}} + \mathrm{R}^+ \rightarrow \mathrm{R} \tag{2.36}$$

and the recombination of an electron in the FTO substrate, e^-_{FTO}, with the oxidized redox species:

$$e^-_{FTO} + \mathrm{R}^+ \rightarrow \mathrm{R} \tag{2.37}$$

Reaction 2.37 can be inhibited by applying a compact blocking layer on the FTO substrate (Section 4.1.2.3) to cover spaces between the colloidal particles where the substrate comes into direct contact with the redox solution [110–112]. Reaction 2.36 is favored by the high surface area of the TiO_2 relative to the FTO, but reaction 2.37 is favored by the high concentration of electrons in the degenerately doped FTO relative to the TiO_2 [113, 114].

2.7 Charge transfer involving the redox couple

In this Section, a description of charge transfer processes involving the redox couple is given. Starting from a basic introduction of energy levels of the redox system (Section 2.7.1), the transport of the redox couple itself is described, including a proposed mechanism for quasi-solid-state devices such as the NSCSC (Section 2.7.2). Section 2.7.3 presents the pathway for the regeneration of the dye, whereas recombination losses originating from oxidized redox species are discussed in Section 2.7.4.

2.7.1 Energy levels of redox systems in solution

The electrochemical potential of electrons, redox potential or Fermi level, for a one-electron redox couple is given by the Nernst equation and can be written as [115]:

$$E_{\mathrm{F,redox}} = E^0_{\mathrm{F,redox}} - k_B T \ln\left(\frac{n_{\mathrm{ox}}}{n_{\mathrm{red}}}\right) \tag{2.38}$$

where $E^0_{\mathrm{F,redox}}$ is the standard redox energy level, n_{ox} and n_{red} are the concentrations of the oxidized and reduced species of the redox system, respectively.

The energy states being empty or occupied by electrons are described by the

fluctuating energy level model originally developed by Marcus [116] and applied to the semiconductor/electrolyte interface by Gerischer (Figure 2.4) [117–119].

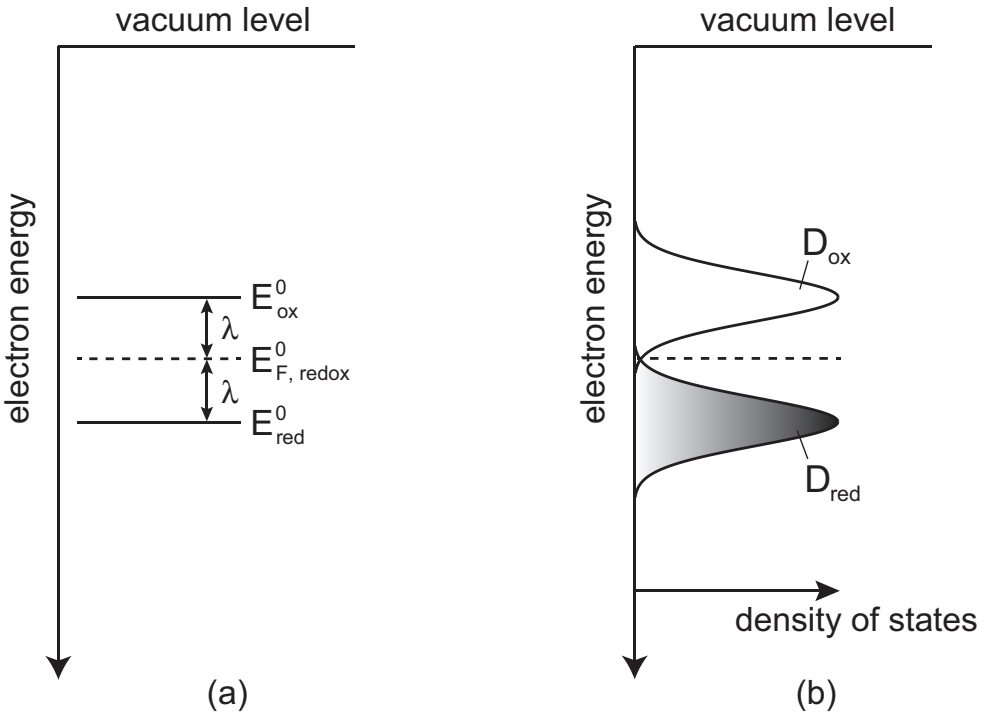

Figure 2.4: Electron energies of a redox system: (a) E^0_{red} = occupied states; E^0_{ox} = empty states; $E^0_{\mathrm{F,redox}}$ = Fermi level of the redox couple. (b) Corresponding distribution function. Adapted from [115].

In this energy scale, E^0_{red} corresponds to the energy position of occupied electron states and E^0_{ox} to the empty states. They differ from the Fermi level, $E^0_{\mathrm{F,redox}}$ by the so-called reorganization energy λ. The reorganization energy is the energy involved in the relaxation process of the solvation shell around the reduced species following transfer of an electron to the vacuum level [115]. For the reverse process, that is, electron transfer from vacuum to the oxidized species, there is an analogous relaxation process. It is normally assumed that λ is equal for both processes. The electron states of a redox system are not discrete energy levels but are distributed over a certain energy range due to fluctuations in the solvation shell surrounding the molecule [120]. This is demonstrated by the distribution of

energy states around the energies E^0_{ox} and E^0_{red} (Figure 2.4b). D_{red} is the density of occupied states (in relative units) represented by the reduced component of the redox system, and D_{ox} is the density of empty states represented by the oxidized component [118]. Assuming a harmonic oscillation of the solvation shell, the distribution curves, D_{red} and D_{ox}, are described by Gaussian functions:

$$D_{\mathrm{red}} = D^0_{\mathrm{red}} \exp\left[-\frac{\left(E - E^0_{\mathrm{F,redox}} - \lambda\right)^2}{4k_{\mathrm{B}}T\lambda}\right] \tag{2.39}$$

$$D_{\mathrm{ox}} = D^0_{\mathrm{ox}} \exp\left[-\frac{\left(E - E^0_{\mathrm{F,redox}} + \lambda\right)^2}{4k_{\mathrm{B}}T\lambda}\right] \tag{2.40}$$

D^0_{red} and D^0_{ox} are normalizing factors making $\int_{-\infty}^{\infty} D(E)\mathrm{d}E = 1$. The half-width of the distribution curves is given by :

$$\triangle E_{1/2} = 0.53\,\lambda^{1/2}\,\mathrm{eV} \tag{2.41}$$

Accordingly, the widths of the distribution function depend on the reorganization energy λ, which is of importance for the kinetics of electron transfer processes at the TiO_2/dye/electrolyte interface. Typical values of λ are in the range from a few tenths of an electronvolt up to 2 eV [121]. In Figure 2.4b, the concentration of reduced and oxidized species are equal (D_{red}=D_{ox}). Changing the concentration ratio varies the Fermi level of the redox couple $E^0_{\mathrm{F,redox}}$ according to the Nernst equation (Eq. 2.38), which can be graphically illustrated as different amplitudes of the distribution function.

Energy levels of the HOMO orbitals of dye complexes adsorbed on TiO_2 layers have been measured using photoelectron spectroscopy [122, 123]. The corresponding densities of states in the valence region have positions above the valence band edge of the semiconductor that fit well with the energy requirements for efficient electron transfer form the electrolyte to the oxidized dye (regeneration of the dye).

2.7.2 Transport of the redox couple

Transport of the redox couple between the electrodes of liquid DSC is mainly driven by diffusion. The diffusion coefficient of I_3^- in the electrolyte might limit the short-

circuit current density of the DSC. The diffusion limiting current density, J_{lim}, is proportional to the porosity, p, the diffusion coefficient, D_0, the concentration of the oxidized form of the redox shuttle, $[R^+]$, and inversely proportional to the thickness of the cell, d, according to [124]:

$$J_{\text{lim}} \propto \frac{pFD_0[R^+]}{d} \tag{2.42}$$

where F is Faraday's constant. Diffusion coefficients of I_3^- have been estimated at $D_0 \approx 10^{-5} - 10^{-6}$ cm^2s^{-1}, depending on the solvent and temperature [125, 126].

In viscous electrolytes, such as ionic liquids (Section 2.4.3), the diffusion coefficient of the triiodide is about 1 - 2 orders of magnitude lower than in organic liquid electrolytes [127]. Therefore, an I_3^- concentration gradient may be produced due to the slow diffusion of I_3^-, which can limit the photocurrent of the DSC. Thus, higher concentrations of I_3^- are required to compensate for the low transport. However, charge transport in iodide-based ionic liquids is often reported to be much faster than predicted by the viscosity of the electrolyte [42, 74, 124]. For high concentrations of the redox couple, an alternative type of charge transport was proposed, called the Grotthus mechanism. This mechanism couples electron hopping and the chemical bonds of polyiodide exchange [73, 128, 129] and can be described by the Dahms-Ruff equation for the apparent diffusion coefficient D_{app} [130]:

$$D_{\text{app}} = D_{\text{phys}} + D_{\text{ex}} = D_{\text{phys}} + k_{\text{ex}}\delta^2 c/6 \tag{2.43}$$

where D_{phys} is the physical diffusion coefficient, k_{ex} is the electron exchange rate constant, δ is the equilibrium center-to-center distance at the exchange reaction, and c is the total concentration of the redox couple in the electrolyte. The second part ($k_{\text{ex}}\delta^2 c/6$) of Equation 2.43 corresponds to the diffusion coefficient due to electron exchange (D_{ex}), and the corresponding diffusion process can be represented as follows [127]:

$$I_3^- + I^- \rightarrow I^- \qquad I_2^- \cdots I^- \rightarrow I^- \cdots I_2^- \qquad I^- \rightarrow I^- + I_3^- \tag{2.44}$$

The formation of polyiodide species was detected in spectroscopic measurements, supporting the enhanced charge transport through a network of polyiodide chains in devices where diffusion limitations might occur [73, 74, 131]. Furthermore, higher

polyiodides ($I_4^{2-}, I_5^-, I_6^{2-}$) were reported to be formed in aqueous iodide/iodine systems [132]. This indicates that a similar transport mechanism may apply in the case of the quasi-solid-state cell concept of the NSCSC presented in this work (Section 2.5.3) where a supersaturated aqueous film of iodide/iodine is available. Since the iodine and iodide concentrations are much higher than in liquid DSC, the Grotthus mechanism can support the charge transport from the counter electrode to the oxidized dye. In addition, diffusion of solvated iodide ions can still occur.

2.7.3 Regeneration of the dye cation by the redox couple

In order to guarantee efficient charge collection in a DSC, the recombination reaction (Eq. 2.35) of injected electrons with the oxidized dye has to be intercepted by a sufficiently fast regeneration of the dye cation.

The mechanism of the reduction of dye cations by iodide is still under debate; however, a proposed pathway for the reduction of the oxidized dye by iodide is given by the following reactions [133–135]:

$$D^* \rightarrow D^+ + e^-_{TiO_2} \tag{2.45}$$

$$D^+ + I^- \rightarrow (D \cdots I) \tag{2.46}$$

$$(D \cdots I) + I^- \rightarrow D + I_2^{-\bullet} \tag{2.47}$$

$$2\, I_2^{-\bullet} \rightarrow I_3^- + I^- \tag{2.48}$$

After electron injection from the excited dye (D^*), the oxidized dye D^+ is reduced by iodide, under the kinetically fast formation of an intermediate complex ($D \cdots I$) [134]. This complex dissociates under the influence of a second iodide ion leading to the dye in the ground state, D, and the formation of the diiodide radical $I_2^{-\bullet}$. The diiodide radicals react to form triiodide and iodide. Previously, the formation of $I_2^{-\bullet}$ was observed by transient absorption (TA) spectroscopy [136–138]. However, recently TA measurements on working cells under operational conditions showed no evidence of such a long-lived radical [139].

For the most common sensitizer cis-Ru(dcbpy)$_2$(NCS)$_2$, the half-time for regeneration in the presence of about 0.5 M iodide in the electrolyte were reported to be in the range of 10 ns to 10 μs [109, 133, 134, 140, 141].

Moreover, the nature and concentration of the cation of the iodide salt was found to have an influence on the regeneration [133]. Rapid oxidation of iodide by the sensitizer's oxidized state was reported to occur in the presence of small cations that adsorb on the TiO_2 surface, such as Li^+ or Mg^{2+}, whereas much slower regeneration was found with TBA^+ ions. This effect was attributed to a higher local iodide concentration near the TiO_2 surface when positive charge is adsorbed. The possible formation of (I^-, I^-) ion pairs was suggested to favor the oxidation of I^- to $I_2^{-\bullet}$:

$$D^+ + (I^-, I^-)|TiO_2 \rightarrow D + I_2^{-\bullet} \tag{2.49}$$

2.7.4 Recombination between conduction band electrons and the oxidized redox couple

Recombination of conduction band electrons from the TiO_2 with the oxidized form of the redox couple can be expressed in terms of the electron lifetime. The electron lifetimes have been measured by different techniques such as open circuit voltage decay, impedance spectroscopy, intensity modulated photovoltage spectroscopy, and other transient photovoltage methods [139, 142–145]. However, not all electrons in the TiO_2 are free conduction band electrons. Sub-band states might trap and release electrons as depicted in Figure 2.5 [96, 146–148]. The distribution of these trap states is exponential, as has been determined by impedance cyclic voltammetry, and charge extraction measurements [95, 149, 150]. Electrons that are trapped in the bulk of the nanoparticle cannot participate in recombination (or diffusion). The trap states thereby modulate the concentration of free conduction band electrons and thus the lifetimes (and charge diffusion). In the quasi-static approximation, the measured electron lifetimes, τ_n, depend on the steady state relationship of free conduction band electrons, n_c, to trapped electrons, n_t (cf. Eq. 2.21) [85, 98]. As a consequence, measured lifetimes exhibit an exponential dependence on potential (cf. Section 2.6.2).

Due to the high iodide concentration and fast regeneration kinetics observed

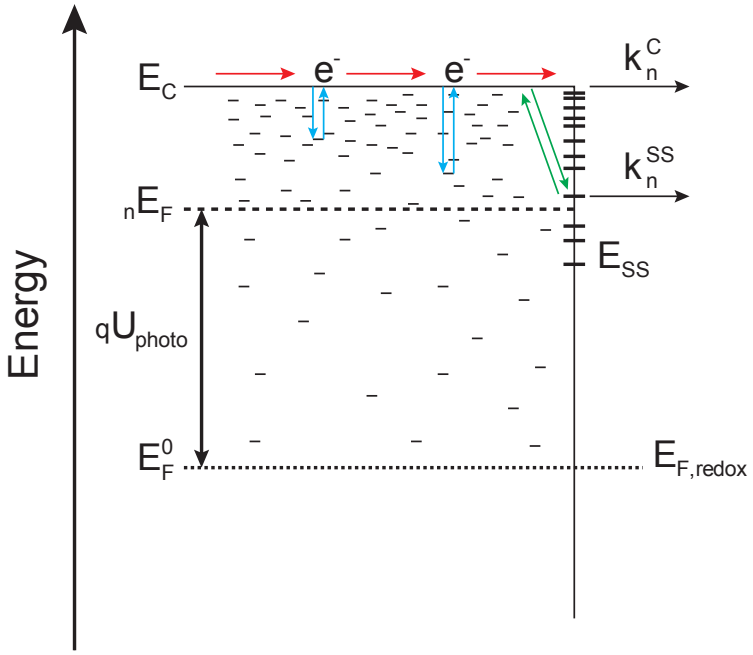

Figure 2.5: Scheme presenting the processes involved in the recombination between electrons in TiO_2 and the oxidized form of the redox couple. E_F^0 is the position of the Fermi level in the dark, equilibrated with the redox potential $E_{F,redox}^0$. ${}_nE_F$ is the quasi Fermi level of electrons which defines the photovoltage U_{photo}. E_C is the conduction band energy and E_{SS} are surface states in the TiO_2. The following processes can occur: Electron transport in the conduction band with rate k_n^C, trapping and release in localized states in the bulk of semiconductor nanoparticles, trapping and release by surface states, electron transfer through surface state with rate k_n^{SS}. Adapted from [146].

in DSC, the recombination reaction of electrons $e^-_{TiO_2}$ with the oxidized sensitizer (Eq. 2.35) is considerably slower than the regeneration of the sensitizer (Section 2.7.3) [138]. Therefore, the primary $e^-_{TiO_2}$ acceptors are the oxidized forms of the redox couple, R^+. Several possible acceptor species can be present in the electrolyte, such as $I^\bullet$, $I_2^{-\bullet}$, I_3^- or I_2 [135]. Details of the possible mechanisms and their associated rate laws have been presented in detail by Ardo and Meyer [63]. In general, the back electron transfer between conduction band electrons and the oxidized form of the redox couple (Eq. 2.36) results in the dark current that limits the photovoltage in the DSC.

One of the proposed pathways is the one-electron reduction of triiodide, which

leads to the formation of the diiodide radical $I_2^{-\bullet}$ [63]

$$I_3^- + e^-_{TiO_2} \rightarrow I_2^{-\bullet} \tag{2.50}$$

and yields iodide through disproportionation (Eq. 2.48). A second pathway includes the reaction of the diiodide radical with $e^-_{TiO_2}$

$$I_2^{-\bullet} + e^-_{TiO_2} \rightarrow 2\,I^- \tag{2.51}$$

which is coupled to the reduction of I_2 (Eq. 2.50), but could also be consecutive to the production of $I_2^{-\bullet}$ by the cation regeneration reaction (Eq. 2.47). However, the rate of the indirect recombination reaction of injected electrons with I_3^- was reported to be second-order in the electron density, with rate constant $k'' = 10^4\,M^{-1}s^{-1}$ for a triiodide concentration of $c = 0.05\,M$ [95, 101]. Such a slow reaction implies that the charge transfer takes place from fully thermalized and trapped carriers. It also suggests that the reaction of electrons with $I_2^{-\bullet}$ (Eq. 2.51) is unable to compete kinetically with the disproportionation of the radical ion (Eq. 2.48), whose rate constant is greater than $10^9\,M^{-1}s^{-1}$ [151].

In summary, it can be stated that iodide based electrolytes have been found to be well suited for DSC because the recombination between electrons in the TiO_2 film and the oxidized part of the redox couple (Reaction 2.36) is extremely slow [113]. Lifetimes of injected electrons were observed to be in the range of 1 - 20 ms under one sun illumination [144, 152, 153].

References

For the realization of this Chapter the following textbooks were used:

- P. Würfel. *Physics of Solar Cells.* Wiley-VCH, 2nd edition (2009).
- R. Memming. *Semiconductor Electrochemistry.* Wiley-VCH, (2001).
- S. M. Sze. *Physics of Semiconductor Devices.* John Wiley & Sons, 2nd edition (1981).
- K. Kalyanasundaram (Editor). *Dye-Sensitized Solar Cells.* EPFL Press, (2010).

- V. Ramamurthy, K. S. Schanze (Editors), *Semiconductor Photochemistry and Photophysics*. CRC Press (2003).
- M. A. Green. *Third Generation Photovoltaics: Advanced Solar Energy Conversion*. Birkhäuser (2006).
- A. J. Bard, L. R. Faulkner. *Electrochemical Methods: Fundamentals and Applications*. John Wiley & Sons, 2nd edition (2001).

3 Experimental

3.1 Cell Preparation

In this Section the production steps of a quasi-solid-state dye-sensitized solar cell based on the cell concept of the NSCSC developed by Junghänel and Tributsch [75] are presented (see Figure 3.1). The cell preparation includes the deposition of a nanoporous TiO_2 layer on a conducting glass substrate by screen-printing, the sensitization of the nanoparticles with a ruthenium dye followed by the deposition of a supersaturated electrolyte film based on an iodide/iodine mixture.

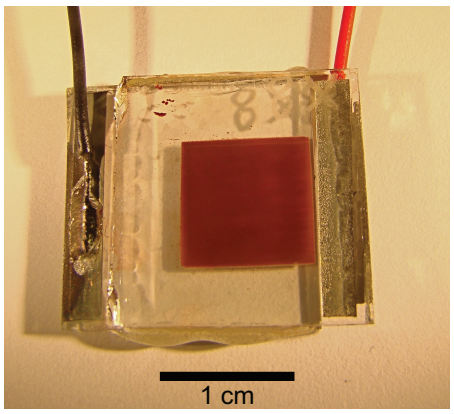

Figure 3.1: Photograph of a nano surface conductivity solar cell (NSCSC).

3.1.1 Front electrode

3.1.1.1 Substrate preparation

Transparent conductive glass (TEC7, d = 2.3 mm, F:SnO_2-doped, FTO) was purchased from Pilkington. The specific resistance of FTO was calculated from the formula: $\rho_{\mathrm{FTO}} = R_{\mathrm{S}} \cdot d_{\mathrm{FTO}}$, where R_{S} is the sheet resistance and d_{FTO} is the

thickness of the F:SnO_2 layer. In the case of the FTO used, $R_S = 7\,\Omega/\square$ (confirmed by a four-point measurement) and $d_{FTO} \approx 600$ nm; thus, the specific resistance of FTO was $\rho_{FTO} = 4.2\,x\,10^{-4}$ Ωcm. The glass substrates of the dimensions 4 x 10 cm were scratched with a glass cutter into areas of 2 x 2 cm. In order to selectively remove the F:SnO_2 layer from the glass in certain areas of the substrate, the FTO was covered in the middle (1 x 1 cm area plus a contact area on one side) with a polyimide (PI) tape and the rest of the substrate was exposed to zinc powder and drops of 2 M hydrochloric acid solution. Such mixture formed hydrogen gas and ZnCl ($Zn + 2\,HCl \longrightarrow H_2 + ZnCl_2$). The hydrogen gas reacted with SnO_2 (from the substrate) to produce Sn metal and water ($SnO_2 + 2\,H_2 \longrightarrow Sn + 2\,H_2O$). Sn metal was then easily removed from the substrate. After this procedure, the PI-tape was removed and the substrates were sonicated for 15 min in a detergent solution (3% RBS®50 in MilliQ water), followed by 10 min in water, acetone, ethanol, and dried in a stream of N_2.

3.1.1.2 Screen-printing of porous TiO_2 electrodes

TiO_2 layers were deposited on the FTO substrates by screen-printing (SEFAR 61-64W screen mesh) the TiO_2 paste (DSL18NR-AO, Dyesol) in two subsequent cycles, resulting in ca. 12 μm thick layer of TiO_2 particles. During every printing cycle ten electrodes of TiO_2 ($A = 1$ cm^2) were printed on the FTO substrate with dimensions 4 x 10 cm. The arrangement of the TiO_2 areas on the substrate is shown in Figure 3.2.

A screen-printing cycle was performed in the following way:

1. The mesh was lifted and the TiO_2 paste was spread on the screen-printing mask with a squeegee applicator at 70° - 80° (angle of the rubber blade) from the mesh; thereby, filling it completely. The mesh was then lowered towards the positioned substrate and the paste was printed at an angle of 80° - 85° with a constant pressure applied to the squeegee. The filling and printing was repeated up to three times to obtain a uniform coverage.

2. The screen-printed substrates were kept at room temperature (RT) for five minutes to reduce mechanical stress in the TiO_2 layer.

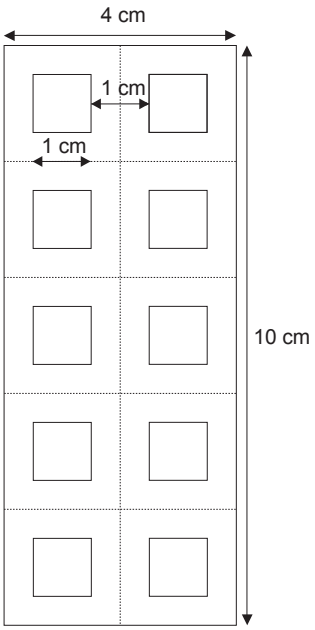

Figure 3.2: Arrangement of the TiO_2 electrodes on the FTO substrate.

3. The substrates were dried on a hot plate for two minutes at 120 °C followed by a cooling down of the substrates at room temperature (RT) for two minutes.

Each screen-printing cycle resulted in a 5 - 6 μm thick TiO_2 layer. To reach the desired total thickness of 10 - 12 μm the above mentioned steps were repeated. The FTO substrate with the printed TiO_2 layers was broken with a glass breaker into single pieces, which were sintered according to the schedule shown in Table 3.1.

	Time /min	temperature /°C	Total time /min
heating	10	280	10
isothermal	10		20
heating	5	380	25
isothermal	15		40
heating	10	520	50
isothermal	30		80
cooling	ca. 70	350	150

Table 3.1: Schedule for the sintering of the TiO_2 layers.

FTO substrates covered with TiO_2 layers were then called electrodes. The cover from the hot plate was opened at 350 °C, when the temperature reached 250 °C,

the electrodes were removed from the oven and cooled down in air to ≈ 60 °C. At this temperature, the electrodes were immersed in a dye solution.

The layer thickness of two electrodes (out of ten electrodes prepared) was measured with a DEKTAK 8 Advanced Development Profiler (Veeco Instruments). This evaluation was done by measuring the vertical displacement of a diamond tipped stylus at a defined scan length, speed, and stylus force. The radius of the stylus was 12.5 μm with a stylus force of 3 mg and a vertical resolution of about 0.1 μm. Figure 3.3 shows the profile of a sintered screen-printed TiO_2 layer. The screen-printing cycle was repeated once to achieve an average layer thickness of 12 μm.

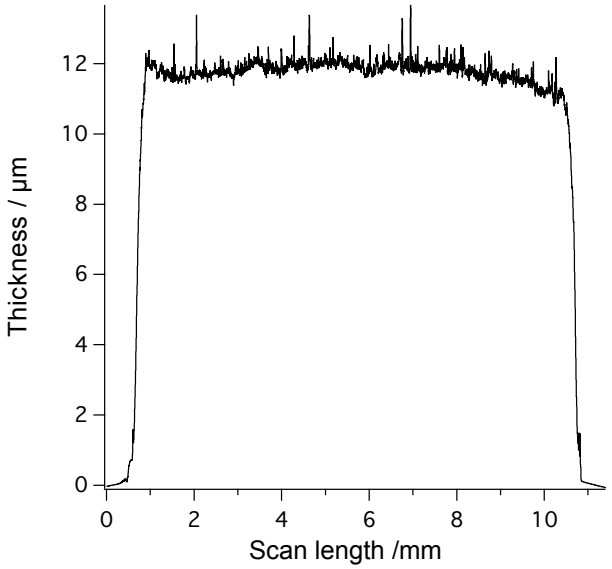

Figure 3.3: Thickness profile of a screen-printed TiO_2 electrode. The average layer thickness was 12 μm.

If the sintered TiO_2 electrodes were not immediately immersed in the dye solution, they had to be reactivated at 520 °C prior to the sensitization to remove contaminations, such as adsorbed CO_2.

3.1.1.3 Surface treatment of the TiO_2 layer

A post-treatment in a titanium(IV) chloride solution was performed on the sintered TiO_2 substrates before the dye sensitization [154]. This treatment is known to

increase the surface area of the TiO_2 layer through the deposition of additional TiO_2 particles on the existing nanoporous layer. Thus, a higher dye adsorption can be reached. Furthermore, it was reported that the post-treatment leads to a shift of the conduction band edge in the TiO_2 resulting in an optimized electron injection and a higher photocurrent [155]. For that purpose the sintered TiO_2 films were placed for 30 min at 70 °C into a 50 mM titanium(IV) chloride in tetrahydrofuran solution (aq.), rinsed with MilliQ water, ethanol, and sintered again at 450 °C for 30 min.

3.1.1.4 Compact TiO_2 underlayer

A compact TiO_2 underlayer was deposited between the FTO substrate and the mesoporous TiO_2 to prevent possible recombination reactions of injected electrons from the FTO substrate with oxidized redox species (cf. Eq. 2.37). Compact TiO_2 "blocking" layers can be deposited by spray-pyrolysis from a titanium actylacetonate precursor [110] or by sol-gel methods [156].

Layers were deposited by dip-coating onto cleaned FTO-substrates with a 10% V/V titanium(IV) isopropoxide in isopropanol under an argon atmosphere. The dip rate was adjusted to 2 mm/s. Two coatings were performed with subsequent heat treatment at 450 °C for 30 min. The resulting thin layers of TiO_2 had a thickness of ca. 100 nm as identified from SEM pictures presented in Figure 3.4.

3.1.1.5 Sensitization of the TiO_2 electrodes

After cooling to 60 °C, the freshly sintered electrodes were immersed into the dye solution according to Table 3.2 and kept at room temperature typically over night for 16 - 20 h.

Name	Molar mass / $g \cdot mol^{-1}$	Volume / mL	Mass / mg	Density / $g \cdot cm^{-3}$	Concentration / $mol \cdot L^{-1}$	Provider
N719	1187.7		17.75		0.001	Dyesol
Acetonitrile	41.05	7.5		0.79		Sigma
tert-Butanol	74.12	7.5		0.78		Sigma

Table 3.2: Composition of the dye-solution.

Figure 3.5 presents the UV/Vis absorptance spectrum of a TiO_2 layer sensitized with the N719 dye.

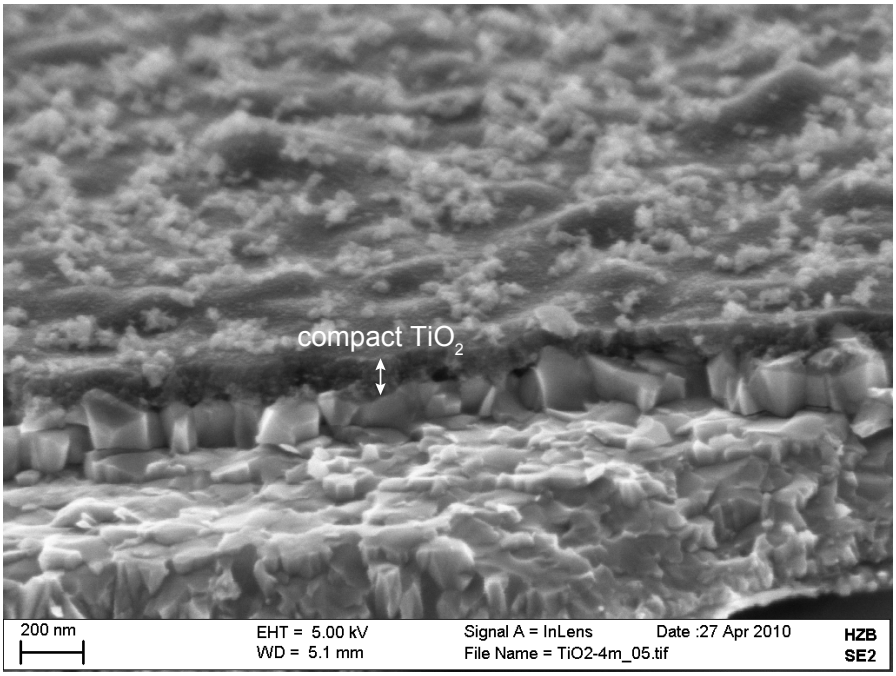

Figure 3.4: SEM image of a compact TiO_2 underlayer deposited on the FTO substrate.

3.1.1.6 Deposition of the electrolyte

After sensitization, the area surrounding the sensitized TiO_2 was masked by adhesive PTFE tape (CT-6571, Chem-Tec) and 3 μL of the electrolyte solution were deposited on the electrode. The composition of the standard electrolyte is given in Table 3.3.

Name	Molar mass / g·mol^{-1}	Volume / μL	Mass / mg	Density / g·cm^{-3}	Concentration / mol·L^{-1}	Provider
Lithiumiodide	133.84		669.2		5	Fluka
Iodine	253.81		12.7		0.05	Sigma
4-tert-butylpyridine	135.21	7.32		0.923	0.05	Aldrich
Ethanol	46.07	1000		0.79		Sigma

Table 3.3: Composition of the electrolyte solution.

The electrodes were stored after the deposition of the electrolyte for 24 h in a dust protected environment at room temperature.

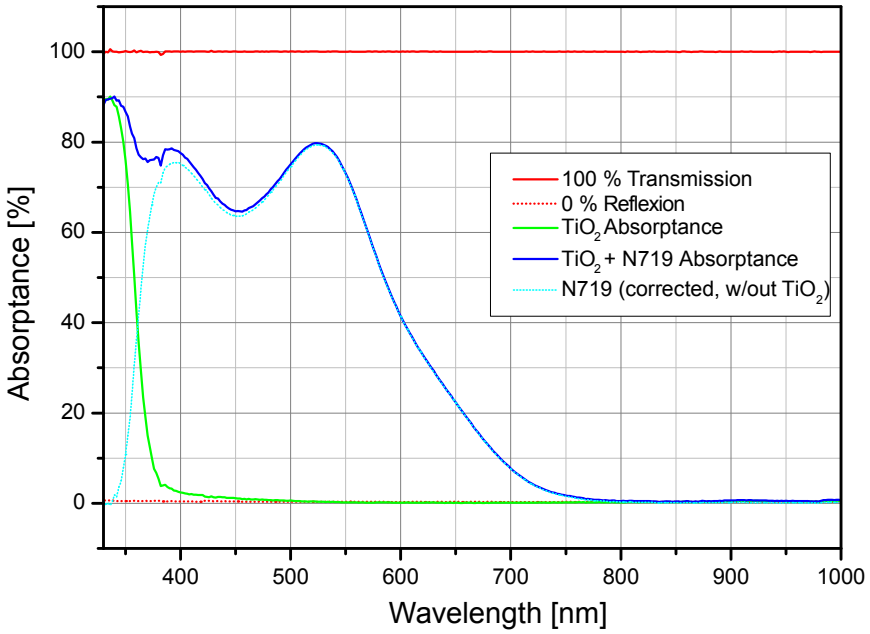

Figure 3.5: UV/Vis absorptance spectrum of the N719 dye on a TiO_2 layer.

3.1.2 Counter electrode

To prepare the counter electrode, the scratched FTO substrates were broken into cells of 2 x 2 cm and cleaned by ultrasound in a detergent solution (3% RBS®50 in MilliQ water) for 15 min, followed by 10 min in MilliQ water and 10 min in ethanol. The single cells were dried in a stream of N_2. Different kinds of counter electrodes were prepared in the course of this work as described in the following Sections.

3.1.2.1 Platinized counter electrodes

The platinum catalyst was deposited on the FTO glass by doctor-blade coating with 20 μL of an aqueous hexachloroplatinic acid solution (composition according to Table 3.4) followed by a heat treatment at 380 °C for 15 min. A layer of highly catalytic platinum clusters was formed by reduction. The counter electrodes were used immediately after platinization or reactivated at 380 °C before contacting them with the front electrode.

Name	Molar mass / g·mol^{-1}	Volume / μL	Density / g·cm^{-3}	Provider
Hexachloroplatinic acid solution (∼10%)	517.92	2.4	1.08	Merck
2-Propanol	60.1	1000	0.79	Merck

Table 3.4: Composition of the platinum solution.

3.1.2.2 Counter electrodes with carbon layer

In contrast to the platinized counter electrodes, a layer of carbon nanoparticles was deposited directly on top of the sensitized substrate containing the electrolyte film by spraying a carbon suspension (60 mg Printex XE2 in 6 mL 2-propanol, 50 μL Nafion) with an airbrush, acting as catalyst for the reduction of iodine and as the electric contact to the counter electrode. The electrodes were stored for another 24 h to remove volatile compounds from the carbon layer. Figure 3.6 shows the SEM image of the carbon layer on a screen-printed TiO_2 electrode.

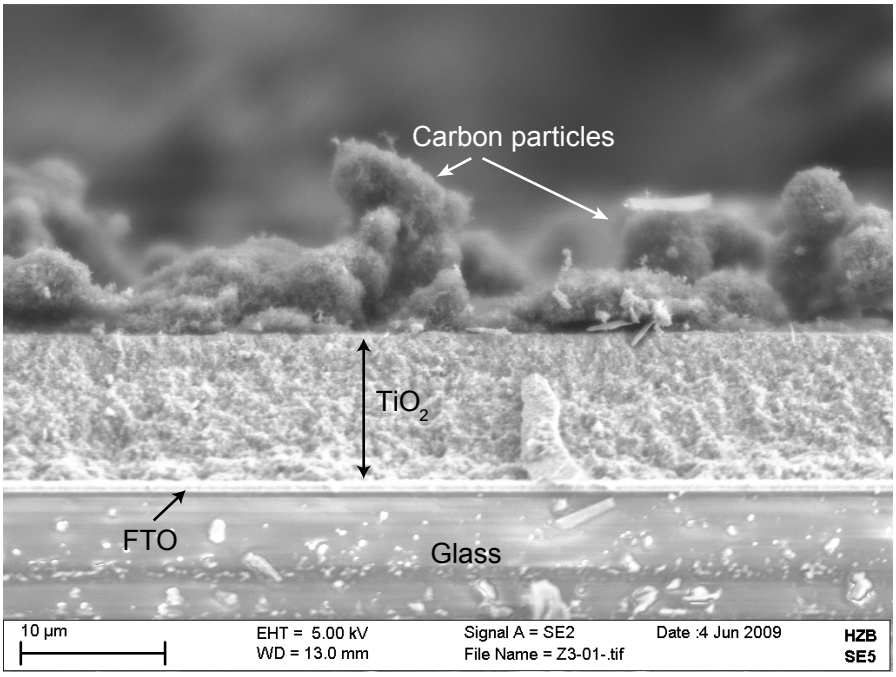

Figure 3.6: SEM image of a carbon layer on top of the screen-printed TiO_2 film.

3.1.3 Cell assembly

At this point, the PTFE tape was removed and the platinized counter electrode or a FTO glass was pressed on top of the front electrode with the help of two spring clamps and fixed with epoxy resin. The cell was contacted by soldering a copper wire to electrical tape (Scotch 3M) adhered to the FTO contact area on both front- and counter electrode. A low-viscous silver paste (Hans Wolbring GmbH) was deposited on the tape and the copper wire to ensure an adequate electric contact.

3.1.4 Preparation of subset devices

TiO_2 layers from paste DSL18NR-T (Dyesol) were deposited on quartz glass (Schröder Spezialglas, $d = 1$ mm) and sensitized with N719 in the same way as for the solar cells (Sec. 3.1.1.2). In this case, no $TiCl_4$ post-treatment was performed for these device subsets. Also the electrolyte film was applied according to the procedure described above (Sec. 3.1.1.6).

3.1.5 Preparation of ZnO films

Layers of ZnO were prepared via screen-printing in a similar way as for TiO_2. A paste from ZnO (nanopowder, Aldrich) was prepared by mixing 6 g of the powder with 9 g of polyethylene glycol, 0.1 mL acetic acid, 5 mL ethanol, and 5 mL of terpineol. This mixture was then milled at 400 rpm for 5 hours, resulting in a vicious and homogeneous paste. The paste was screen-printed on glass substrates (Corning 7059, $d = 0.5$ mm) according to the procedure described in Section 3.1.1.2. The layers were sintered at 450 °C for 30 min followed by a cooling down under ambient atmosphere. Surface profiles obtained with DEKTAK revealed a layer thickness of ca. 8 μm. A porous structure of interconnected particles was identified from SEM images as depicted in Figure 3.1.

3.1.6 Preparation of ZnO rods

Prior to the growth of ZnO nanorods, a 50 nm thick ZnO film was deposited as a seed layer on the glass substrate (Schott AF45, $d = 0.5$ mm) by a spray-pyrolysis

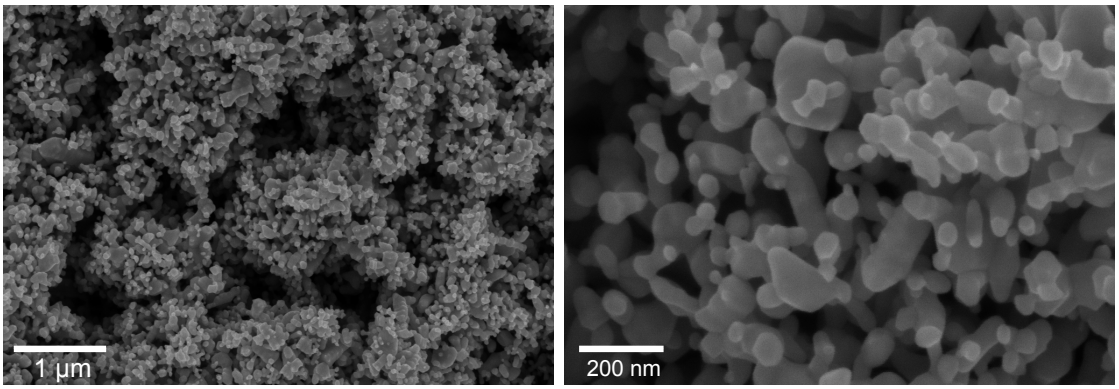

(a) (b)

Figure 3.7: SEM image of a screen-printed, mesoporous ZnO layer on glass (a). The higher magnification reveals a porous structure of interconnected particles (b).

method [157]. At a substrate temperature of 400 °C, a 20 mM precursor solution of zinc acetate (Sigma-Aldrich) in ethanol was sprayed over the substrate for 10 min with nitrogen as carrier gas. The samples were then heated at 450 °C for 30 min. The nanorods were grown onto this substrate by chemical bath deposition in an aqueous solution of 0.01 M $Zn(NO_3)_2$ (Fluka) and 0.4 M NaOH (Merck) at 80 °C for 50 min [158,159]. The sample was rinsed in purified ethanol after deposition and then annealed under ambient atmosphere at 450 °C for 30 min.

The ZnO films and nanorods were sensitized for 2 h 30 min in a 0.125 mM dye solution (N719 or black dye) with ethanol as solvent.

3.2 Time Resolved Microwave Conductivity measurements (TRMC)

The TRMC technique allows the characterization of nanoporous systems such as DSC, providing information on charge carrier kinetics for injection as well as recombination processes. The TRMC signal, $(\Delta P(t)/P)$, is the relative change of the microwave power reflected by the sample induced by a photogenerated change of the conductivity $(\Delta\sigma(t))$ [160].

The change of the photoconductivity is proportional to the reflected microwave

signal:

$$\frac{\Delta P(t)}{P} = A\Delta\sigma(t) \tag{3.1}$$

where A is a sensitivity factor depending on the experimental configuration and the electrical parameters of the sample [161]:

$$A = \left(\frac{1}{R(\sigma)}\right)\left(\frac{\partial R(\sigma)}{\partial \sigma}\right) \tag{3.2}$$

where R is a reflection coefficient defined by the relationship of the microwave signal reflected by the sample $P(\sigma)$ to the incoming microwave power P_{in}. R depends on σ, the geometry of the measurement setup and the microwave frequency. The sensitivity factor A can be determined from the reflection coefficient R at different conductivity values (σ) with a fixed geometry of the experimental setup.

Due to the non-uniformity of the initial induced carrier distribution and the charge-carrier decay processes (e.g. surface recombination), the photoconductivity can be non-uniform. The generalization of Eq. 3.1 to a non-uniform photoconductivity $\Delta\sigma(z,t)$ is:

$$\frac{\Delta P(t)}{P} = \int_0^d A(z)\Delta\sigma(z,t)dz \tag{3.3}$$

where $A(z)$ is the generalized sensitivity coefficient for a non-uniform response and d is the thickness of the sample.

In general, the change in TRMC signal $\Delta P(t)/P$ with time is due to the decay of photoconductivity and the change in distribution of the excess conductivity with time [160]. Two limiting cases of Eq. 3.3 are:

1. If the sensitivity factor A does not depend on the position on the z-axis (homogenity of A), the signal is proportional to the photoconductance ΔS:

$$\frac{\Delta P(t)}{P} = A\int_0^d \Delta\sigma(z,t)dz = A\Delta p_t(t)(u_n + u_p)q = A\Delta S(t) \tag{3.4}$$

with the total amount of excess minority charge carriers

$$\Delta p_t(t) = \int_0^d \Delta p(z,t)dz \tag{3.5}$$

and the mobility of electrons (u_n) and holes (u_p).

2. If the excess conductivity is a stationary distribution $\Delta\sigma_0(z)$ with the decay behavior $f(t)$ given by:

$$\Delta\sigma(z,t) = \Delta\sigma_0(z)f(t) \tag{3.6}$$

follows with Eq. 3.3:

$$\frac{\Delta P(t)}{P} = f(t)\int_0^d A(z)\Delta\sigma_0(z)dz \tag{3.7}$$

From Eq. 3.7 it can be concluded that the time dependence of the TRMC signal reflects the time dependence of the conductance.

For the measurements presented here it is evident that case 1 is valid.

In general, the TRMC signal is determined by all mobile excess species; however, in the case of TiO_2, it will be assumed that only electrons at the bottom of the conduction band with mobility u_n contribute to the photoconductance [162]:

$$\frac{\Delta P(t)}{P} = A\Delta S(t) = Aq\Delta N(t)u_\mathrm{n} \tag{3.8}$$

The total number of excess electrons with mobility u_n at time t, ΔN(t), refers to an integration of the excess electron concentration, Δn(t), only over the thickness d of the sample (1-dimensional model). Any process that decreases the number of excess electrons in the conduction band leads to a decay of the photoconductivity.

For the analysis of the measurement signal several contributions have to be taken into account according to the experimental conditions:

- The amplitude of the TRMC signal $A_{10\mathrm{ns}}$, i.e. the maximum signal height after 10 ns. This parameter describes the product of the amount of excess electrons at time t = 10 ns, $\Delta N_{10\mathrm{ns}}$, and the mobility of electrons u_n. Therefore, the signal is sensitive to:
  1. the amount of absorbed excitation photons.
  2. fast decay processes which occur during the excitation (0 - 10 ns).
  3. the mobility of electrons.

It is important to note that the TRMC signal reflects the kinetics of excess electrons. The kinetics of the corresponding positive charges are only observed as long

as they influence electron kinetics by recombination.

3.2.1 TRMC-Setup

Transient photoconductance measurements in the microwave frequency range were performed by the TRMC technique using a K_a-band (28 - 40 GHz) apparatus as described previously [160, 161]. A scheme of the setup is given in Figure 3.8.

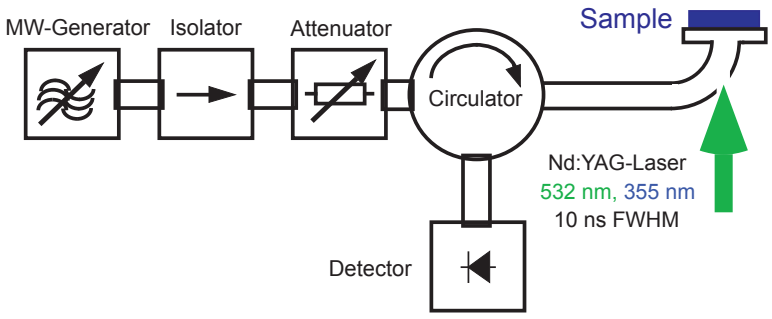

Figure 3.8: Scheme of the K_a-band setup for the TRMC-measurements.

The excitation occurred by 10 ns (FWHM) pulses of a Nd:YAG laser at wavelengths of 532 nm or 355 nm with a diameter of about 3 mm. The excitation intensity was adjusted by the use of calibrated filters. External potentials were applied by connecting the front contact of the cell with the working electrode, and the back contact to the combined counter and reference electrode of the potentiostat (Wenking POS 73). The potentials were set at 0.1 V steps for the regime from +0.6 to -0.6 V.

The setup consisted of a microwave generator (Gunn diode) which emitted in the frequency range 28 - 40 GHz (K_a-band) with a maximum power of 150 mW and was protected against perturbing back reflections from the remaining microwave circuit through an isolator. After the microwave radiation passed through an attenuator, the radiation reached the sample via a wave guide system, a circulator, and a switch. After reflection from the sample, the microwaves reached the detector.

The detector consisted of an antenna operating as a diode, which received the high-frequency electrical alternating field, rectified it and transformed it into a voltage which increased monotone with the received radiated power.

3.3 Current-voltage measurements

The Current-Voltage (I-V) characteristics of the solar cells were determined by using a solar simulator (VOSS Electronic GmbH, WXS-140S-Super). Illumination conditions corresponding to the standard AM1.5G spectrum were simulated by the combined use of a 100 W xenon lamp and a 120 W halogen lamp. This standard spectrum is characterized by the so called Air Mass (AM), which is the path length that light takes through the atmosphere normalized to the shortest possible path length (AM = $1/\cos\psi$, where ψ is the solar zenith angle). The G stands for *global* and includes both direct and diffuse radiation. Measurements were performed with an irradiation intensity of 100 mW/cm^2 and 10 mW/cm^2. The latter was achieved using a neutral density filter. The system was periodically calibrated with a Si solar cell as reference. The I-V characteristics were obtained by applying an external potential bias to the cell and by measuring the generated photocurrent with a measuring unit (Keithley SMU 238). The temperature of the sample holder was set constant by a thermostat at a given value, normally set at 23 °C for standard measurements.

The characteristic variables determining the solar cell efficiency are the open circuit voltage V_{OC}, the short circuit current I_{SC}, and the fill factor FF, which is given by the ratio of the maximum power output of the solar cell and the product of open circuit voltage and short circuit current. The solar to current conversion efficiency η is defined as the ratio of the maximum power to the incident irradiation power P_{in}:[1]

$$\eta = \frac{P_{\mathrm{max}}}{P_{\mathrm{in}}} = \frac{FF \cdot V_{\mathrm{OC}} \cdot I_{\mathrm{SC}}}{P_{\mathrm{in}}} \tag{3.9}$$

[1]Error margins for η were approximated by: $\frac{\Delta\eta}{\eta} \approx 3\frac{\Delta I}{I} + 3\frac{\Delta V}{V} + \frac{\Delta P_{\mathrm{in}}}{P_{\mathrm{in}}} + \frac{\Delta A_{\mathrm{TiO_2}}}{A_{\mathrm{TiO_2}}} \approx 6\%$

3.4 Impedance spectroscopy

Impedance measurements for NSCSC were performed with a computer controlled potentiostat (Gamry 600) equipped with an impedance spectra analyzer. The impedance spectra were acquired in the dark and under illumination (by laser light diodes at 510 nm and ca. 10 mW/cm^2) as a function of the applied potential. The amplitude of the ac signal used was 20 mV, and the frequency ranged between 10 kHz and 10 mHz; dc potentials ranged between 0 and -0.6 V.

In impedance spectroscopy (IS), a small potential modulation is superimposed on the fixed potential polarizing the cell and the frequency of this potential modulation is swept. The harmonic current response of the cell (amplitude and phase shift with respect to the potential modulation) is measured as a function of the modulation frequency. The impedance is defined as the ratio between the harmonic potential modulation and the harmonic current response. This complex quantity is frequency dependent and can be represented by the use of a complex notation [120]:

$$\hat{Z}(\omega) = \frac{\hat{V}(\omega)}{\hat{I}(\omega)} \tag{3.10}$$

where $\hat{V}(\omega)$ is the potential modulation and $\hat{I}(\omega)$, the current response at a certain angular frequency, ω.

Impedance spectra can be analyzed by the use of equivalent circuits based on linear circuit elements: a resistor, a capacitor, and an inductor. For a resistor (R), the impedance is a real value, independent of modulation frequency, while capacitors (C) and inductors (L) yield an imaginary impedance, whose values are frequency dependent.

Impedance spectroscopy can be used to study complete dye-sensitized solar cells [84, 163, 164] or cell components such as a blocking layer on conducting glass [112]. The impedance response of a DSC is related to the response of various components of the device, which can be modeled by an equivalent circuit which contains linear elements representing all of the processes taking place in the DSC (Figure 3.9). The mesoporous electrode can be modeled using a distributed equivalent circuit (a transmission line) with appropriate elements [165–167]. The following parameters can be obtained by fitting the equivalent circuit to the impedance:

series resistance, charge transfer resistance of the counter electrode, diffusion resistance of the electrolyte, the resistance of electron transport and recombination in the TiO_2, and the chemical capacitance of the porous TiO_2 electrode as a function of the applied potential.

The impedance associated with shunting via the substrate (i.e., electron transfer to I_3^-) appears in parallel with the transmission line. The impedance associated with transport of ions in the electrolyte is modeled by a finite Warburg element which appears in series with the charge transfer resistance associated with electron transfer at the cathode. The remaining elements are the double layer capacitance of the cathode and the series resistance of the DSC.

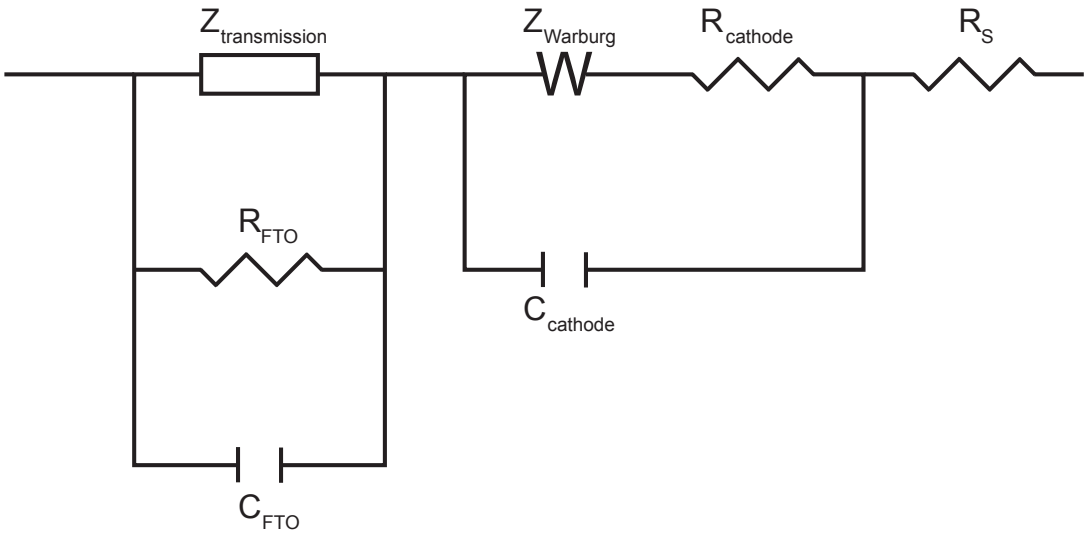

Figure 3.9: Equivalent circuit of a DSC. $Z_{transmission}$ represents the impedance of the TiO_2 layer, R_{FTO} and C_{FTO} are associated with the anode/electrolyte contact, $Z_{Warburg}$ describes the diffusion of I_3^- and I^-, $R_{cathode}$ is the charge transfer resistance of the cathode, $C_{cathode}$ is the double layer capacitance of the cathode and R_S is the total series resistance of the cell.

The transport and interfacial transfer of electrons in the mesoporous TiO_2 layer can be modeled using a distributed network of resistive and capacitive elements in the form of the finite transmission line shown in Figure 3.10.

The resistances in the transmission line are interpreted in terms of the relationship between the electron flux (the current) and the gradient of the quasi-Fermi level [168, 169]. Similarly, the capacitance elements are related to the ability of

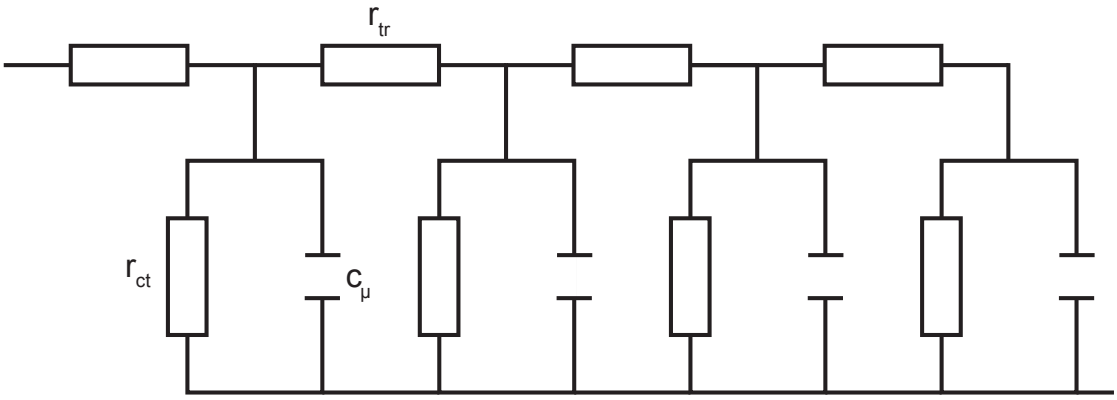

Figure 3.10: Transmission line equivalent circuit representing electron transport in the TiO_2 layer. r_{ct} is the distributed charge-transfer resistance, r_{tr} the electron-transport resistance and c_μ the chemical capacitance (ability of the TiO_2 layer to store electronic charge).

the TiO_2 layer to store electronic charge (the "chemical capacitance") [170, 171]. In the case transport occurs by diffusion and only conduction band electrons are involved, the distributed and corresponding total resistive and capacitive elements for the TiO_2 layer are given by [168]:

$$r_{\mathrm{tr}} = \frac{k_B T}{A q^2 n_c D_0} \qquad R_{\mathrm{tr}} = r_{\mathrm{tr}} d_{\mathrm{film}} \tag{3.11}$$

$$r_{\mathrm{ct}} = \frac{k_B T \tau_0}{A q^2 n_c} \qquad R_{\mathrm{ct}} = \frac{r_{\mathrm{ct}}}{d_{\mathrm{film}}} \tag{3.12}$$

$$c_\mu = A q^2 g(E) \qquad C_\mu = c_\mu d_{\mathrm{film}} \tag{3.13}$$

where d_{film} is the film thickness, A the electrode area, R_{tr} the total electron-transport resistance, R_{ct} charge-transfer resistance of the charge recombination process of electrons in the TiO_2 layer, $g(E)$ the density of electron states in the band gap and C_μ the chemical capacitance. With the assumption that the stored electronic charge is predominantly in electron trap states (i.e., $n_t \gg n_c$), the electron diffusion length can be expressed as:

$$L_n = (D_0 \tau_0)^{1/2} = \left(\frac{R_{\mathrm{ct}}}{R_{\mathrm{tr}}}\right)^{1/2} d_{\mathrm{film}} \tag{3.14}$$

The effective electron lifetime is given by:

$$\tau_n = R_{\mathrm{ct}} C_\mu \tag{3.15}$$

The impedance of the transmission line is written as [168]:

$$Z = \left[\frac{R_{\mathrm{tr}} R_{\mathrm{ct}}}{1 + \frac{j\omega}{\omega_{\mathrm{ct}}}}\right]^{1/2} \coth\left[\left(\frac{\omega_{\mathrm{ct}}}{\omega_{\mathrm{tr}}}\right)\left(1 + \frac{j\omega}{\omega_{\mathrm{ct}}}\right)^{1/2}\right] \tag{3.16}$$

where

$$\omega_{\mathrm{ct}} = \frac{1}{R_{\mathrm{ct}} C_\mu} \tag{3.17a}$$

$$\omega_{\mathrm{tr}} = \frac{1}{R_{\mathrm{tr}} C_\mu} \tag{3.17b}$$

are the characteristics reaction- and transport frequency, respectively.

3.5 Scanning Microscope for Semiconductor Characterization (SMSC)

A scanning laser spot technique was used to obtain spatially resolved photocurrent images. The Scanning Microscope for Semiconductor Characterization (SMSC) was an inverted microscope with a scan-stage [72, 172, 173]. A schematic representation of the equipment is shown in Figure 3.11. The cell was mounted onto the scan-stage, which allowed the movement of the sample in the x and y directions with a resolution of 1 μm. In the case of DSC, the photocurrent was generated by illumination with a He/Ne-laser ($\lambda = 632.8$ nm) focused onto the cell surface by a microscopic lens and the light intensity was adjusted to 130 mW/cm^2 by neutral grey filters. To monitor the laser induced photocurrent, the laser light was chopped at 20 Hz and a lock-in amplifier (Model 5210, EG&G) was used. The image resolution depended on the laser spot focused through the microscope objectives, and the scan step width. The spatially resolved photocurrent images were obtained by measuring the photocurrent at different laser spot positions, while these positions were altered step by step. To obtain a reasonable time frame for the measurements

of cells with an area of ca. 1 × 1 cm^2 the laser spot diameter was adjusted to 25 μm with a step width of 40 μm; however, resolutions of less than 3 μm can be obtained with this technique.

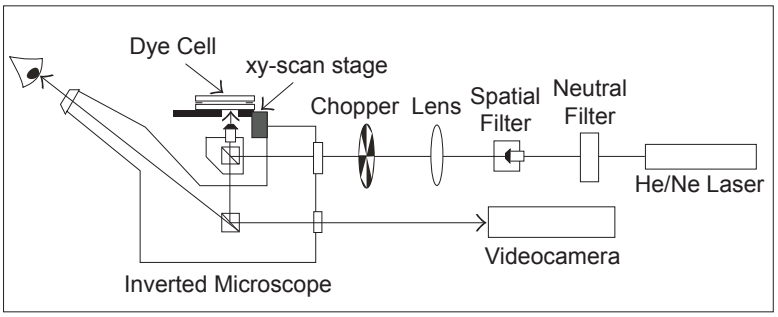

Figure 3.11: Scheme of the Scanning Microscope for Semiconductor Characterization (SMSC); adapted from [67].

3.6 Step profilometer

Film thickness of the screen printed TiO_2 was determined using a DEKTAK 8 Advanced Development Profiler (Veeco Instruments Inc.), which measured the vertical displacement of a diamond tipped stylus electromechanically. The gantry moves the stylus with an adjustable speed and stylus force across the surface of the sample. A stylus with a radius of 12.5 μm and force of 3 mg was used. The vertical resolution depended on the measurement range and varied between 0.1 nm for a maximum layer thickness of 6.5 μm and 4 nm for layers of 262 μm.

3.7 Scanning Electron Microscopy (SEM)

SEM images were acquired with a field emission microscope LEO1530 (Zeiss Gemini), in a range of 2 - 10 keV. The maximum resolution is 1 nm at an electron energy of 20 keV, at 1 keV about 3 nm. In addition to the standard secondary electron detector, the microscope was equipped with an energy dispersive X-ray spectrometer for elementary analysis (EDX).

4 Results and Discussion

The following chapter is divided into three Sections:

Section 4.1 deals with the measurements performed on quasi-solid-state dye-sensitized solar cells (NSCSC) and the results obtained from transient photoconductance measurements in the microwave frequency range (Section 4.1.1), the characterization of the devices by current-voltage analysis (Section 4.1.2), the space-resolved characterization of photocurrent distribution in the solar cells (Section 4.1.3) and the characterization by impedance spectroscopy (Section 4.1.4).

Section 4.2 presents TRMC studies of subset devices of the solar cell dependent on the electrolyte components.

The investigation of charge carrier transport and kinetics in TiO_2 films and powders is extended to ZnO films and nanorods in Section 4.3.

4.1 Nano Surface Conductivity Solar Cell (NSCSC)

4.1.1 Transient photoconductance measurements in the microwave frequency range

4.1.1.1 Effects of degradation

Figure 4.1 displays TRMC signals induced by 532 nm light pulses in a double-logarithmic representation.

The maximum initial amplitude of the TRMC signals at ∼10 ns was approximately proportional to the square root of the excitation density. This indicates a fast, non-linear decay process which dominates the decay within the duration of the laser pulse (probably electron-hole recombination).

After constant exposure to simulated sunlight for 18 h at 100 mW/cm^2, the cell showed strong degradation effects, where the initial efficiency decreased by 85%

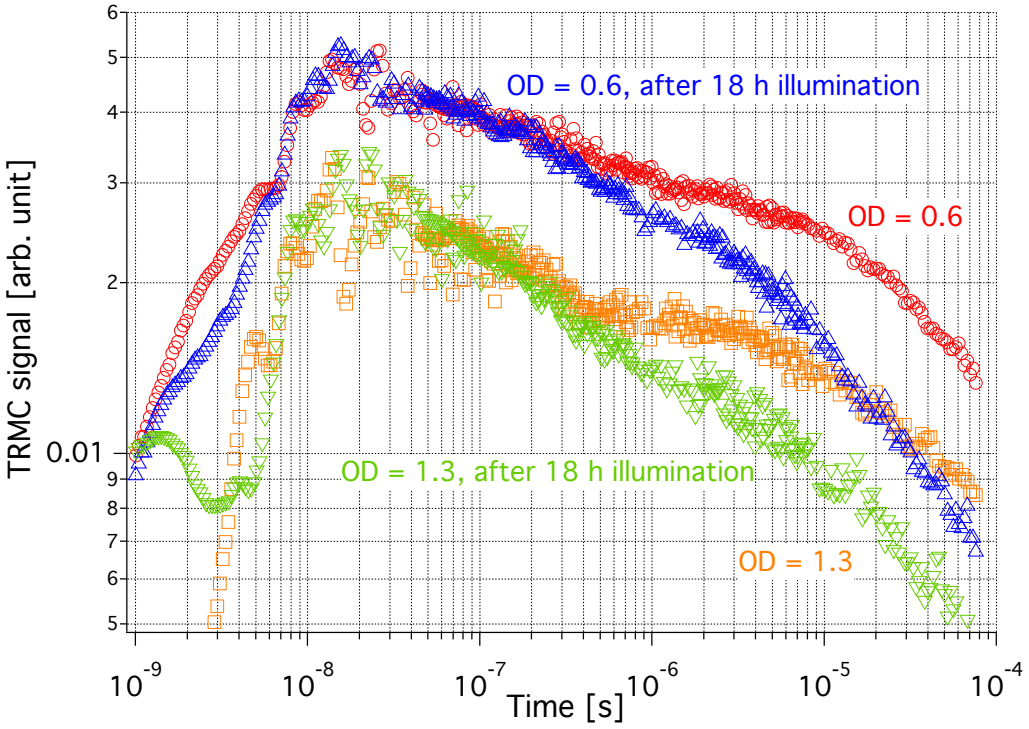

Figure 4.1: TRMC signals of a quasi-solid-state dye-sensitized solar cell in a double-logarithmic plot induced by laser pulses at 532 nm and excitation densities of 20 mJ/cm^2 (OD = 0.6) and 5 mJ/cm^2 (OD = 1.3).

from $\eta_1 = 1.3\%$ to $\eta_2 = 0.2\%$.

Studies on the photoinduced degradation of conventional liquid dye-sensitized solar cells revealed that a variety of processes contribute to the degradation of a solar cell. The connection to specific surface states in TiO_2 was demonstrated by Tributsch to influence the degradation of the dye [69]. Furthermore, if the chemical binding of the Ru-complex was ideal, the oxidized dye would be stable until regeneration by the redox couple. The formation of a temporary interfacial Ti^{3+}-ligand-Ru^{2+} charge-transfer complex (during photoinduced electron transfer to TiO_2) between the dye and Ti^{3+} states was proposed to explain the stability on TiO_2 surfaces [68, 69]. However, if the dye was chemisorbed to states where the regeneration was disturbed and not ideal, irreversible side reactions could occur, leading to a further negative influence on the cell performance.

Additional negative factors were found in the use of unstable electrolytes [72] or

platinum counter electrodes [77].

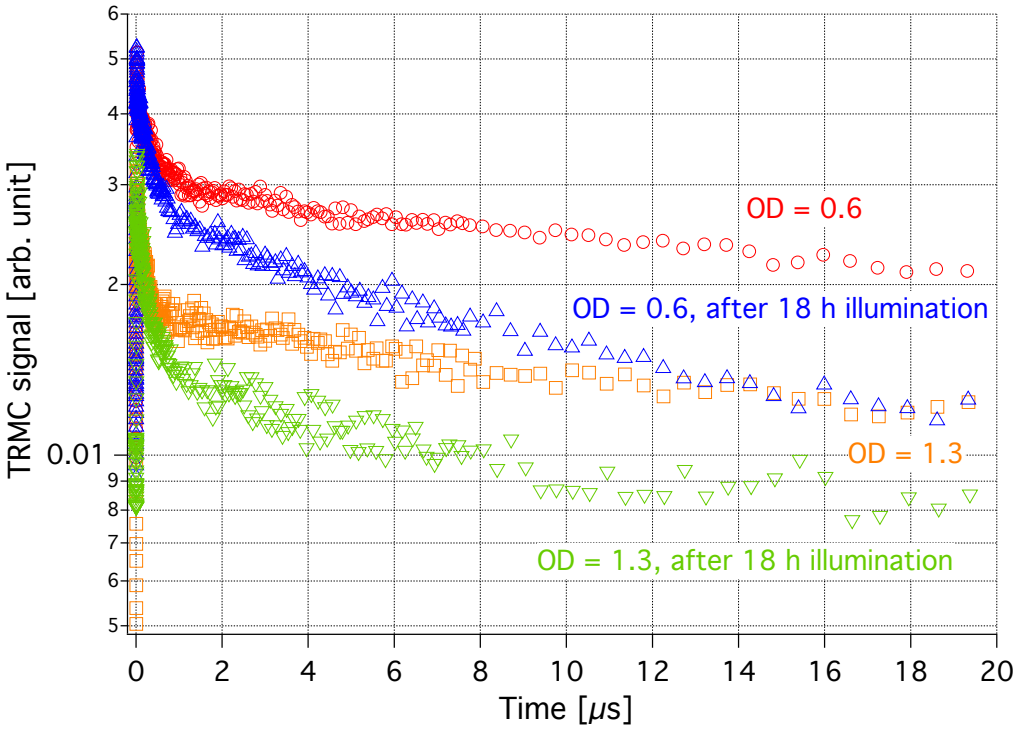

Figure 4.2: TRMC signals of a quasi-solid-state dye-sensitized solar cell in a semi-logarithmic plot induced by laser pulses at 532 nm and excitation densities of 20 mJ/cm^2 (OD = 0.6) and 5 mJ/cm^2 (OD = 1.3).

The decay of the TRMC signal allowed further insights on the degradation processes involved. Assuming that the number of excited dye molecules and therefore the number of electrons that could be injected into the conduction band of the TiO_2 decayed during degradation, the amplitude of the TRMC signal (A_{10ns}) should also decay as a result of the reduced number of free excess charge carriers in the degraded cell. However, the amplitude showed no significant changes for the degraded cell. This led to the hypothesis that the initial excitation of the dye remained the same, whereas the transport of charges subsequent to the excitation were either repressed or influenced by additional decay processes. The signal of the degraded cell decayed faster in the time regime from $\sim$ 1 - 100 μs, which again indicates an additional or enhanced decay channel.

The faster decay of the degraded cell in the time regime of ca. 1 - 2 μs after

excitation was clearly noticeable in Figure 4.2. The curve approached a straight line for the time regime up to 20 μs, which corresponded to a first order decay process in this representation. The differences in the time-dependent decay of the curves indicates complex recombination- and trapping processes.

4.1.1.2 External potential applied to the working solar cell

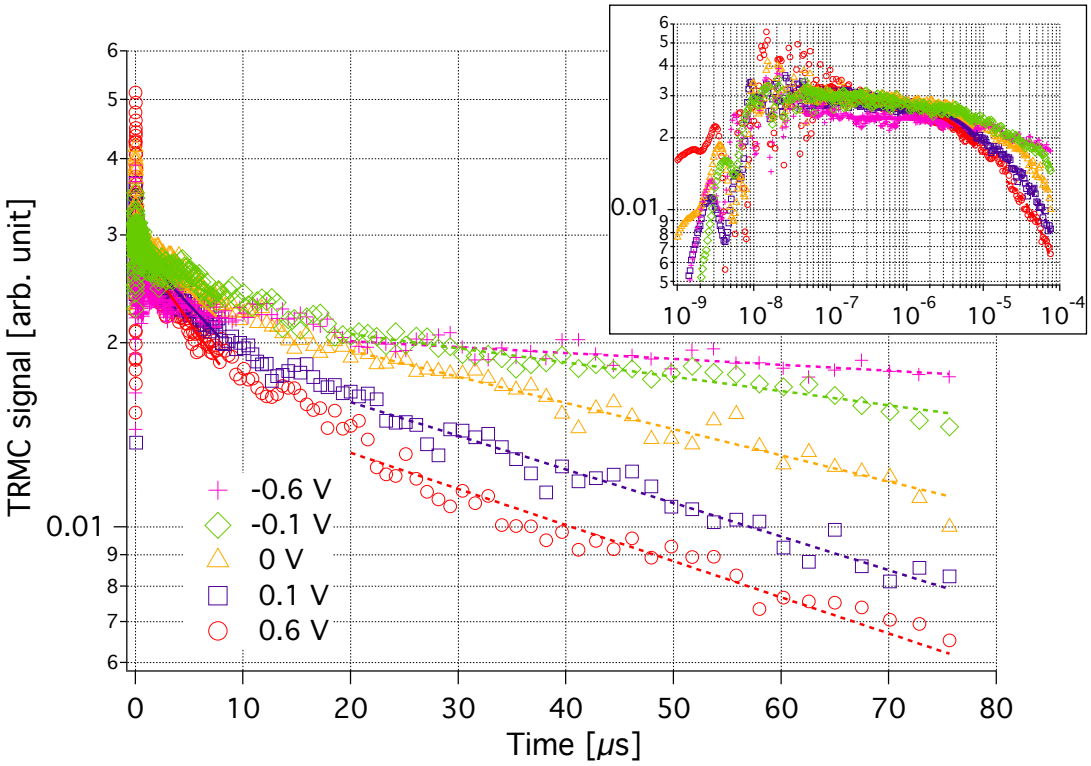

Figure 4.3: Semi-logarithmic plot of the TRMC signal of a quasi-solid-state dye-sensitized solar cell induced by laser pulses at 532 nm and an excitation density of 20 mJ/cm^2. Signals are plotted for an applied external potential to the cell as indicated. Included are the exponential fits of the decay times for time intervals 200 ns to 8 μs (solid lines) and 20 μs to 75 μs (dashed lines). The insert shows the signals in a double-logarithmic representation.

The analysis of charge carrier kinetics was performed by applying an external potential to the cell during the TRMC measurements. External potentials were applied by connecting the front contact of the cell with the working electrode, and the back contact to the combined counter and reference electrode of the poten-

tiostat (Wenking POS 73). The potential was varied in the regime from +0.6 to -0.6 V with steps of 0.1 V. The TRMC signals exhibited a potential dependence, where the decay was rather slow in the short time range, up to a few microseconds (Figure 4.3). Furthermore, this decay was slower than the previously reported power-law decay behavior of excess charge carriers in dye sensitized TiO_2 films, usually ascribed to dispersive transport and recombination of electrons in the TiO_2 film [174].

An appreciable decay of the TRMC signal was observed after about 5 μs depending on the applied potential. The TRMC signals are presented in Figure 4.3 together with the results of the exponential fits for the time interval between 20 - 75 μs showing an increase of the decay time with decreasing external potential; reaching the maximum at -0.6 V and the minimum at +0.6 V.

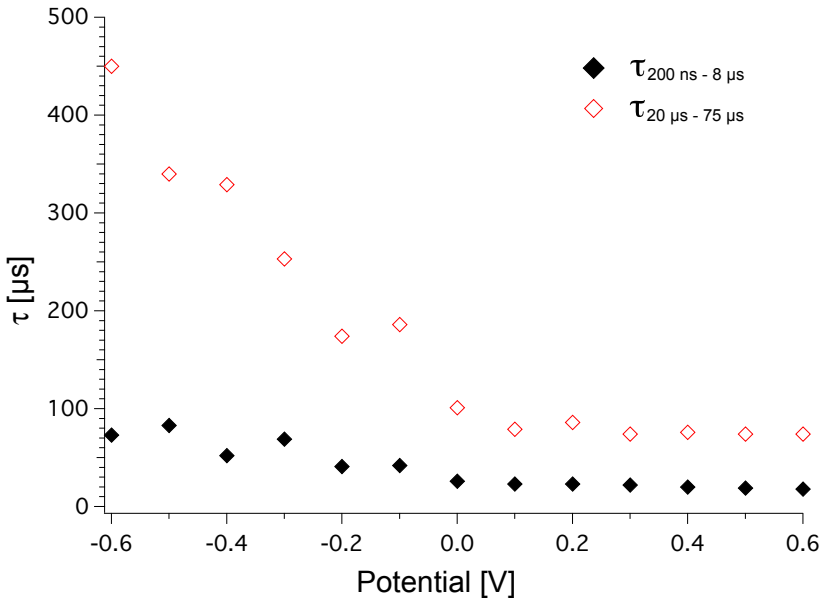

Figure 4.4: Lifetime τ of the photogenerated charge carriers as a function of the applied external potential. Solid diamonds (open diamonds) represent the lifetime from the exponential fit of the TRMC signal for the time regime of 200 ns to 8 μs (20 μs to 75 μs).

Figure 4.4 shows the lifetimes for the two time intervals, which were chosen for a convenient description from 200 ns to 8 μs and from 20 μs to 75 μs as a function of the applied external potential. The lifetime of the photogenerated charge carriers

decreases with increasing applied potential. There are in principle three decay channels for the electron injected from the dye into the TiO_2: (1) The injected electron can recombine with the oxidized dye, (2) with the oxidized redox species in the electrolyte, and (3) as well be injected into the front contact. The potential dependence of the decay suggests that the decay was mainly due to the injection of charges into the front contact because the predominant influence of an applied external potential was at the FTO/TiO_2 interface. In the short time range, a change in decay time from $\sim$ 20 μs at +0.6 V to $\sim$ 80 μs at -0.6 V was observed, while in the long time range it increased from $\sim$ 75 μs at +0.6 V to $\sim$ 450 μs at -0.6 V.

The lifetime reached its maximum at an external potential of -0.6 V. This potential lay near the open circuit potential of the cell. The photocurrent density in this potential regime was minimal, i.e. the potential dependent decay observed was limited by the injection of electrons into the front contact. The field in the space charge region at the FTO/TiO_2 interface controlled this injection. The onset of the decay at about 5 μs could be interpreted as the time required for the excess charge carriers to reach the front contact and to enable electron injection into the FTO contact.

4.1.2 Modifications to the cell concept: Characterization by current-voltage measurements

The following Section presents results obtained from the Current-Voltage (I-V) analysis of the solar cells. A number of modifications were applied to the basic concept of the NSCSC and the resulting influences on device performances were evaluated by comparing the I-V characteristics. Some examples of these measurements will be presented.

4.1.2.1 Platinum vs. carbon counter electrode

Figure 4.5 compares the I-V curve characteristic of a typical NSCSC with a platinum counter electrode (Figure 4.5(a)) to a cell with a carbon counter electrode (Figure 4.5(b)).

The higher efficiency of the carbon NSCSC was mainly due to a better short

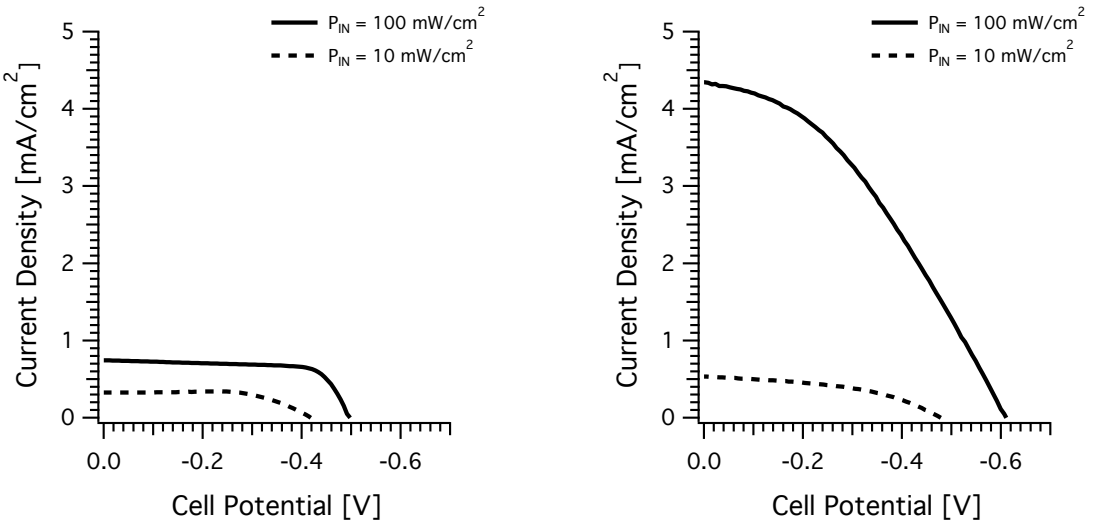

(a) Platinum counter electrode

(b) Carbon counter electrode

P_{IN} /mWcm^{-2}	I_{SC} /mAcm^{-2}	V_{OC} /mV	FF /%	η /%
10	0.33	-418	65	0.90±0.06
100	0.74	-498	71	0.26±0.02

P_{IN} /mWcm^{-2}	I_{SC} /mAcm^{-2}	V_{OC} /mV	FF /%	η /%
10	0.54	-479	45	1.16±0.07
100	4.34	-611	38	1.01±0.06

Figure 4.5: Influence of the counter electrode on the photo I-V curve characteristic of a quasi-solid-state dye-sensitized solar cell.

circuit current which increased by ca. 61% for illumination with 10 mW/cm^2 and nearly six times for illumination with 100 mW/cm^2. The open circuit potential increased by 15% for the reduced light intensity and 23% for the high illumination. The lower open circuit voltage of the cell containing the platinum electrode could be attributed to weakly bound Pt-clusters that dissolved after contact with the electrolyte film, then diffused to the front electrode where they enhanced the recombination reaction of electrons from the TiO_2 conduction band and thus lowering the V_{OC}.

However, the fill factor decreased significantly for both light intensities when carbon was employed. This could be due to a higher series resistance of the carbon layer, which was reflected by the moderate slope of the I-V curve near the open circuit potential.

The cell showed an overall higher efficiency for reduced light intensities. This indicates an increased loss of charge carriers with increasing number of excess charge carriers. Most probably, a saturation in transport of the positive charge to

the counter electrode occurs for high light intensities. Therefore, the short circuit density might be limited by both the recombination of injected electrons $e^-_{TiO_2}$ with the oxidized dye D^+ (Eq. 2.35) as well as with the oxidized redox species R^+ (Eq. 2.36).

4.1.2.2 Influence of the $TiCl_4$ post-treatment

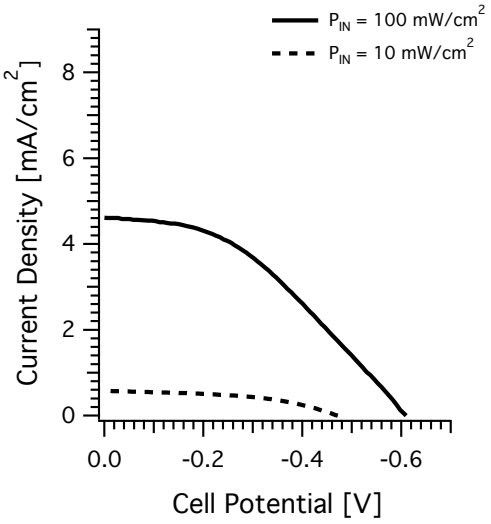

(a) Carbon counter electrode

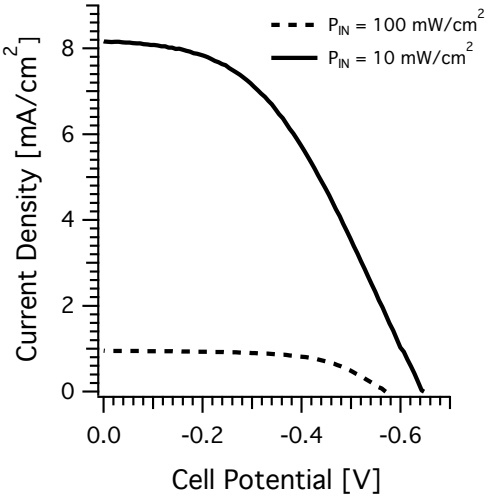

(b) $TiCl_4$ post-treatment

P_{IN} /mWcm^{-2}	I_{SC} /mAcm^{-2}	V_{OC} /mV	FF /%	η /%
10	0.58	-472	48	1.31±0.08
100	4.61	-610	40	1.12±0.07

P_{IN} /mWcm^{-2}	I_{SC} /mAcm^{-2}	V_{OC} /mV	FF /%	η /%
10	0.95	-570	60	3.3±0.2
100	8.17	-648	44	2.3±0.1

Figure 4.6: Influence of the post-treatment with $TiCl_4$ on the photo I-V curve characteristic of a quasi-solid-state dye-sensitized solar cell.

To optimize the cell, a post-treatment in a titanium(IV) chloride solution was performed on the sintered TiO_2 electrodes (Section 3.1.1.3). All cell parameters increased significantly as can be seen in the comparison of two cells with/without the $TiCl_4$ treatment in Figure 4.6. The short circuit current increased by ca. 64% for illumination with 10 mW/cm^2 and by ca. 77% for illumination with 100 mW/cm^2. The open circuit potential displayed an increase of ca. 21% and ca. 7%, accordingly. Fill factor values increased by ca. 25% and ca. 10% leading to an overall increase of the sunlight to electric power conversion efficiency of more

than 100%.

The higher short circuit density could be attributed to a downward shift (towards more positive potentials on the electrochemical energy scale) of the conduction band edge in the TiO_2; thus, leading to an additional driving force and optimized electron injection form the excited state of the sensitizer [155]. However, at the same time the shift was expected to lower the V_{OC} by reducing the distance between conduction band edge and the iodide/iodine potential. This shift was compensated by a reduced electron recombination rate; therefore, the open circuit potential was not affected negatively [175]. Moreover, the post-treatment with $TiCl_4$ was proposed to increase the surface area of the TiO_2 layer through the deposition of additional TiO_2 particles on the existing nanoporous layer [154]. Hence, a higher dye adsorption could be achieved which benefited the charge extraction efficiency.

4.1.2.3 Influence of the TiO_2 blocking layer

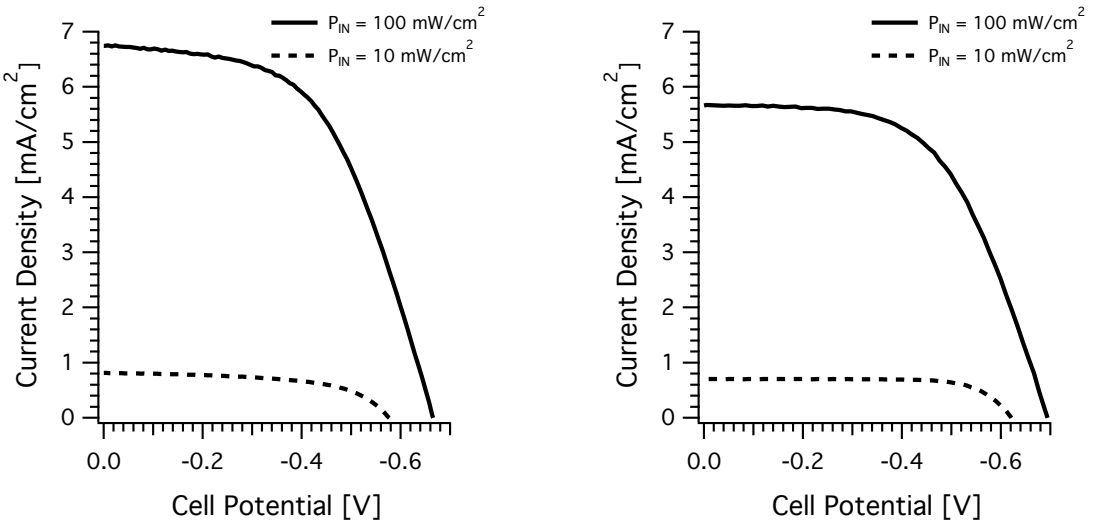

(a) $TiCl_4$ post-treatment

(b) $TiCl_4$ post-treatment + blocking layer

P_{IN} /mWcm^{-2}	I_{SC} /mAcm^{-2}	V_{OC} /mV	FF /%	η /%
10	0.81	-577	58	2.7±0.2
100	6.75	-666	54	2.4±0.2

P_{IN} /mWcm^{-2}	I_{SC} /mAcm^{-2}	V_{OC} /mV	FF /%	η /%
10	0.71	-621	73	3.2±0.2
100	5.67	-694	57	2.2±0.1

Figure 4.7: Influence of the additional compact TiO_2 layer on the photo I-V curve characteristic of a quasi-solid-state dye-sensitized solar cell.

The quasi-solid-state dye-sensitized solar cell was further modified by introducing a compact TiO_2 underlayer between the FTO substrate and the mesoporous TiO_2 layer. The purpose of this "blocking layer" was to prevent recombination reactions of electrons from the FTO substrate (e^-_{FTO}) with oxidized redox species R^+ (Eq. 2.37) by covering spaces between the colloidal particles where the substrate comes into direct contact with the redox solution [176].

Figure 4.7 displays the I-V characteristic obtained from typical quasi-solid-state dye-sensitized solar cells, where one sample (Figure 4.7(a)) was treated with an additional TiO_2 blocking layer.

Compared to the drastic increase in performance observed in Figure 4.6, the effects of the blocking layer appeared less obvious. The open circuit potential increased for both light intensities by ca. 8% and ca. 5%. This could be explained by an enhanced suppression of dark current at the FTO/electrolyte interface [154]. The fill factor increased by ca. 25% for 10 mW/cm^2 and ca. 6% for 100 mW/cm^2 which is consistent with the assumption that a V_{OC} increase caused by a decrease in the recombination rate constant should be accompanied by an increase in the fill factor [177]. The slightly decreased short circuit currents might be explained in a similar way as for studies on metal oxide passivated solid-state dye-sensitized solar cells with a p-type hole conducting medium [177]. Here, an increase of both V_{OC} and fill factor was observed while the short circuit current density decreased, which was correlated to a decreased electron injection rate. However, the increase in both fill factor and V_{OC} compensated the slightly reduced current density leading to an overall increase of the sunlight to electric power conversion efficiency by ca. 20% for the reduced light intensity (10 mW/cm^2).

4.1.2.4 Alternative dye compounds

Two different Ru-based dye complexes were tested as an alternative to the "standard" Ru-dye employed for all solar cells fabricated in this work. The dye "Z907" was a modified version of the N719 dye (Section 2.4.3), where hydrophobic properties were incorporated by adding long aliphatic chains in the ligands to overcome the possible problem of water induced desorption of the sensitizer from the TiO_2 surface [42]. The second alternative dye was the so-called "black dye" (N749), where the ligands were modified to shift the absorption response ca. 100 nm

further into the infrared regime [45].

An UV/Vis spectrum of the three sensitizers is presented in Figure 4.8.

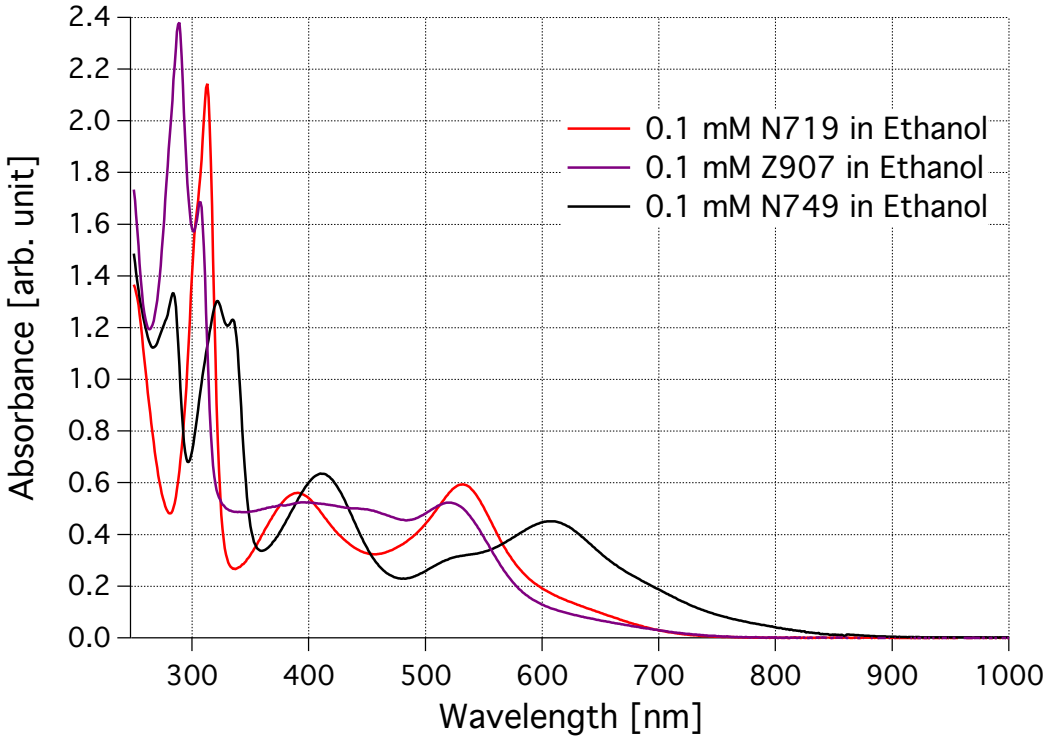

Figure 4.8: UV/Vis absorbance spectra of the Ru-sensitizers "N719", the hydrophobic "Z907" and the "black dye" (N749) (0.1 mM solution in ethanol).

Figure 4.9 compares the I-V curve characteristic of three quasi-solid-state DSC with different Ru-complexes as sensitizers. The cells with the Z907 (Figure 4.9(b)) and N749 (Figure 4.9(b)) sensitizers displayed comparable photovoltaic performance with slightly enhanced fill factor values for the Z907 dye. However, compared to the "standard" N719 (Figure 4.9(c)) sensitizer employed efficiency parameters could not be matched. The reasons for the differences in photovoltaic performance of the sensitizer are diverse. For example, the extension of the spectral response into the near-infrared region for the "black dye" might also be coupled to a shift of the LUMO to lower levels from where charge injection into the TiO_2 conduction band was hindered [64]. Furthermore, the increase of the chain length in the "Z907" dye might led to a retardation of the dye regeneration; thus, inducing a reduced device performance.

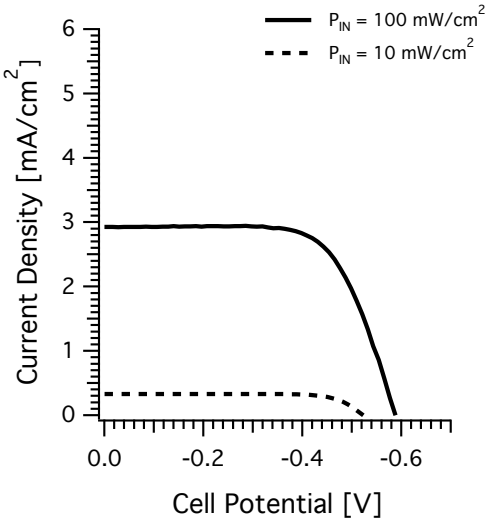

(a) Z907

P_{IN} /mWcm^{-2}	I_{SC} /mAcm^{-2}	V_{OC} /mV	FF /%	η /%
10	0.33	-523	77	1.33±0.08
100	2.93	-588	67	1.15±0.07

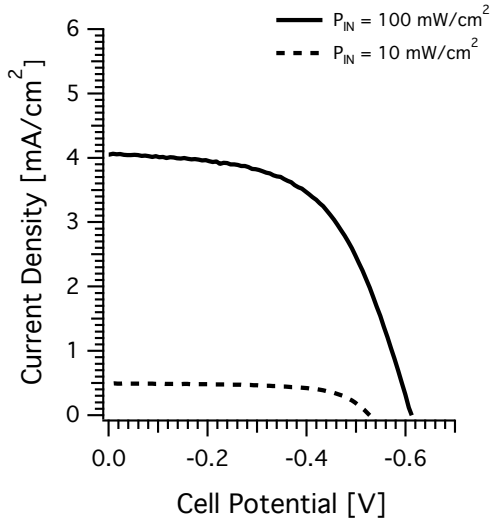

(b) N749 "black dye"

P_{IN} /mWcm^{-2}	I_{SC} /mAcm^{-2}	V_{OC} /mV	FF /%	η /%
10	0.49	-528	65	1.7±0.1
100	4.05	-612	57	1.4±0.1

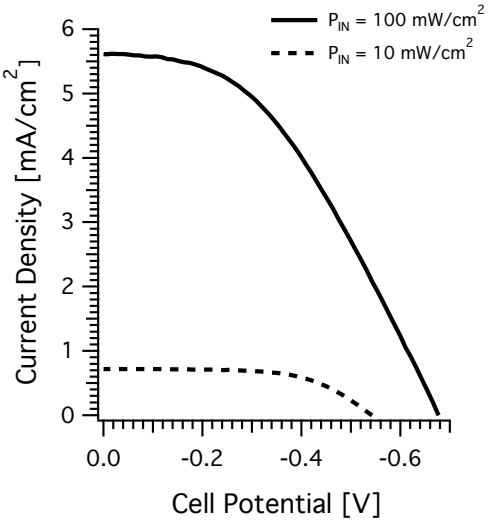

(c) N719

P_{IN} /mWcm^{-2}	I_{SC} /mAcm^{-2}	V_{OC} /mV	FF /%	η /%
10	0.72	-542	61	2.4±0.2
100	5.62	-677	42	1.6±0.1

Figure 4.9: Substitution of the dye complex and its influence on the photo I-V curve characteristic of a quasi-solid-state dye-sensitized solar cell.

4.1.2.5 Characterization of the "best" NSCSC

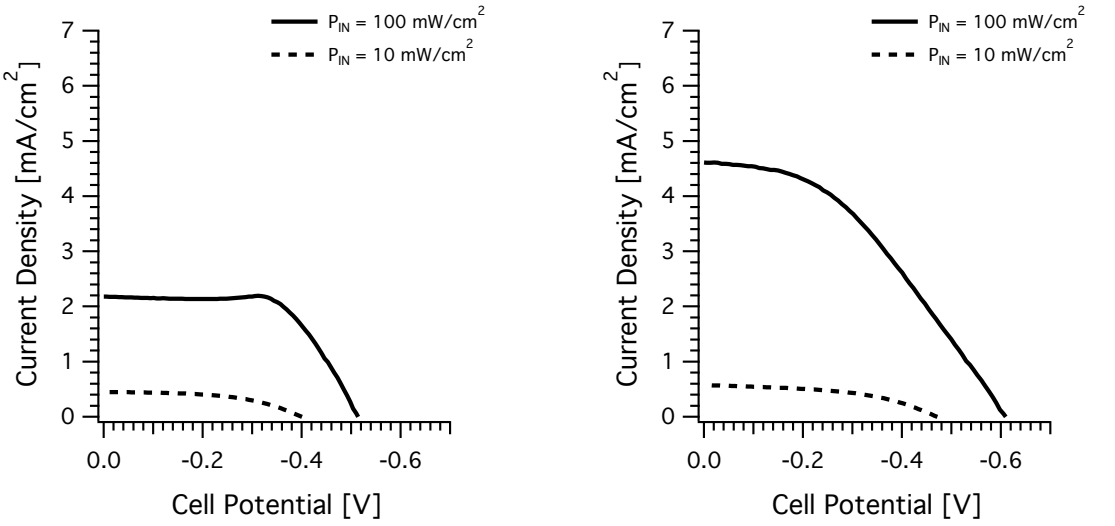

(a) Platinum

(b) Carbon

P_{IN} /mWcm^{-2}	I_{SC} /mAcm^{-2}	V_{OC} /mV	FF /%	η /%
10	0.45	-401	51	0.92±0.06
100	2.18	-514	65	0.73±0.05

P_{IN} /mWcm^{-2}	I_{SC} /mAcm^{-2}	V_{OC} /mV	FF /%	η /%
10	0.58	-472	48	1.31±0.08
100	4.61	-610	40	1.12±0.07

Figure 4.10: Photo I-V curve characteristic of the "best" quasi-solid-state dye-sensitized solar cells. Platinum vs. carbon counter electrode.

Figure 4.10 and Figure 4.11 present I-V curve characteristic of NSCSC with the highest efficiencies obtained during this work. Cells employing a platinum counter electrode reached a maximum sunlight to electric power conversion efficiency of ca. 1% (Figure 4.10(a)).

Improvements were obtained by substituting the platinum counter electrode with a carbon layer reaching an efficiency of 1.3% for the "best" cell (Figure 4.10(a)).

A more drastic improvement was achieved with a $TiCl_4$ post-treatment on the mesoporous TiO_2, which led to an increase of the overall efficiency to 3.2% (at 10 mW/cm^2) and 2.4% (at 100 mW/cm^2) for the "best" cell produced (Figure 4.11(a)).

The efficiencies were raised even slightly higher by incorporating a compact TiO_2 blocking layer, thereby reaching an overall efficiency of 3.5% (at 10 mW/cm^2) and

2.4% (at 100 mW/cm^2) for the "best" cell (Figure 4.11(b)).

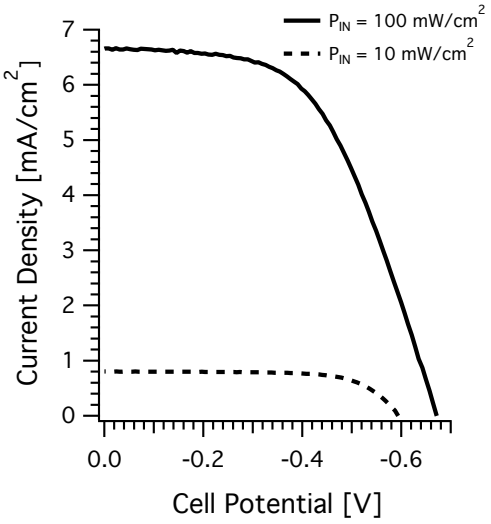

(a) $TiCl_4$

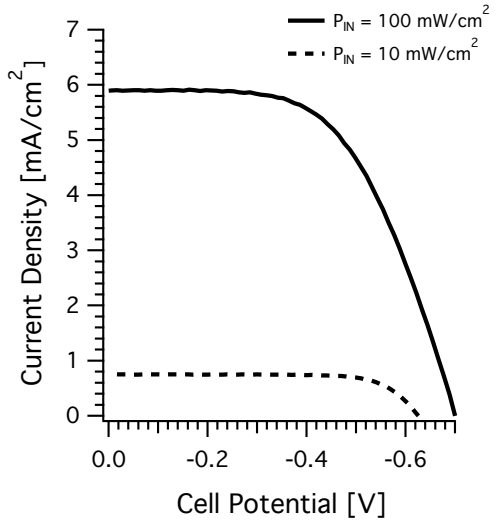

(b) $TiCl_4$ + compact TiO_2

P_{IN} /mWcm^{-2}	I_{SC} /mAcm^{-2}	V_{OC} /mV	FF /%	η /%
10	0.8	-594	70	3.3±0.2
100	6.66	-672	54	2.4±0.2

P_{IN} /mWcm^{-2}	I_{SC} /mAcm^{-2}	V_{OC} /mV	FF /%	η /%
10	0.77	-626	73	3.5±0.2
100	5.89	-700	57	2.4±0.2

Figure 4.11: Photo I-V curve characteristic of the "best" quasi-solid-state dye-sensitized solar cells. (a) using a $TiCl_4$ post-treatment and (b) with an additional compact TiO_2 layer.

4.1.3 Spatially resolved imaging of photocurrents

In the following Section results from the spatially resolved photocurrent analysis (SMSC, Section 3.5) are presented. The aim of this analysis was to determine the influence of a different electrolyte concentration on the photocurrent distribution in the dye-sensitized solar cells. The obtained photocurrent images are presented together with I-V curves of the cells.

4.1.3.1 Influence of electrolyte concentration on the photocurrent distribution

Figure 4.12 shows the spatially resolved photocurrent image of a NSCSC, where a TiO_2 blocking layer was incorporated and a $TiCl_4$ post-treatment was performed. The electrolyte film was deposited according to Section 3.1.1.6. However, the concentration of the redox pair in the base solution was ten-fold reduced (0.5 M LiI / 5 mM I_2 in ethanol). A volume of 3 μL of the electrolyte solution was deposited on the sensitized TiO_2 layer.

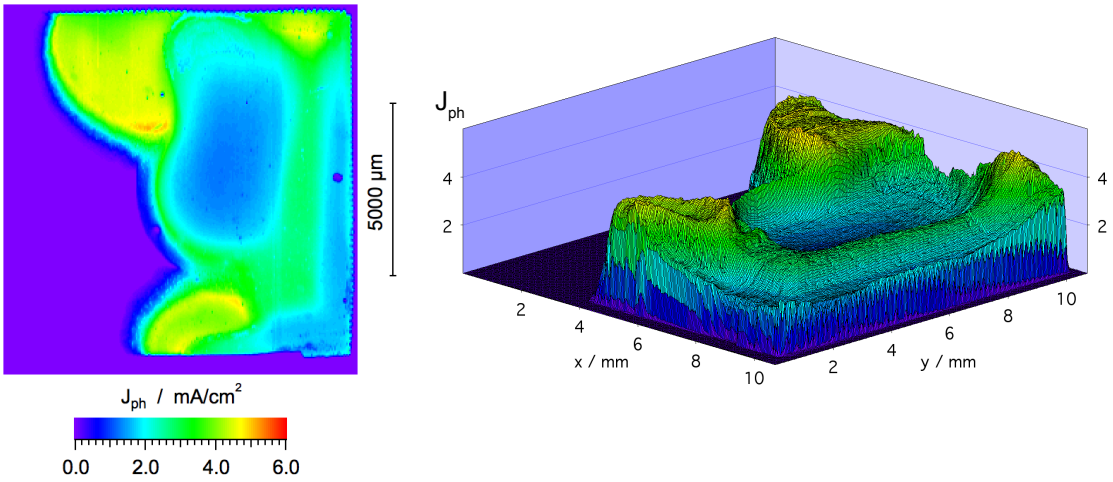

Figure 4.12: Spatially resolved photocurrent image of a NSCSC with an electrolyte film deposited from a 0.5 M LiI / 5 mM I_2 solution; step width: 40 μm; laser intensity: 130 mW/cm^2; spot diameter: 25 μm and average photocurrent density: $\overline{J_{ph}} \approx 1.8$ mA/cm^2.

For all measurements the intensity of the laser was adjusted with grey filters to ca. 0.6 μW, equivalent to a light intensity of ca. 130 mW/cm^2 with the spot

diameter of the laser $d \approx 25$ μm. The photocurrents of different laser spot positions were measured, while these positions were altered step by step with a step width of 40 μm.

The spatial distribution of the photocurrent density across the surface of the sample was quite inhomogeneous; thereby, certain areas on the surface of the cell had no photocurrents and small localized regions exhibited high photocurrents. The highest localized photocurrent was recorded at $\approx$ 5 mA/cm^2. The average photocurrent density obtained from an integration over all spots was $\overline{J_{ph}} \approx 1.8$ mA/cm^2. This value was in the range of current values obtained from I-V measurements under AM1.5G simulated conditions as presented in Figure 4.13(a).

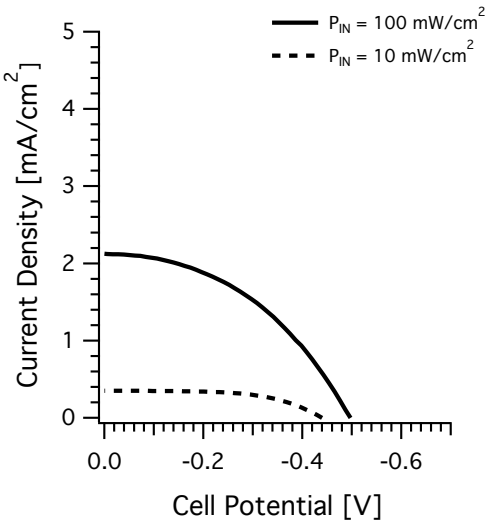

(a) ten-fold reduced LiI

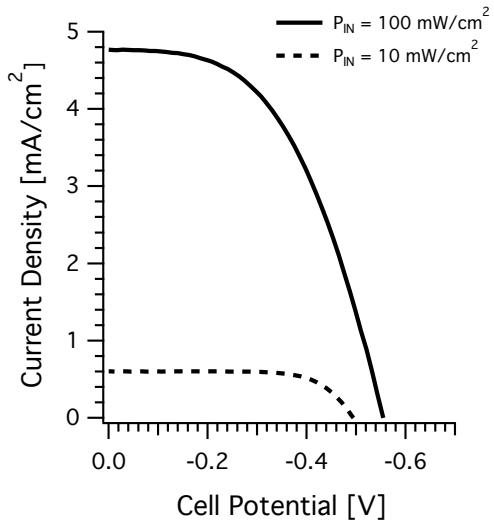

(b) five-fold reduced LiI

P_{IN} /mWcm^{-2}	I_{SC} /mAcm^{-2}	V_{OC} /mV	FF /%	η /%
10	0.35	-440	58	0.89±0.06
100	2.13	-498	43	0.46±0.03

P_{IN} /mWcm^{-2}	I_{SC} /mAcm^{-2}	V_{OC} /mV	FF /%	η /%
10	0.6	-495	70	2.1±0.1
100	4.77	-555	50	1.3±0.1

Figure 4.13: Photo I-V curve characteristic of a NSCSC with (a) ten-fold and (b) five-fold reduced redox concentration.

In view of the very localized distribution of the photocurrent, it was assumed that the amount of iodide/iodine in the base electrolyte solution, and consequently in the deposited electrolyte film was insufficient to guarantee a homogeneous coverage of the TiO_2 surface.

Figure 4.14 presents the photocurrent image of a cell with a five-fold reduced

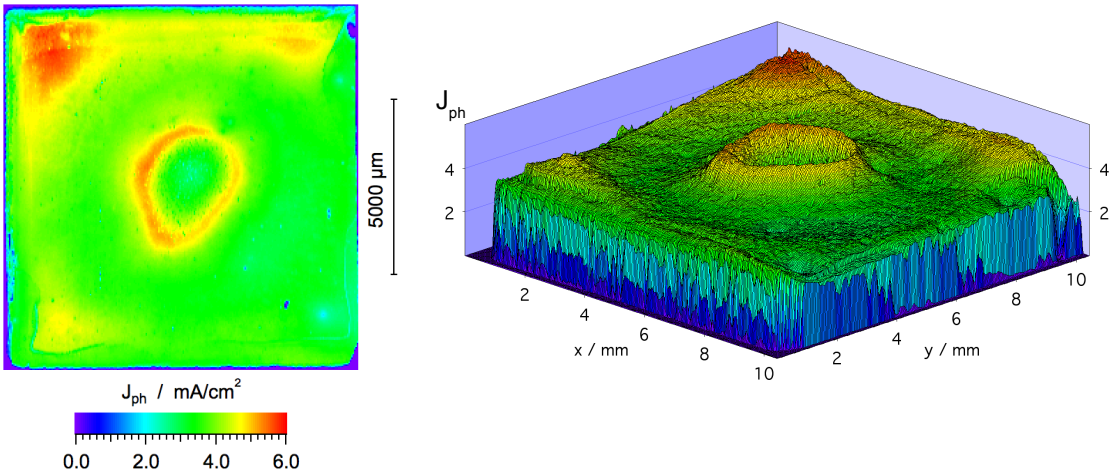

Figure 4.14: Spatially resolved photocurrent image of a NSCSC with an electrolyte film deposited from a 1 M LiI / 10 mM I_2 solution; step width: 40 μm; laser intensity: 130 mW/cm^2; spot diameter: 25 μm and average photocurrent density: $\overline{J_{ph}} \approx 3.7$ mA/cm^2.

concentration of the redox pair (1 M LiI / 10 mM I_2). The homogeneity of the photocurrent distribution increased significantly; however, there were still localized regions of higher photocurrents and "valleys" of low currents as displayed in the three-dimensional (3D) image (Figure 4.14(b)).

Effects of the electrolyte deposition were clearly noticeable in the ring-shaped area of maximum photocurrent with a decreased photocurrent in the center, which was assigned to a local variation of the concentration, originating from the spot where the electrolyte drop was placed upon deposition, followed by the spreading of the solution to the edges of the cell. The average photocurrent density was $\overline{J_{ph}} \approx 3.7$ mA/cm^2, which lay within the range of current values obtained from I-V measurements (Figure 4.13(b)).

The photocurrent distribution of a NSCSC with an electrolyte film deposited from the "standard" concentration of the redox pair (5 M LiI / 50 mM I_2) in the base solution (as used for typical cells) is presented in Figure 4.15. The maximum localized photocurrent and average photocurrent density ($\overline{J_{ph}}$) were ≈ 6.7 mA/cm^2 and ≈ 3.5 mA/cm^2, respectively. A reasonable homogeneity was observed for large parts of the cell surface; however, a slight increase was noticeable towards one side. This effect possibly originated from irregularities in the TiO_2 layer or from a slight

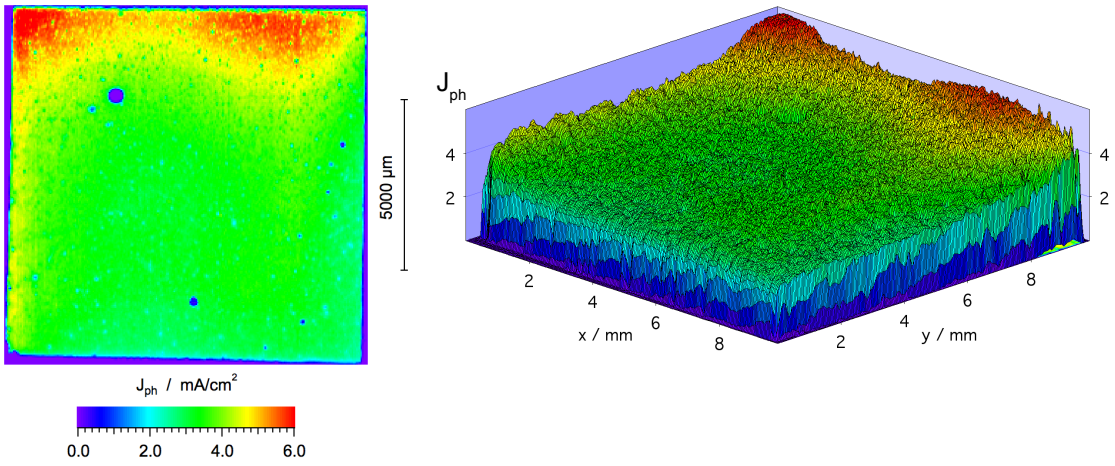

Figure 4.15: Spatially resolved photocurrent image of a NSCSC with an electrolyte film deposited from a 5 M LiI / 50 mM I_2 solution; step width: 40 μm; laser intensity: 130 mW/cm^2; spot diameter: 25 μm and average photocurrent density: $\overline{J_{ph}} \approx 3.5$ mA/cm^2.

accumulation of the electrolyte film.

As can be seen from the I-V curves presented in Figure 4.16(a), the cell had an improved fill factor and open circuit voltage values, which contributed to the overall increase in efficiency. The higher fill factor was attributed to a reduced series resistance with increased concentration of redox couple in the electrolyte film, which favored charge transport to the counter electrode.

In addition to studies on NSCSC, a spatially resolved photocurrent image was acquired of a conventional liquid DSC. Figure 4.17 shows the photocurrent distribution of a DSC containing an iodide/iodine based electrolyte with methoxypropionitrile as solvent.

The gradient in photocurrent observed in Figure 4.17 was assigned to a gradient in thickness of the TiO_2 layer. Localized areas with significantly reduced photocurrents were noticeable, which corresponded to the holes introduced during fabrication of the device for the filling of the electrolyte. In contrast to the NSCSC analyzed previously, the overall homogeneity of the photocurrent distribution was enhanced; however, the maximum localized photocurrent of ≈ 3.5 mA/cm^2 and the average photocurrent density of $\overline{J_{ph}} \approx 1.7$ mA/cm^2 were lower. It should be noted that the liquid DSC most probably suffered from degradation due to its fab-

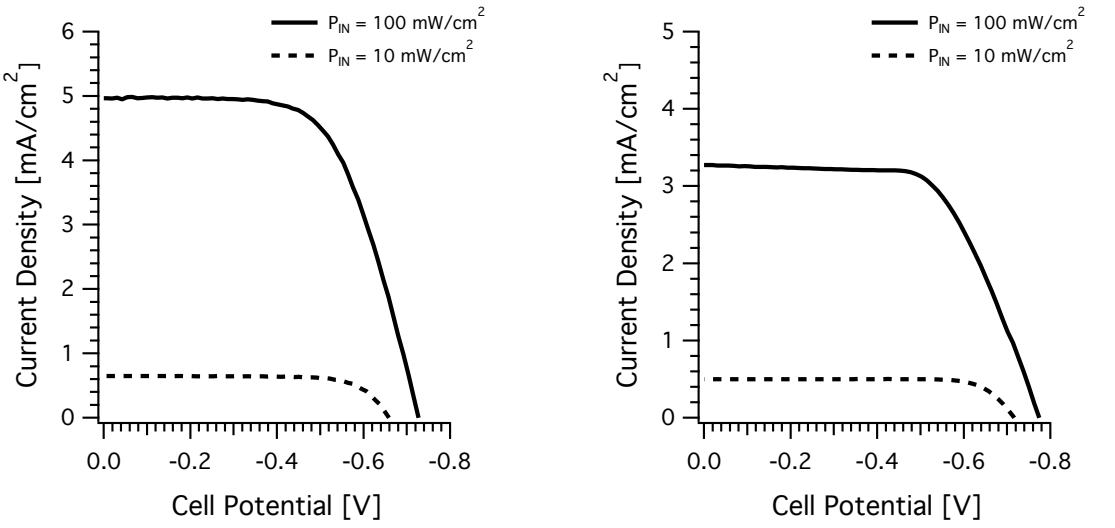

(a) standard redox concentration

P_{IN} /mWcm^{-2}	I_{SC} /mAcm^{-2}	V_{OC} /mV	FF /%	η /%
10	0.65	-658	74	3.2±0.2
100	5.02	-727	63	2.3±0.1

(b) liquid DSC

P_{IN} /mWcm^{-2}	I_{SC} /mAcm^{-2}	V_{OC} /mV	FF /%	η /%
10	0.5	-717	78	2.8±0.2
100	3.27	-774	63	1.6±0.1

Figure 4.16: Photo I-V curve characteristic of a NSCSC with (a) "standard" (5 M LiI / 50 mM I_2) redox concentration and (b) of a liquid DSC.

rication time several months prior to the reported I-V and SMSC measurements. However, the SMSC image revealed the importance of a homogeneous distributed electrolyte, which seemed to be superior in the liquid cell than in the NSCSC. The I-V curve of the liquid DSC presented in Figure 4.16(b) reveals high V_{OC} and fill factor values that partially compensate the small currents.

These results led to the conclusion, that not only was the photocurrent affected by the concentration of the redox couple in the electrolyte film but also the homogeneity of distribution in the active electrode area, where a non-uniform dispersion led to localized areas of high and low photocurrents. The areas of low photocurrents were the result of an insufficient concentration of the redox couple, which hindered the regeneration of the oxidized dye and/or the transport of the positive charge to the counter electrode. However, the use of excessive concentrations of the redox couple might lead to an increased recombination of injected electrons with the oxidized redox species (cf. Eq. 2.36). Therefore, a homogeneous distribution of the redox couple in the electrolyte film is crucial for the functioning of

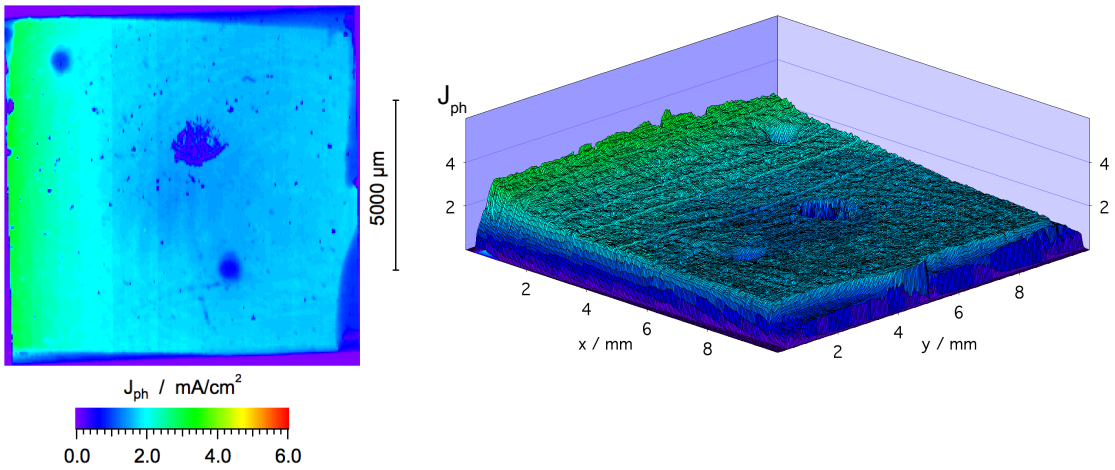

Figure 4.17: Spatially resolved photocurrent image of a liquid DSC containing an iodide/iodine based electrolyte; step width: 40 μm; laser intensity: 130 mW/cm^2; spot diameter: 25 μm and average photocurrent density: $\overline{J_{ph}} \approx 1.7$ mA/cm^2.

the solar cell.

4.1.4 Characterization by impedance spectroscopy

Impedance spectroscopy (IS) was performed to further characterize the NSCSC. IS spectra were recorded for cells containing different concentrations of the redox couple in the electrolyte film (cf. Section 4.1.3.1). The spectra were analyzed by fitting the experimental data to an equivalent circuit model that employs a transmission line of circuit elements representing the electron transport in TiO_2 (cf. Section 3.4). It must be noted that the equivalent circuit used in the presented model omits, for the sake of simplicity, elements associated with transport of charges to the counter electrode.

The characteristic parameters obtained are the electron transport resistance R_{tr}, the charge transfer resistance, R_{ct}, which is related to recombination of electrons at the TiO_2/electrolyte interface and the chemical capacity, C_μ that represents the ability of the TiO_2 layer to store electronic charge. With these parameters it was possible to calculate the basic electron transport and recombination parameters: the diffusion coefficient D_n, the electron lifetime τ_n, transit time τ_{trans} and the diffusion length L_n. IS experiments give only access to effective parameters. This implies that trapping is implicitly taken into account using the quasi-static approximation (cf. Section 2.6.2).

In order to compare cells with variations in the redox concentration, the possible differences of the conduction band position with respect to the Fermi level or redox potential has to be considered. Therefore, instead of comparing the response of the cells with respect to the potential, it is more convenient to present the data with respect to the relative position between the Fermi level and the conduction band, E_F - E_C. This provides a comparison of the kinetic parameters under conditions of an equivalent density of electrons in the different cells. The electron conductivity can be taken as a reference since it may be written as [92]:

$$\sigma_n = \sigma_0 \exp\left[\frac{E_F - E_C}{k_B T}\right] \tag{4.1}$$

where σ_0 is a constant. The conductivity of electrons in the TiO_2 may be calculated from the electron transport resistance R_{tr}:

$$\sigma_n = \frac{d_{film}}{A(1-p)R_{\mathrm{tr}}} \tag{4.2}$$

where p is the porosity of the layer (typically value: 60%), and A is the area (1 cm^2). Therefore, the samples are compared under the condition that the conduction band is filled with the same amount of electrons.

Figure 4.18 compares the diffusion coefficients obtained from IS on NSCSC with varied redox concentration in the dark and under illumination by laser light diodes at 510 nm and ca. 10 mW/cm^2. In addition, the results of impedance spectroscopy on a high efficient liquid DSC employing an acetonitrile-based electrolyte are included in the following graphs for comparison.

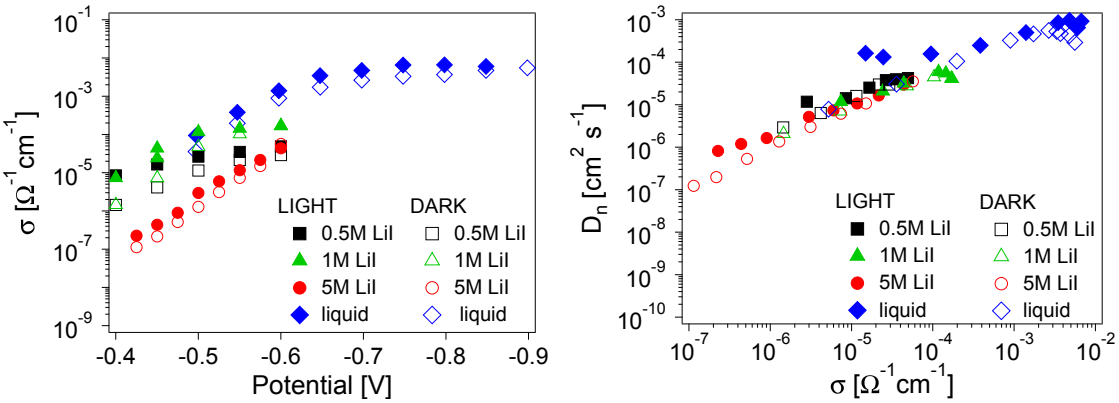

(a) (b)

Figure 4.18: (a) Conductivity σ_n as a function of the applied potential and (b) the diffusion coefficient D_n of electrons in TiO_2 as a function of σ_n for NSCSC with a different concentration of the redox couple in the electrolyte film and a liquid DSC, as indicated.

The diffusion coefficient D_n can be related to fundamental models for transport in disordered materials [178, 179]. It is obtained from C_μ and R_{tr} (cf. Eqs. 3.11 - 3.13):

$$D_n = \frac{d_{film}^2}{C_\mu R_{tr}} \tag{4.3}$$

with the time constant for the electron transit time:

$$\tau_{trans} = C_\mu R_{tr} \tag{4.4}$$

The diffusion coefficient of the three NSCSC was very similar (Figure 4.18(b)). As the concentration of electrons and thus the conductivity increased, the charge

transport resistance R_{tr} decreased. This indicates an increase in the diffusion coefficient D_n. However, the concentration of the redox couple did not have a significant influence on D_n.

Figure 4.19 presents the electron lifetime τ_{n} and the transit time τ_{trans} obtained from IS under illumination. The effective electron lifetime τ_n was obtained from the impedance data according to:

$$\tau_n = C_\mu R_{ct} \tag{4.5}$$

where R_{ct} is the charge transfer resistance associated with the recombination of electrons. Both τ_{n} and τ_{trans} decreased as the conductivity increased.

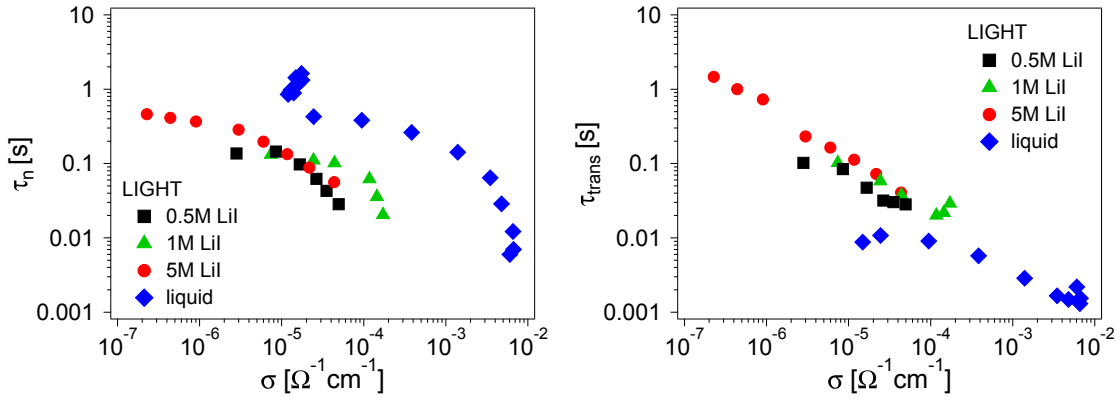

Figure 4.19: Effective electron lifetime τ_n and transit time τ_{trans} of electrons in TiO_2 for NSCSC with a different concentration of the redox couple in the electrolyte film and a liquid DSC, as indicated. The data is plotted versus the electron conductivity in the TiO_2.

The charge transfer (or recombination) resistance R_{ct} decreased with higher conductivity due to the increasing electron density that augmented the recombination rate (Figure 4.20(b)). Accordingly, the effective lifetime of electrons in the TiO_2, τ_n, decreased (Figure 4.19(a)). The obtained electron lifetime at the same conductivity was about a factor ten higher in the liquid DSC than in NSCSC, as it could be concluded from the fact that R_{ct} was about two orders of magnitude higher in the liquid cell. Moreover, the transit time in liquid DSC was much smaller than in NSCSC, which corresponded to the higher diffusion coefficient (Figure

4.18(b)). This effect was possibly due to the higher electron concentration (higher conductivity) in the liquid DSC (Figure 4.18(a)).

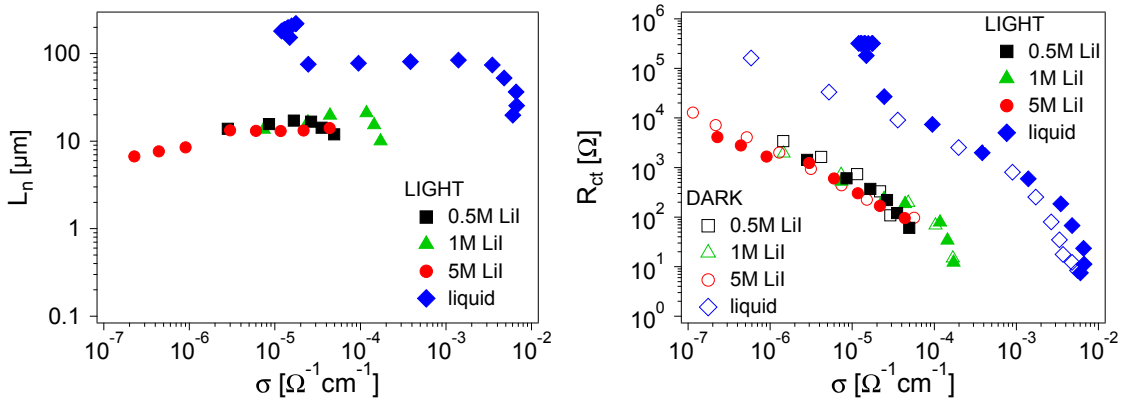

Figure 4.20: Diffusion length and charge transfer resistance R_{ct} of electrons in TiO_2 for NSCSC with a different concentration of the redox couple in the electrolyte film and a liquid DSC, as indicated. The data is plotted versus the electron conductivity in the TiO_2.

Figure 4.20 presents the diffusion length together with the charge transfer resistance R_{ct} in the TiO_2 as a function of the potential obtained from IS under illumination. The diffusion length is a measure of how far an electron diffuses toward the anode before it is lost through recombination. Thus, the diffusion length has to be larger than the film thickness. A diffusion length of electrons larger than the thickness of the film means that the transit time, i.e. the time required for an electron to reach the contact, is shorter than the lifetime (cf. Figure 4.19), and this is a necessary condition to efficiently collect the charge injected by the dye under illumination. The values obtained in this measurements were sufficiently large at higher electron densities to guarantee that electrons could be collected. However, diffusion lengths obtained for the liquid DSC were significantly higher than in NSCSC (Figure 4.20(a)). This effect correlated with an increased recombination resistance at same electron densities in the conduction band for the liquid DSC (Figure 4.20(b)).

The dependence of the charge transfer resistance R_{ct}, the transport resistance R_{tr}, and the chemical capacitance C_μ as a function of the cell potential is illustrated in Figure 4.21 for the liquid DSC. Important for the functioning of the cell was a

higher recombination resistance than transport resistance, which was given here. Both resistances decreased with the applied negative potential as the electron density increased, which favored both recombination and charge transport. The chemical capacitance C_μ is proportional to the density of electron trap states below the conduction band edge. This density increases towards the conduction band (e.g. by an exponential function, cf. Eqs. 3.13 and 2.17) [171]. It was then clear that C_μ increased as the Fermi level approached the conduction band due to the applied potential.

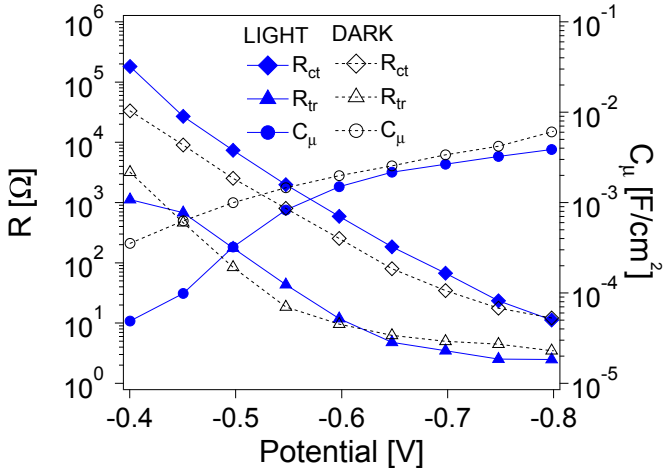

Figure 4.21: Charge transfer resistance R_{ct}, the transport resistance R_{tr}, and the chemical capacitance C_μ as a function of the cell potential in a liquid DSC.

In summary, electron transport appeared to be unaffected by the concentration of the redox couple in the electrolyte film of NSCSC. Since impedance measurements reflect the (quasi) stationary state of the system, a stationary high concentration of triiodide was assumed to be present around the TiO_2 particles, which did not increase with higher concentrations of the redox couple. Therefore, the transport of the positive charge to the counter electrode seemed to be the main process limiting the efficiency of the NSCSC.

4.1.5 Characterization by scanning electron microscopy

The microscopic morphology of the mesoporous TiO_2 layer and of other modifications performed on the NSCSC were characterized by Scanning Electron Microscopy (SEM). Figure 4.22 presents a cross section SEM image of a TiO_2 layer

on FTO glass. The mesoporous layer with a thickness of about 12 μm consisted of a mixture of ca. 20 nm sized particles and bigger, ca. 200 nm sized particles that acted predominantly as scatterers for light, as depicted in a higher resolution image in Figure 4.22(b).

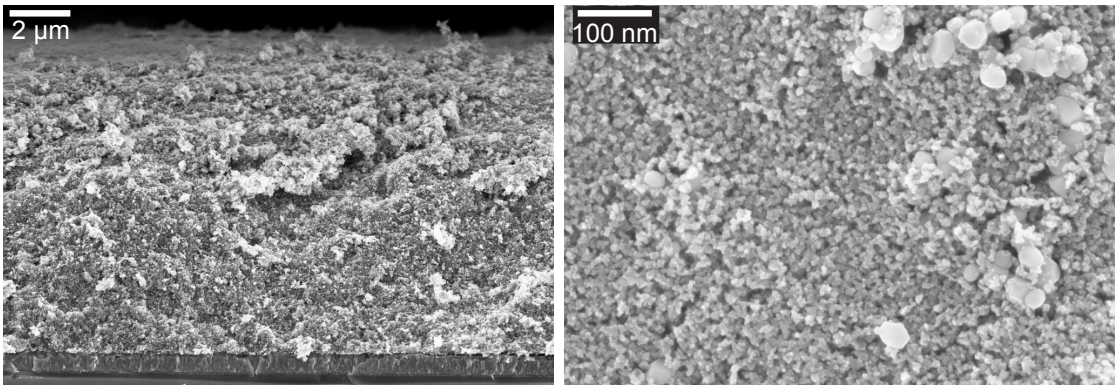

(a) (b)

Figure 4.22: SEM cross section image of a screen-printed, mesoporous TiO_2 layer on FTO glass.

A compact TiO_2 underlayer of about 100 nm thickness was deposited between the TiO_2 layer and the ca. 400 nm thick FTO layer (Figure 4.23). The compact TiO_2 layer provided a barrier for the recombination reaction of injected electrons from the FTO with oxidized redox species (Eq. 2.37).

4.2 Subset devices based on TiO_2: Time Resolved Microwave Conductivity (TRMC) studies

The results of the previous Section (Section 4.1) showed that the quasi-solid-state DSC in this work functioned as a standard DSC although with lower efficiency. However, the absence of liquid in this cell enabled an improved investigation of the (opto) electronic properties of DSC. To improve the sensitivity, the samples analyzed were deposited on a quartz substrate with a similar configuration to the device described here, in order to assure the value of this analysis for the functioning of DSC.

In this Section, the TRMC signals of different subsets of the device presented

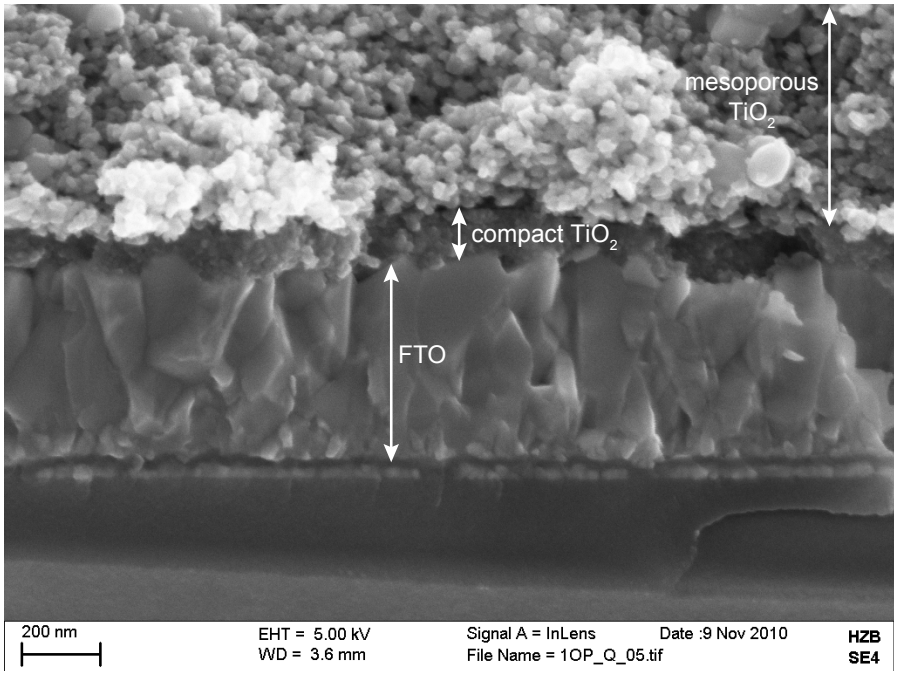

Figure 4.23: SEM cross section of the compact TiO_2 layer between the FTO glass and the mesoporous TiO_2.

in the Section 4.1 will be compared in order to investigate the influence of the different components on the electron transport.

4.2.1 Influence of the electrolyte components

In Figure 4.24 the TRMC signals of a sensitized TiO_2 film on quartz glass are compared to that of a sensitized film with an electrolyte as used in the device.

The deposition of the electrolyte film with a high iodide/iodine concentration led to a much slower decay when compared to the untreated sample. The decay of the signals could not be described by only one exponential function with a single time constant. Therefore, the signals were separated into time regimes characterized by their respective, exponential decay constants. The signals showed a fast initial decay with time constants (determined by an exponential fit in the time regime up to 60 ns) $\tau_1 = (160 \pm 3)$ ns for the "bare" TiO_2/N719 sample and $\tau_2 = (390 \pm 10)$ ns for the TiO_2/N719/electrolyte sample. In the time regime from 10 to 75 μs the signal of both the untreated TiO_2/N719 and TiO_2/N719/electrolyte sample decayed rather slowly with $\tau_3 = (110 \pm 11)$ μs and $\tau_4 = (600 \pm 28)$ μs,

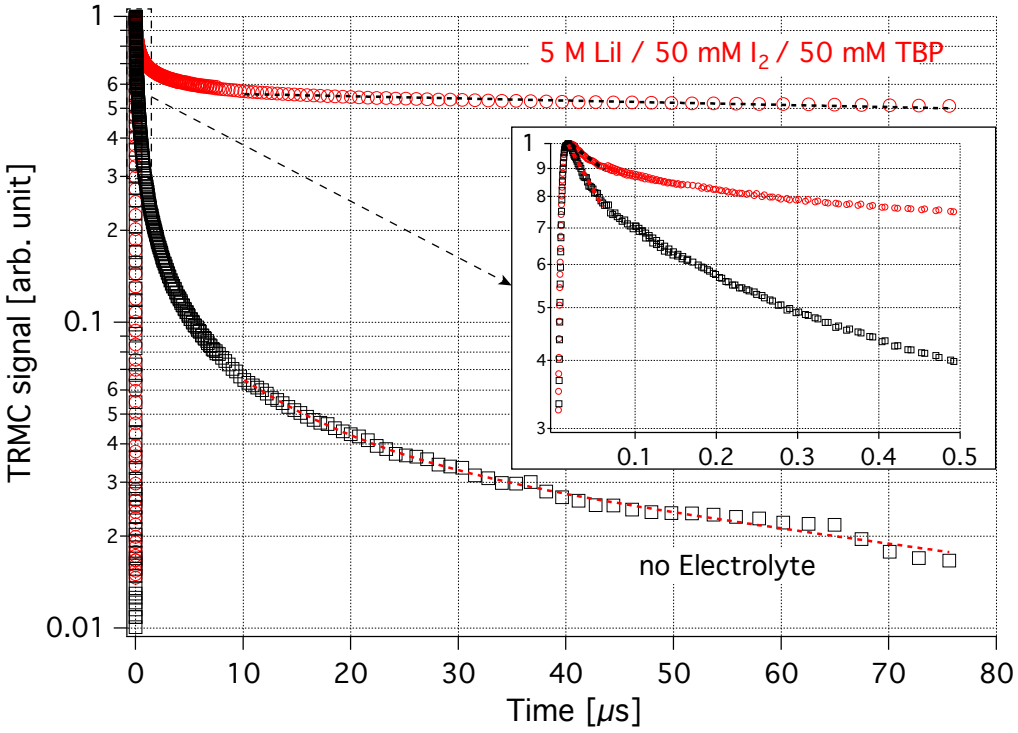

Figure 4.24: Normalized TRMC signals of sensitized TiO_2 films on quartz glass with/without redox pair induced by laser pulses at 532 nm. The insert shows the signals on a shorter time scale. Laser intensity: 1.3 mJ/cm^2.

respectively. The fast initial decay suggests a fast recombination of photogenerated charge carriers, especially in view of the high excitation densities. Most likely, electrons injected from the dye into TiO_2 recombine with the oxidized dye. In the presence of the redox pair the oxidized dye can be reduced by iodide; thus, quenching this decay channel. In addition, the dye adsorbed at the surface could also passivate surface states responsible for the dispersive transport.

To further evaluate the decay behavior in the presence of the redox pair, the concentration of the electrolyte constituents was varied (Figure 4.25). The decay of the TRMC signal revealed a dependence on the electrolyte concentration with the fastest decay for the lowest concentration of iodide/iodine. The decay time in the range up to 60 ns decreased with decreasing electrolyte concentration. For a ten-fold reduced concentration of the electrolyte solution, the lifetime was nearly halved. However, for the lifetime in the time region from 10 to 75 μs there was

only a minor diminution for the lowest concentration. In addition, the halved and five-fold reduced concentrations appeared to induce a saturated condition, as there was no noticeable difference in the decay behavior.

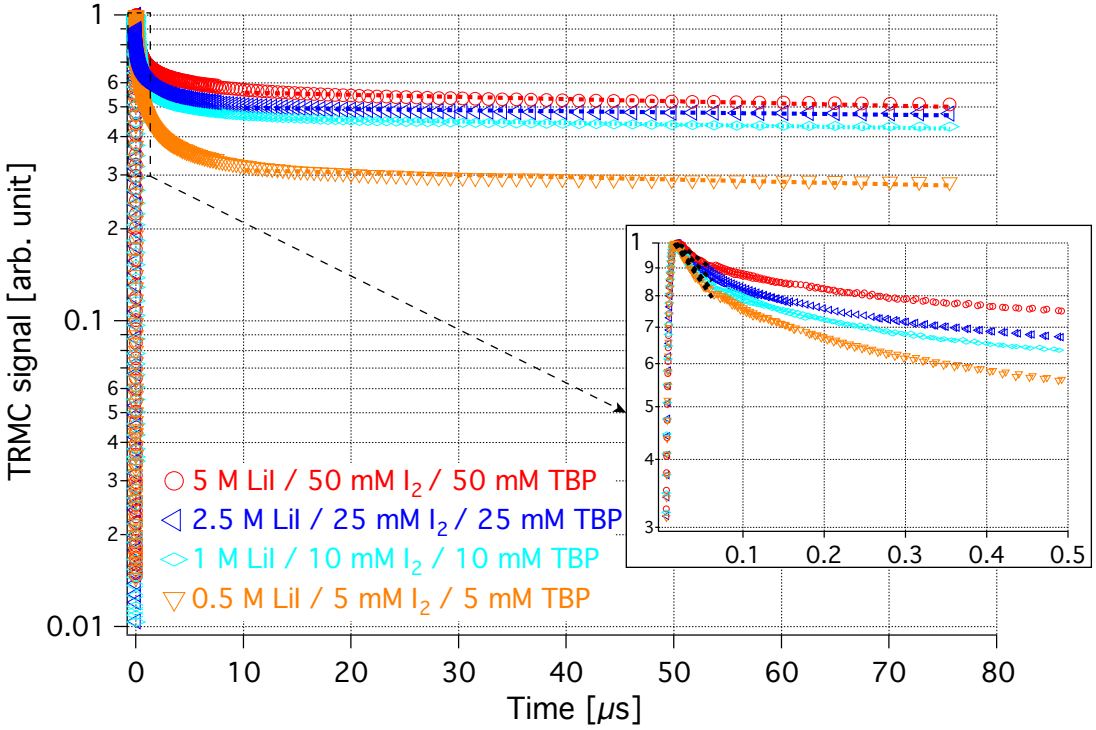

Figure 4.25: Normalized TRMC signals of sensitized TiO_2 films with different electrolyte concentrations induced by laser pulses at 532 nm. The insert shows the signals in the first 500 ns and the exponential fits for the fast initial decay in the time regime up to 60 ns. Laser intensity: 1.3 mJ/cm^2.

Since the electrolyte consisted of the redox pair, 4-tert-butylpyridine (TBP) as an additive, and ethanol as a solvent, a possible influence of these components on the charge carrier decay was analyzed. The addition of ethanol to the sensitized TiO_2 layer caused an increase of charge carrier lifetime (Figure 4.26). Previously, it was reported that adsorption of 2-propanol on TiO_2 powder led to a decrease of the electron decay rate after band-to-band excitation and was attributed to a decrease of the electron recombination rate by the trapping of excess holes in surface states induced by 2-propanol with a low recombination probability [162]. Similar conclusions were drawn here, where ethanol acted as a hole scavenger in

TiO_2 films [180, 181]. In general, the decrease of the decay rate under influence of ethanol (Figure 4.26) was explained by a decrease of the recombination rate as described above, a decrease of the electron trapping rate by suppression of active electron traps, or both.

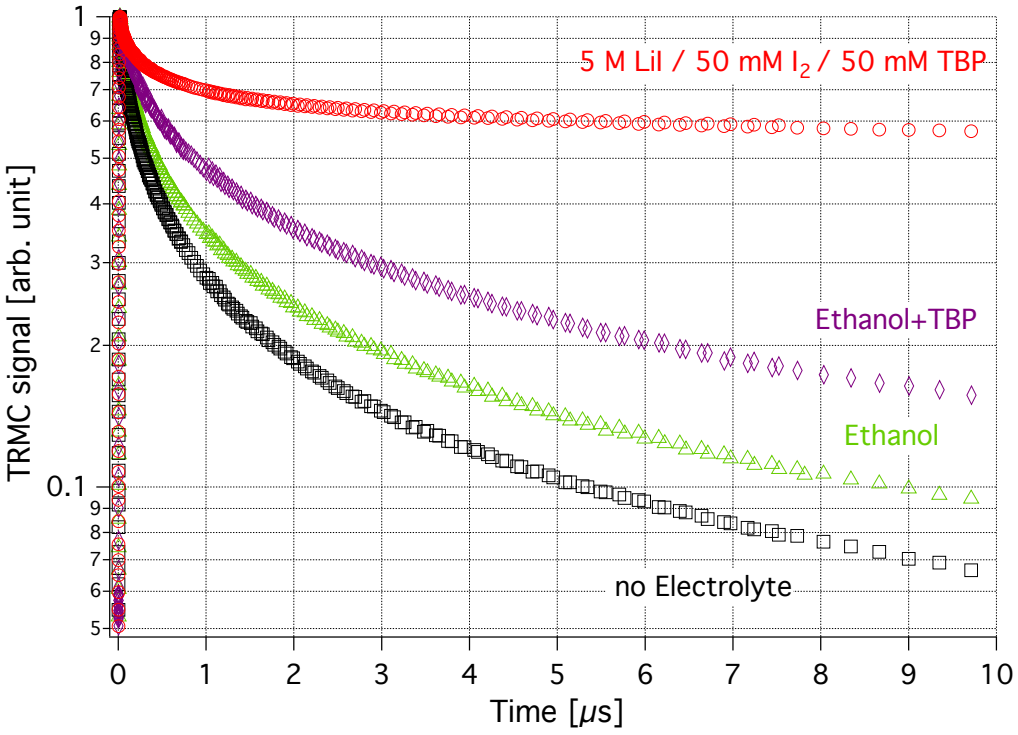

Figure 4.26: Influence of electrolyte constituents ethanol and 4-tert-butylpyridine (TBP) on the TRMC signals of sensitized TiO_2 films induced by laser pulses at 532 nm. Laser intensity: 1.3 mJ/cm^2.

The addition of TBP led to a further prolonged decay. One effect of TBP in the redox electrolyte of dye-sensitized TiO_2 solar cells was observed to change the surface charge of TiO_2 by decreasing the amount of adsorbed protons, lithium ions, or both [182]. In the case of ethanol/TBP, the slow decay may be attributed to a screening of positive charges on the TiO_2 surface; therefore, hindering the recombination of electrons.

The adsorption of cations like Li^+ on the TiO_2 surface was proposed to accelerate the regeneration of oxidized dye by reversing the particle surface charge from negative to positive, which causes I^- to adsorb electrostatically onto the nanoparti-

cles [133]. The formation of (I^-, I^-) ion pairs on the surface of TiO_2 was suggested to allow the more energetically favorable and faster regeneration reaction involving oxidation of I^- to $I_2^{-\bullet}$ to take place [133, 134]. To distinguish the influence of adsorbed Li from the effect of the redox couple on the signal decay, TiO_2 films were treated with electrolyte solutions containing high amounts of lithium perchlorate (Figure 4.27).

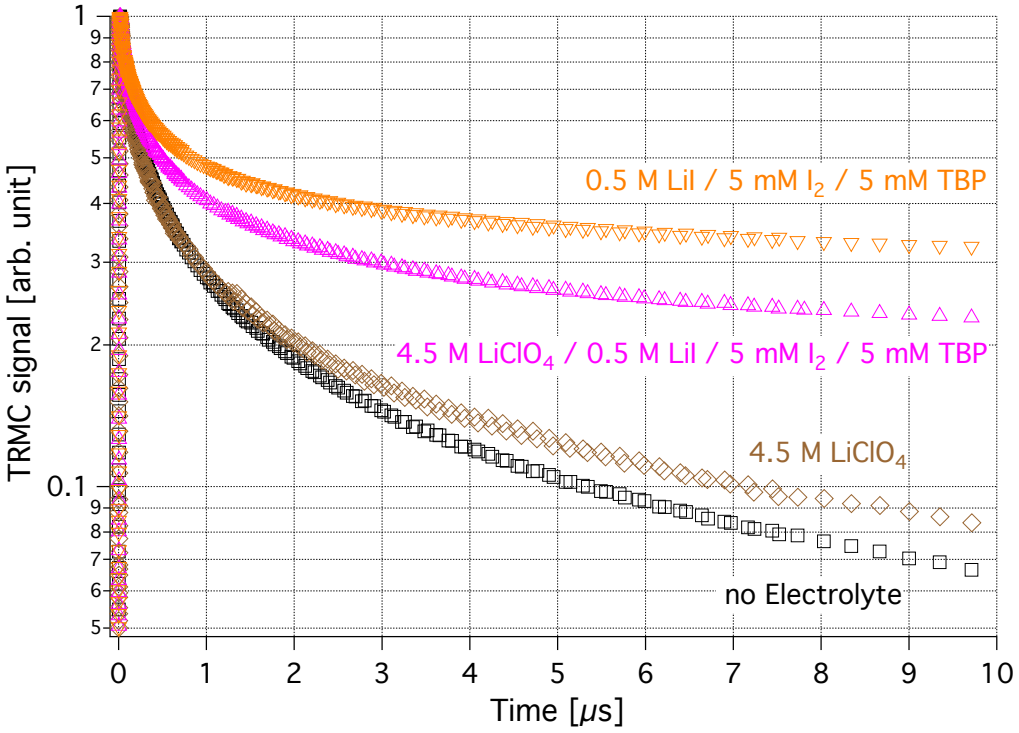

Figure 4.27: Influence of cation concentration on the TRMC signals of sensitized TiO_2 films induced by laser pulses at 532 nm. Laser intensity: 1.3 mJ/cm^2.

The decay of the sample treated with $LiClO_4$ in ethanol showed only a slightly slower decay; comparable to the effect of ethanol on the sensitized TiO_2 films (Figure 4.26). The samples corresponding to the two upper curves in Figure 4.27 were treated with the same concentration of LiI/I_2, but only one sample received an additional treatment with $LiClO_4$. The sample treated with the high $LiClO_4$ concentration in addition to the standard LiI/I_2 composition showed a slightly accelerated decay. The presence of the $LiClO_4$ might induce a competition for adsorption sites of the two species, thereby partially hindering the regeneration of

oxidized dye by I^-. As there was no significantly prolonged decay for the sample treated only with $LiClO_4$, it can be concluded that the slower decay was due to the presence of the iodide/iodine redox pair in the electrolyte solution.

4.2.2 Exchange of the redox couple: the importance of iodide/iodine

For a further understanding of the role of the iodide/iodine redox pair on the slow decay of charge carrier observed by the TRMC studies, an alternative redox couple was used. Presently, only the iodide/iodine redox pair allows conventional dye-sensitized solar cells to function efficiently. In order to guarantee an efficient electron transfer to the external circuit the rate of reduction of the dye cation by a redox couple (Reaction 2.47) should be higher than the rate of recombination of the dye cation with electrons injected into the TiO_2 (Reaction 2.35). Moreover, the charge recombination should be slow to avoid recombination between electrons in the TiO_2 film and the oxidized part of the redox couple (Reaction 2.36) [113]. The self-exchange rate for the iodide/iodine redox pair is very slow ($k_{ex} \approx 5 \times 10^2\ M^{-1}s^{-1}$) [183] compared to the kinetically fast redox couple ferrocene/ferrocenium (Fc/Fc^+, $k_{ex} \approx 10^7\ M^{-1}s^{-1}$) [184, 185]. However, the redox potential of the ferrocene couple (0.31 V vs SCE) is comparable to that of the I^-/I_2^- couple (0.15 V vs SCE). Thus, the major difference between the ferrocene and iodine couples lies in the different rates for electron transfer; the rate for electron injection from the excited dye to TiO_2 being almost equal to that of the transfer rate of injected electrons from TiO_2 to ferrocenium. Therefore, injected electrons recombine very fast with the oxidized redox species and no photocurrent can be detected in a DSC employing the Fc/Fc^+ couple. The ferrocene/ferrocenium couple was used previously to probe the inhibition of recombination reactions by surface treatment in conventional DSC [113]. In the present work, it was used to further analyze the influence of the redox couple on the charge carrier kinetics by the TRMC method.

Figure 4.28 compares the TRMC signal of a sensitized TiO_2 layer on quartz glass to samples treated with the standard electrolyte film as used in the device and a sample where an electrolyte film containing the Fc/Fc^+ couple was deposited.

In contrast to the films treated with the iodide/iodine pair where an increase

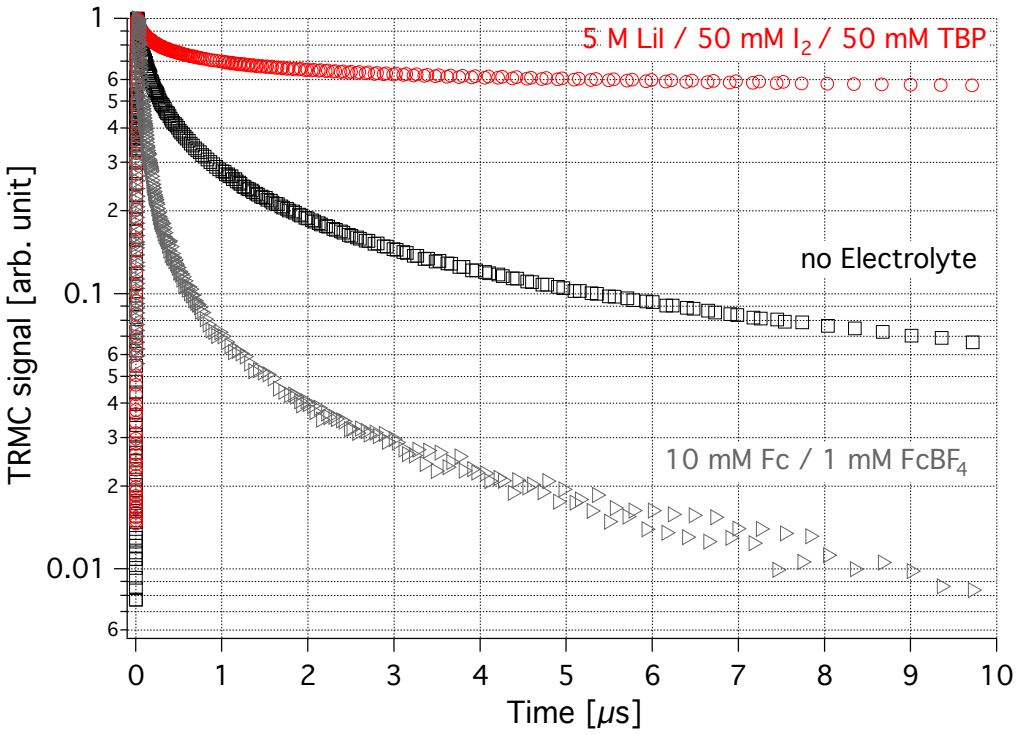

Figure 4.28: Normalized TRMC signals induced by laser pulses at 532 nm of sensitized TiO_2 films on quartz glass with/without redox pair and the Fc/Fc^+ redox pair. Laser intensity: 1.3 mJ/cm^2.

of the electron lifetime was observed (4.2.1), the presence of the kinetically fast ferrocene/ferrocenium system led to a dramatic increase of the decay rate. This behavior could be explained by an increased availability of recombination sites introduced by ferrocene/ferrocenium. Photoinjected electrons $e^-_{TiO_2}$ could recombine fast with the oxidized form R^+ of the redox couple. In the case of iodide/iodine, the reduction of the dye cation D^+ decreased the recombination probability with injected electrons from the TiO_2. Due to the kinetically slow reduction rates of the oxidized redox couple I^-/I_2^-, the electron lifetime increased. On the other hand, in the ferrocene/ferrocenium system the predominant decay channel could be ascribed to the fast recombination of injected electrons with ferrocenium. This provided an additional microscopic background for the higher performance of DSC employing the iodide/iodine system.

4.2.3 Summarizing discussion

The TRMC signals presented in the previous Section were not mono-exponential and were characterized by a decay rate constantly decreasing with time (Figures 4.24 - 4.28). This effect was expected due to the heterogeneity of the samples: a distribution of electron traps and recombination centers will show this behavior if also emission from these states play a role. Previous studies employing transient absorbance (TA) techniques revealed an increase in the rate of dye cation decay with increasing iodide concentration [136,138]. The observed decay was separated into two components: (1) a fast decay channel involving quenching of the cation signal and assigned to the reduction of the oxidized dye by iodide leading to the formation of $I_2^{-\bullet}$ species, and (2) a slower channel assigned to long-lived $I_2^{-\bullet}$ and $e^-_{TiO_2}$, with the decay of this signal being assigned to the $I_2^{-\bullet}$ disproportionation reaction (Equation 2.48) and interfacial charge recombination of $e^-_{TiO_2}$ with the redox couple.

In agreement with these findings, the observed slower decay of the TRMC signal for high concentrations of the redox pair (depending on the concentration of the redox pair) was attributed to the regeneration of the oxidized dye by iodide; therefore, screening the positive charge from possible recombination with injected electrons $e^-_{TiO_2}$. The recombination of electrons with I_3^- was not found to be rate limiting the fast decay behavior. Furthermore, the main decay channel for the sensitized TiO_2 films in absence of any redox species was ascribed to the recombination of injected electrons with the oxidized dye D^+. Also experiments can be cited on non-sensitized TiO_2 reporting a decrease of the electron lifetime by adding a redox couple [186]. This provided additional support for the explanation given above: the increase of the electron lifetime observed here was intimately connected to the presence of the positive counter charge in the form of the dye cation. The interaction of this dye cation with the redox couple decreased the recombination probability of the electrons.

4.3 Transport and kinetics in TiO_2 and ZnO colloidal systems

In order to obtain a more thorough understanding of charge carrier transport in DSC and nanosystems in general, the analysis of subset devices of TiO_2-based quasi-solid-state dye-sensitized solar cells by TRMC measurements (cf. Section 3.2) was further extended to TiO_2 and ZnO colloidal systems (powders, films and nanorods).

The experimental data were analyzed by studying the influence of variation of the excitation wavelength and intensity on the TRMC signal. It is convenient to distinguish two time regimes of the signals: the time regime during the excitation and the adjacent one, which presents the decay of generated charge carriers. Moreover, recombination and trapping processes during the excitation pulse are expressed in the maximum TRMC signal height.

Several authors reported an intensity dependence of the microwave signal in TiO_2 layers at low excitation densities, which was attributed to a gradual filling of trapping sites with increased light intensity [187,188]. In these studies, a superlinear increase in the initial microwave signal with increasing light intensity was observed. At a certain intensity the dependence became linear and eventually approached sublinearity for higher values of the excitation; thus, two decay processes are active during the excitation and influence the amplitude: interaction between electrons and a large distribution of traps, and electron hole recombination. The former leads to a linear dependence of the amplitude on the excitation density in the range where the density of electrons is much smaller than the density of traps; merging to a superlinear dependence in the range where the density of electrons approaches the density of traps. The latter is active at higher excitation densities; hence, leading to a sublinear dependence of the amplitude.

The dependence of particle size in TiO_2 studied by Katoh et al. demonstrated no major trap filling effect for 300 nm particle size films, which was assigned to a lower density of traps in these bigger particles [188].

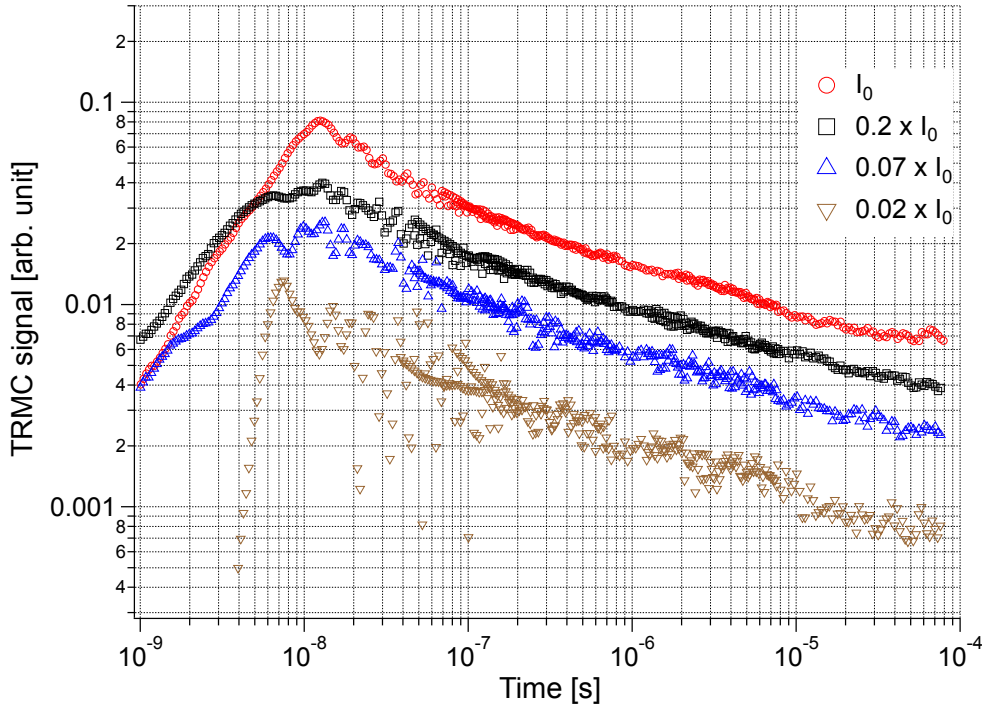

Figure 4.29: TRMC signals of TiO_2 powder (P25) in a double-logarithmic representation induced by laser pulses at 355 nm and different laser intensities (I_0 = 25 mJ/cm^2).

4.3.1 Bare TiO_2 powders and films

The TRMC signal of TiO_2 powder (P25) induced by light pulses at 355 nm was characterized by an extended decay, i.e., the decay rate decreased with time (Figure 4.29). In the time regime from 100 ns to 100 μs, the decay was described approximately by a power law with a coefficient of -0.25, where the initial decay up to about 100 ns was faster than according to this power law. A power law is defined as $\Delta S(t) = Bt^{\gamma}$, where ΔS represents the TRMC signal being proportional to the change in photoconductance (Section 3.2), B is a constant, and γ characterizes the decay.

In this TRMC signal the decay behavior was within the experimental accuracy independent of the excitation density (Figure 4.29). However, the maximum signal at about 10 ns (the TRMC amplitude, A_{10ns}) was not linear with the excitation density but proportional to its square root. This effect could be due to a decrease in

electron mobility with increasing charge carrier concentration, or to a fast electron-hole recombination during excitation [187]. The latter may be preferred [188].

The extended decay in TiO_2 powder (Figure 4.29) was expected since there was a large distribution of states interacting with the generated excess charge carriers. In general, the observed electron decay is due to (i) the interaction (i.e. trapping and emission) of electrons with a wide distribution of states in the band gap (multiple trapping) and to (ii) recombination of electrons with holes characterized by a large distribution of cross sections. A simple example of the first process is multiple trapping in an exponential band tail with constant cross section as used for charge carrier transport in amorphous silicon (a-Si:H) [189]. As for the second process, an example is the recombination of electrons with holes in the valence band, where the availability of holes is determined by hole emission from a wide distribution of states [190]. However, it is speculative to attribute the observation of an extended decay characterized by a power law over a restricted time range to the interaction of charge carriers with an exponential band tail [190]. The display of the experimental data in a double-logarithmic representation enables an overview over the whole decay but it conceals important details, in particular in the short time range.

In the case of TiO_2 films prepared by a screen-printing method, the TRMC signal generated by light pulses at 355 nm presented an extended decay (characterized by a power law after 100 ns) and a TRMC amplitude proportional to the square root of the excitation density. These results were similar to TiO_2 powder. On the other hand, the TRMC amplitude, A_{10ns}, in the films was significantly larger than in the powder (about a factor 2 - 3 at the same excitation density) (Figure 4.30). Furthermore, the final decay in the film at the highest excitation density was slower than at lower excitation densities.

The power law coefficient of the decay after 100 ns in the film was about -0.40, where in TiO_2 powder this value was only -0.25. Therefore, the decay in TiO_2 films was clearly faster than in TiO_2 powder. Also the initial decay up to 100 ns was faster in the film than in the powder.

The larger TRMC amplitude found in TiO_2 films could be due to a higher effective mobility or more likely a better light coupling because of a higher TiO_2 density.

Figure 4.31 shows the TRMC signals of TiO_2 film (upper curves) and TiO_2

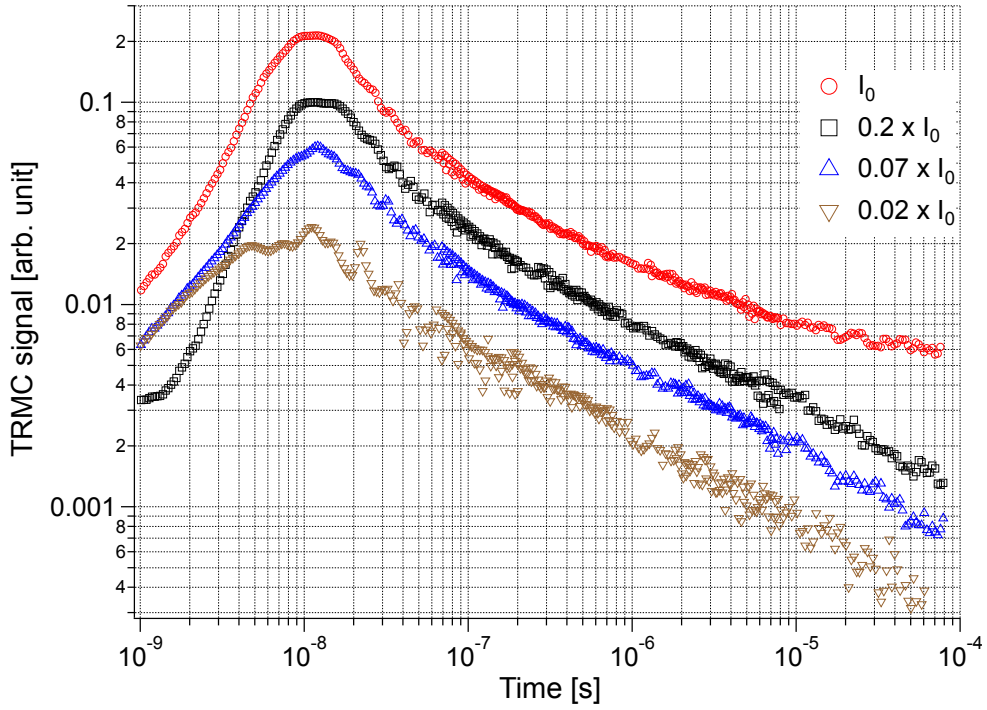

Figure 4.30: TRMC signals of TiO_2 films in a double-logarithmic representation induced by laser pulses at 355 nm and different laser intensities (I_0 = 25 mJ/cm^2).

powder (lower curves) at different laser intensities. The TRMC signals at two different excitation densities were normalized to the same amplitude in order to improve the visualization of the decay behavior. In addition, the TRMC signals of TiO_2 film were arbitrarily displaced relative to the signals of the powder. TRMC signals of TiO_2 film exhibited a clearly visible slower decay at the highest excitation density after 10 μs. In the case of TiO_2 powder, a slower decay was also detected, where also the initial decay up to 100 ns (not conform to a power law) was faster in the TRMC signals of the film. It is important to note that the final decay in the TiO_2 film at the highest excitation density (from about 10 μs) was parallel to the powder samples. This effect suggests the presence of an additional decay process in films compared with powders that could be saturated at high excitation densities.

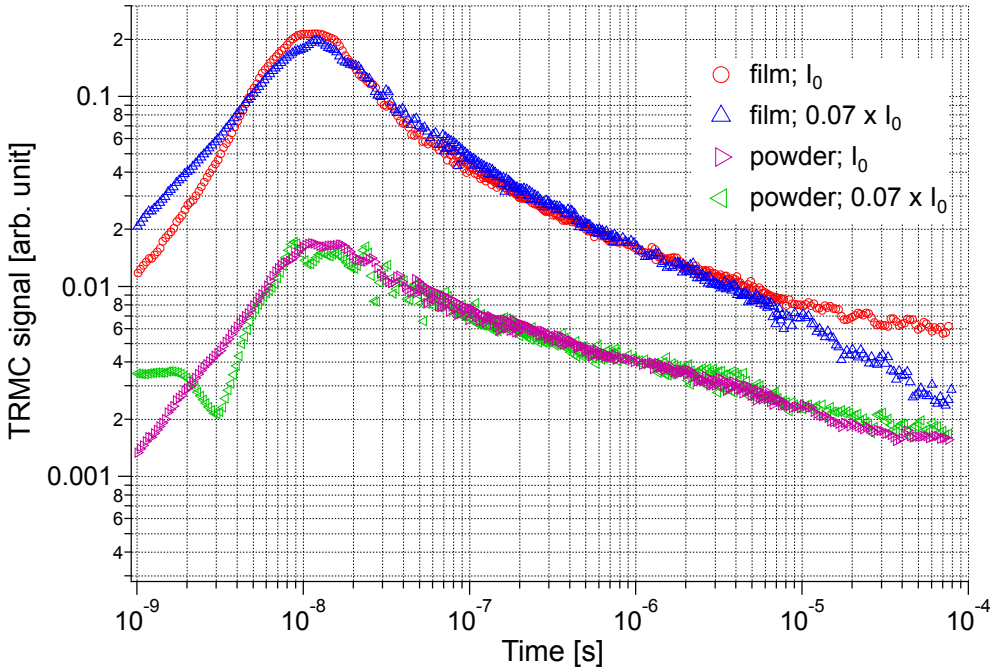

Figure 4.31: TRMC signals of TiO_2 powder and films in a double-logarithmic representation induced by laser pulses at 355 nm and different laser intensities ($I_0 = 25$ mJ/cm^2). Signals obtained in the same sample were normalized to the same amplitude.

4.3.2 Sensitized TiO_2 powders and films

Dye sensitization of TiO_2 is normally used to increase charge carrier generation in the visible range. However, this investigation showed that charge carrier kinetics are also strongly influenced by the adsorption of dye molecules at the surface.

Figure 4.32 shows TRMC signals of bare and sensitized TiO_2 powder generated by light pulses at 355 nm and two excitation densities. First, the signal amplitude did not change appreciably by the presence of dye molecules at the surface. This suggests that the generation of excess charge carriers proceeds mainly by direct excitation of electrons and holes in TiO_2 and the excitation of the dye plays only a minor role. Furthermore, the decay rate of the sensitized TiO_2 powder was distinctively slower than in the non-sensitized TiO_2 powder. However, this difference in decay rate occurred only in the first 100 ns as it can be seen in a semi-logarithmic representation (Insert Figure 4.32). The decay after 1 μs was

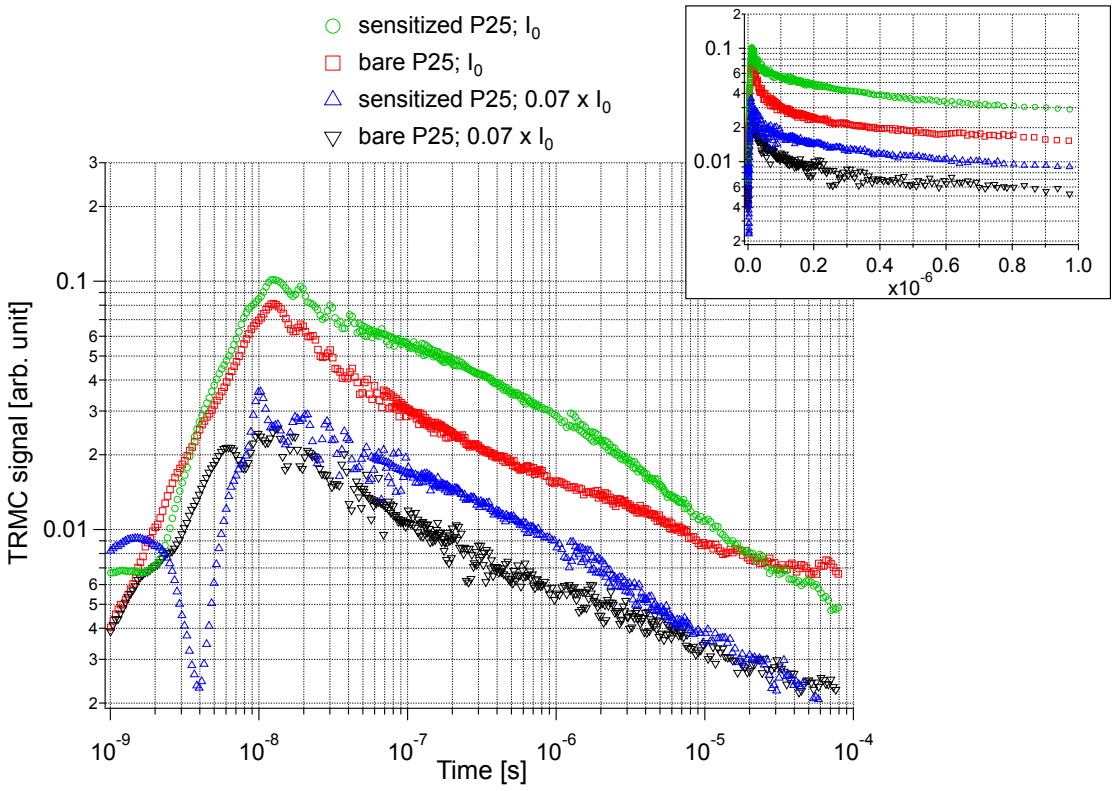

Figure 4.32: TRMC signals of bare and sensitized TiO_2 powder (P25) in a double-logarithmic representation induced by laser pulses at 355 nm and different laser intensities (I_0 = 25 mJ/cm^2). Sensitization with N719 Ru-dye. The insert shows the TRMC signals in a semi-logarithmic representation in the short time range (0 - 1 μs).

even faster in the sensitized TiO_2 powder leading to a crossing of the signals for sensitized and non-sensitized samples after 10 μs (Figure 4.32). Additional data at still lower excitation densities suggests that the signals in sensitized TiO_2 powder approached the data in non-sensitized TiO_2 powder (not shown here).

In the case of dye-sensitized and non-sensitized TiO_2 films, the same phenomena were observed when comparing the signals after 355 nm excitation (Figure 4.33), where the TRMC signal of the sensitized TiO_2 film exhibited no major changes in the signal amplitude and the decay was slower in the sensitized TiO_2 film during the first 100 ns after the start of the excitation (Insert in Figure 4.33).

However, differences were detected in the decay in the short time range (up to 1 μs) between dye-sensitized TiO_2 powders and films (Figure 4.34).

After 1 μs, the decay was identical and characterized by a power law between 1 μs -

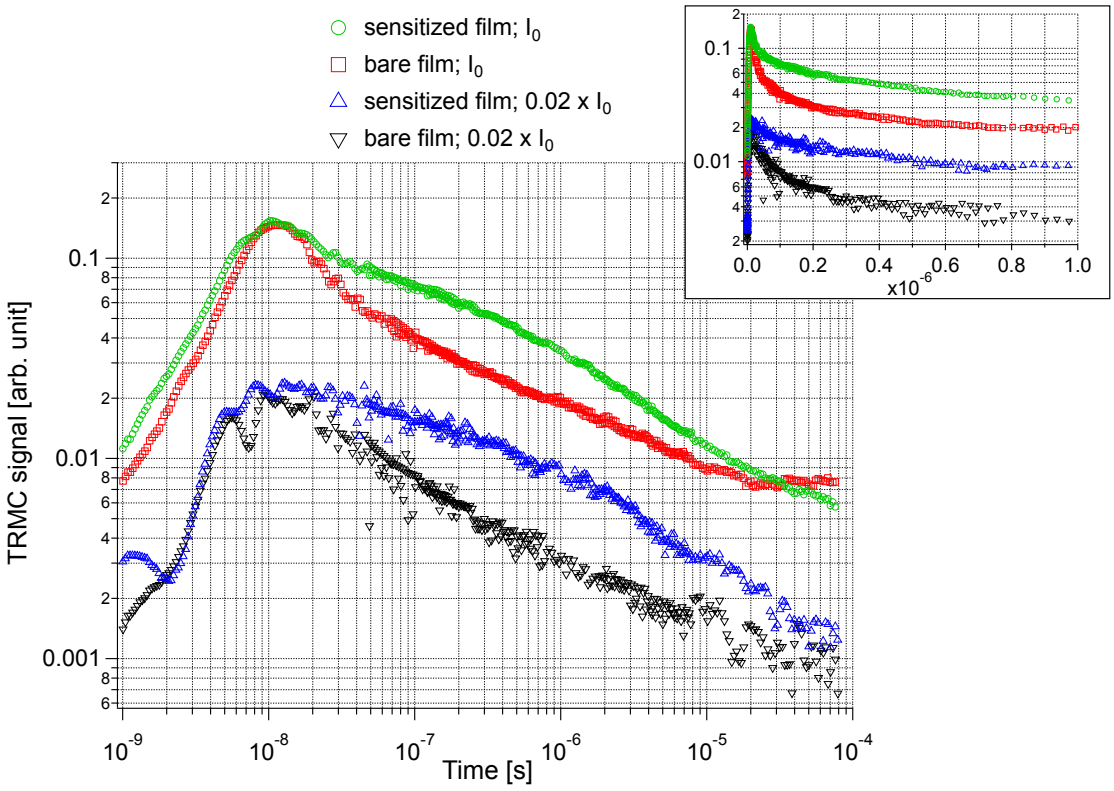

Figure 4.33: TRMC signals of bare and sensitized TiO_2 films in a double-logarithmic representation induced by laser pulses at 355 nm and different laser intensities (I_0 = 25 mJ/cm^2). Sensitization with N719 Ru-dye. The insert shows the TRMC signals in a semi-logarithmic representation in the short time range (0 - 1 μs).

100 μs with a coefficient of -0.45. This decay was faster than that in non-sensitized TiO_2 films (coefficient -0.4) in the same time range (Figure 4.33).

In contrast to the results on non-sensitized TiO_2 powders and films (Figures 4.29 - 4.30), the slope in the initial time range was less negative than after 1 μs in the sensitized TiO_2 powders and films in a double-logarithmic representation (Figures 4.32 - 4.33). However, the decay rate was still larger in this initial time range than after 1 μs as it was concluded from a semi-logarithmic representation (Insert in Figure 4.34).

TRMC signals excited by light pulses at 532 nm in sensitized TiO_2 powders and films are shown in Figure 4.35. At this wavelength, the dye was excited and excitation of the TiO_2 could be neglected (no signal was detected at 532 nm for non-sensitized TiO_2 powders or films). Consequently, the signals were due to

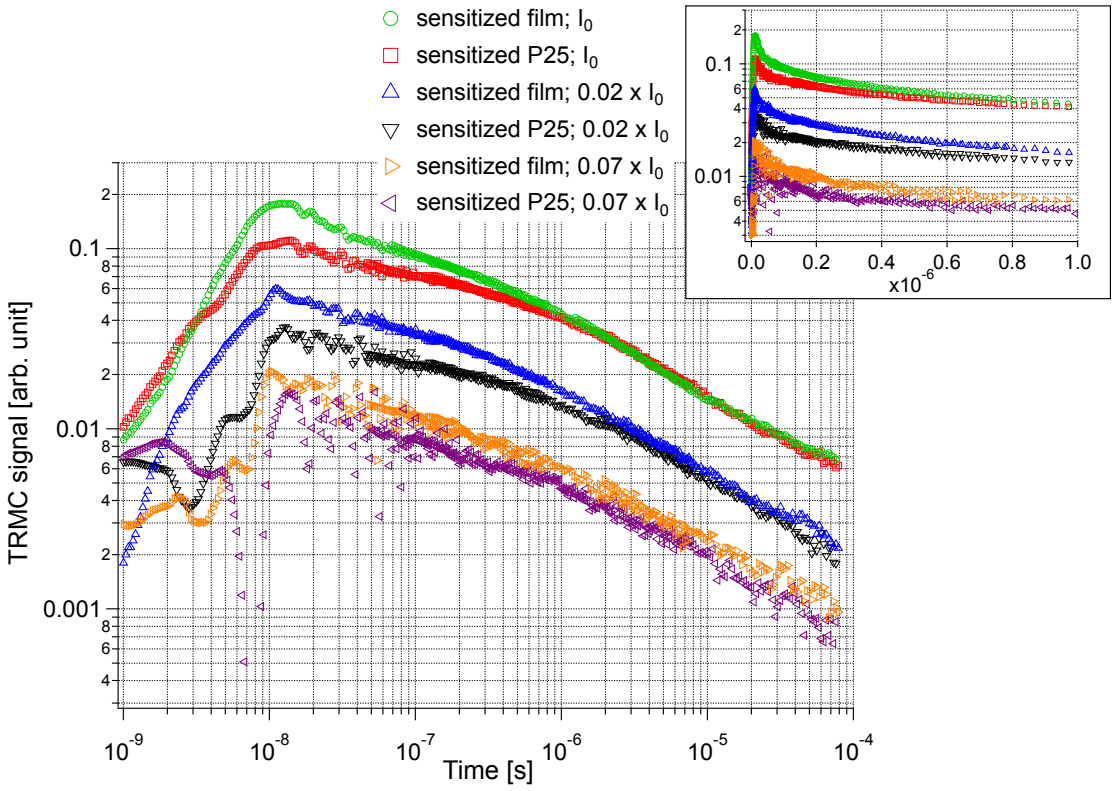

Figure 4.34: TRMC signals of sensitized TiO_2 powders (P25) and films in a double-logarithmic representation induced by laser pulses at 355 nm and different laser intensities (I_0 = 25 mJ/cm^2). Sensitization with N719 Ru-dye. The insert shows the TRMC signals in a semi-logarithmic representation in the short time range (0 - 1 μs).

electrons injected by the excited dye, where the compensating-, positive charge resided in the form of the dye cation. The shape of the signals was approximately the same for films and for powders, although the initial decay in the sensitized TiO_2 film was somewhat faster (Insert in Figure 4.35). The signals in the films were at the same excitation density higher than in the powder. This indicates a more efficient attachment of dye molecules at the surface of the film.

4.3.3 Summarizing discussion

The identical decay between 1 μs - 100 μs of sensitized TiO_2 films and powders after as well 532 nm and 355 nm excitation pointed to electron-dye cation recombination as the underlying process (Figures 4.34 - 4.35). After 532 nm excitation, the dye cation was a direct result of the electron injection; however, after 355 nm excitation

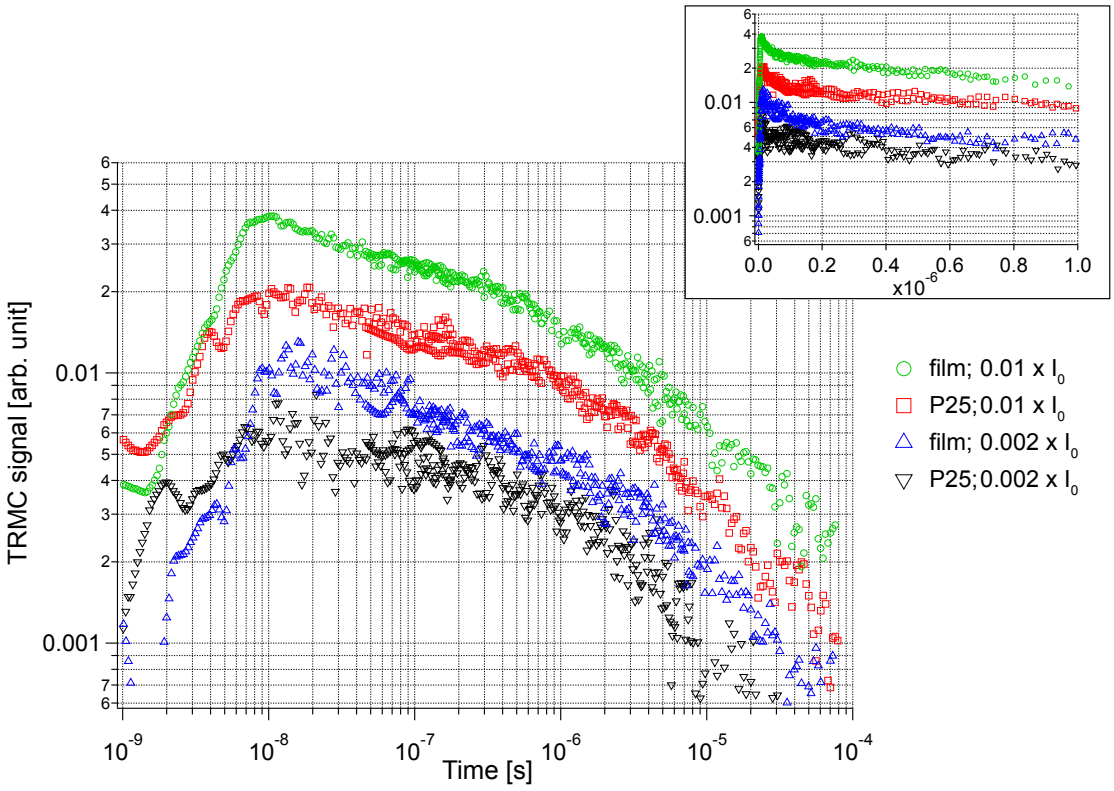

Figure 4.35: TRMC signals of sensitized TiO_2 powders (P25) and films in a double-logarithmic representation induced by laser pulses at 532 nm and different laser intensities (I_0 = 25 mJ/cm^2). Sensitization with N719 Ru-dye. The insert shows the TRMC signals in a semi-logarithmic representation in the short time range (0 - 1 μs).

a transfer of an excess hole to the adsorbed dye forming a dye cation had to be assumed. This was an indication that after 1 μs, electrons and dye cations were the main species and the signal decay was due to recombination between these species. Thus, there was a high probability for the trapping of a hole by an attached dye molecule.

The initial decay (0 - 100 ns) was probably mainly due to recombination of electrons with free holes and holes in defect states, although some electron trapping may have contributed to the decay. It had to be taken into account that the decay up to 40 ns was still influenced by the shape of the exciting laser pulse.

In Figures 4.32 and 4.33 it was observed that sensitized TiO_2 powders and films had initially a lower decay rate and after 300 ns a higher decay rate than non-sensitized TiO_2. This was probably due to the much wider distribution of holes

and therefore a much wider distribution of rate parameters for electron/trapped hole recombination in the non-sensitized material than in the sensitized material. The initially higher decay rate for non-sensitized TiO_2 samples indicates a fast recombination with a large distribution of available states. Subsequently, as the density of accessible states in the non-sensitized sample decreased, the decay due to recombination of electrons and localized dye cations was faster in the sensitized samples.

4.3.4 Comparison of sensitized and bare nanoporous ZnO films

ZnO has been introduced as an alternative electron-conducting medium with a high internal surface area for DSC [191–193]. The band gap (3.2 eV) and energetic position of the valence band maximum and conduction band minimum in ZnO are similar; therefore, it is possible to apply electrodes made up of ZnO nanoparticles in dye-sensitized solar cells [194, 195]. However, a dissolution process of the ZnO occurred during long-time sensitization and the formation of Zn^{2+}/dye complexes in the pores of the ZnO results in a decrease of the net yield for charge carrier injection [191, 196].

Figure 4.36 presents TRMC signals of bare and sensitized ZnO films induced by laser pulses at 355 nm. ZnO films were treated with N719 and "black dye" Ru-dye sensitizers. In contrast to the prolonged decay observed in sensitized TiO_2 films (Section 4.3.2), the decay was significantly accelerated for sensitized ZnO films. Within 500 ns less than 1% of the signal remained. After 355 nm excitation, electron-hole pairs are formed directly by band gap excitation of the ZnO. The accelerated decay for samples treated with the sensitizers indicates the formation of an additional decay channel upon dye adsorption. It has been reported that the adsorption of Ru-dyes leads to the formation of dye agglomerates in the ZnO film, due to the dissolution of Zn^{2+} ions binding to the dye molecules [196]. Although the times for dye adsorption by immersing the ZnO samples in the dye solution were reduced to two hours to prevent dissolution of ZnO, it appears that additional recombination states were introduced.

Figure 4.37 compares the microwave transients obtained from excitation of the ZnO films by laser pulses at 355 and 532 nm. In contrast to the formation of electron-hole pairs after 355 nm excitation, 532 nm pulses led to the excitation of

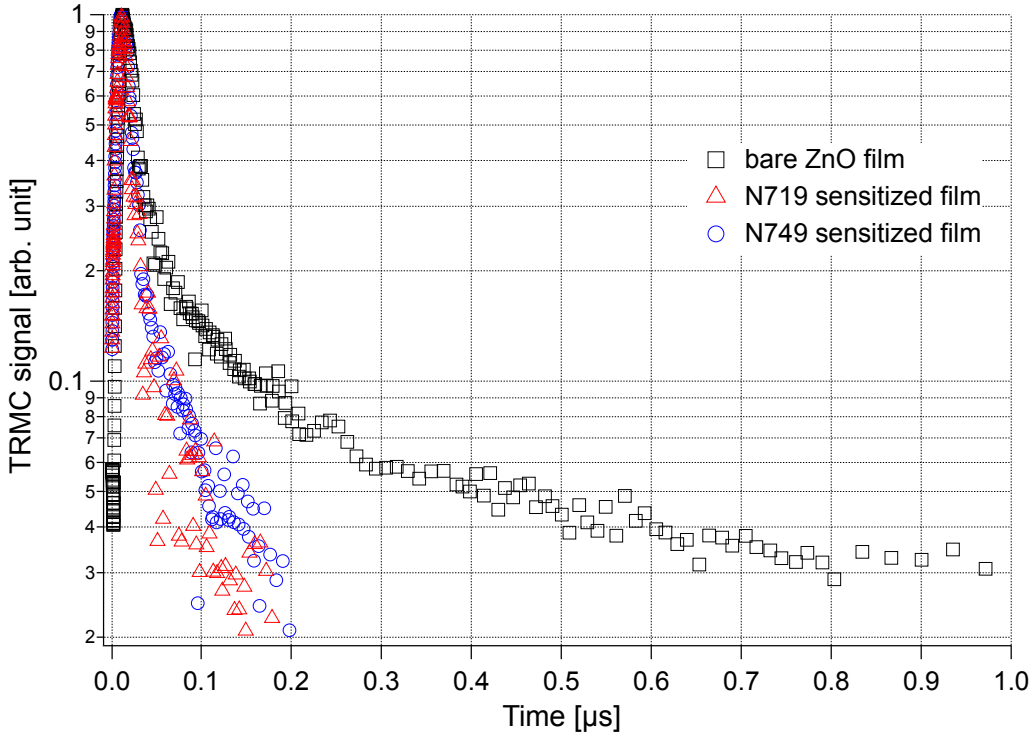

Figure 4.36: Normalized TRMC signals of bare and sensitized ZnO films induced by laser pulses at 355 nm. Sensitizers were the Ru-dyes N719 and N749 ("black dye"). Laser intensity: 0.6 mJ/cm^2.

the dye followed by a possible injection of electrons into the conduction band of the ZnO and a positive state in form of the dye cation. The decay after 532 nm illumination showed a drastic decrease in decay rate, with very similar transients observed for the samples sensitized with N719 and black dye, respectively. Some conclusions on the origin of the charge carrier decay could be drawn from the comparison of TRMC transients presented in Figure 4.36 after 355 nm excitation and Figure 4.37 after 532 nm excitation.

If the decay after 355 nm excitation was due to electron trapping, the adsorption of the dye would lead to an increase of the density of states in which trapping can occur, which would explain the observed accelerated decay (Figure 4.36). However, since the decay observed after 532 nm excitation was significantly slower, this explanation seemed improbable. Here, in the assumed case of electron trapping, the same amount of trapping states would be available for the photoinjected electrons

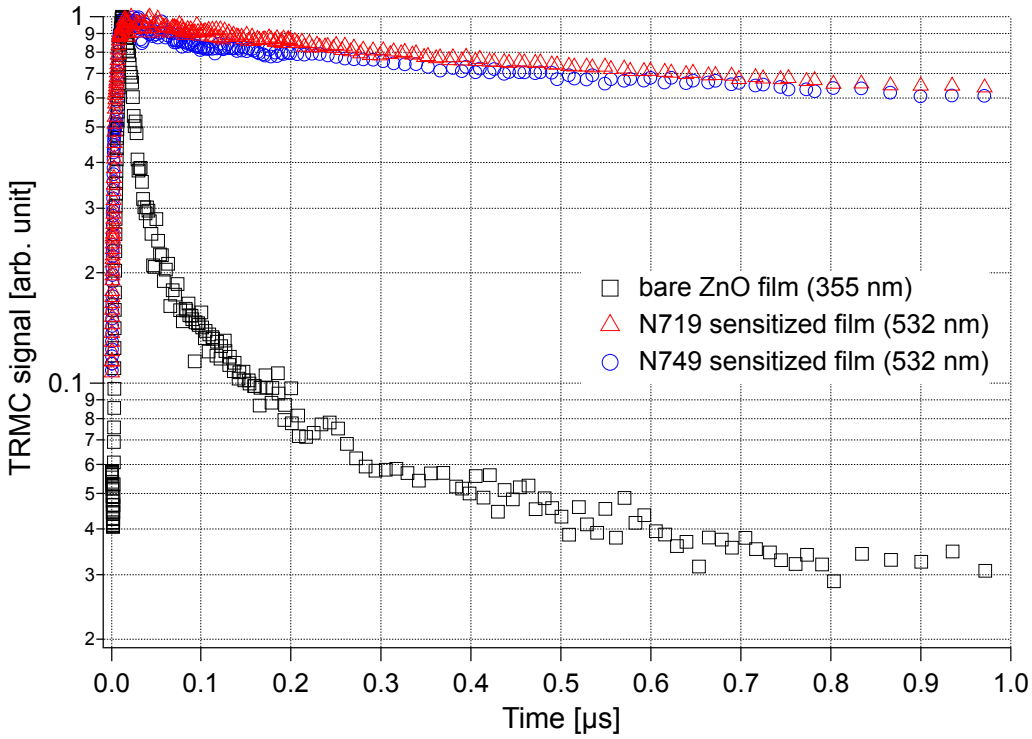

Figure 4.37: Normalized TRMC signals of bare and sensitized ZnO films induced by laser pulses at 355 and 532 nm. Sensitizers were the Ru-dyes N719 and N749 ("black dye"). Laser intensity: 0.6 mJ/cm^2 and 0.8 mJ/cm^2, respectively.

and the decay should be similar. Thus, trapping of electrons can be excluded as the main decay channel for charge carriers, so recombination is the most important decay channel.

As mentioned above, the excitation with pulses at 355 nm led to the formation of electron-hole pairs. Excitation of the dye with 532 nm laser pulses led to a localized hole in the form of the dye cation and an electron (after fast injection) in the conduction band of the ZnO. As recombination was considered to be the main mechanism for charge carrier decay, the faster decay observed for sensitized samples after 355 nm excitation could be attributed to a higher electron-hole recombination rate upon dye adsorption, whereas the prolonged decay after 532 nm excitation was due to the separation of injected electrons in the ZnO and the positive charge in form of the dye cation with a relatively low cross section for the recombination between electrons and dye cations.

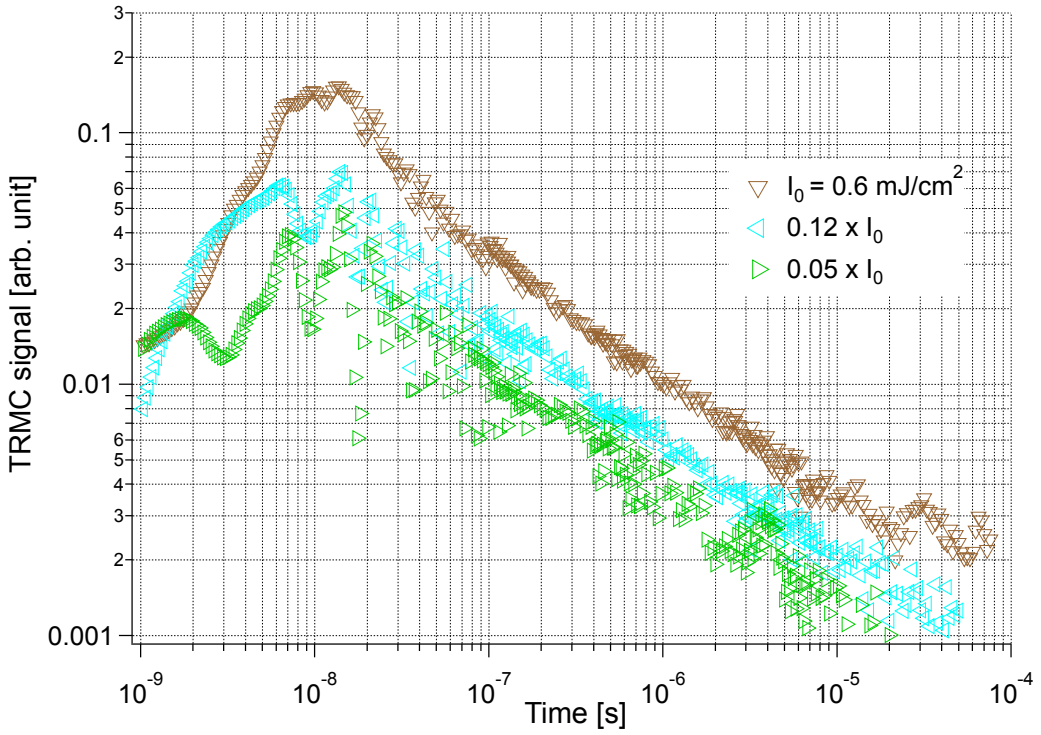

Figure 4.38: TRMC signals of a bare ZnO film in a double-logarithmic representation induced by laser pulses at 355 nm and different laser intensities (I_0 = 0.6 mJ/cm^2).

The double-logarithmic presentation of the TRMC signal after 355 nm excitation in the bare ZnO film revealed an extended decay that approached a power law with a coefficient of -0.6 (Figure 4.38). The amplitude displayed a sublinear dependence on the excitation density for bare ZnO screen-printed films.

The sublinear dependence on the excitation density indicates a fast initial recombination process within the laser pulse length which is ascribed to fast electron-hole recombination. Hence, considering the results from Kroeze et al. [187] presented above (cf. Section 4.3.1), trapping during the excitation played only a minor role and recombination during the excitation led to a sublinear dependence of the amplitude. Moreover, the decay in the longer time range was characterized by a power law with a weak trend to become faster with higher excitation densities. This decay may (at least partially) have been due to recombination.

Likewise, the TRMC signal amplitude for different excitation intensities at 532 nm revealed a sublinear dependence of the initial amplitude (Figure 4.39). This

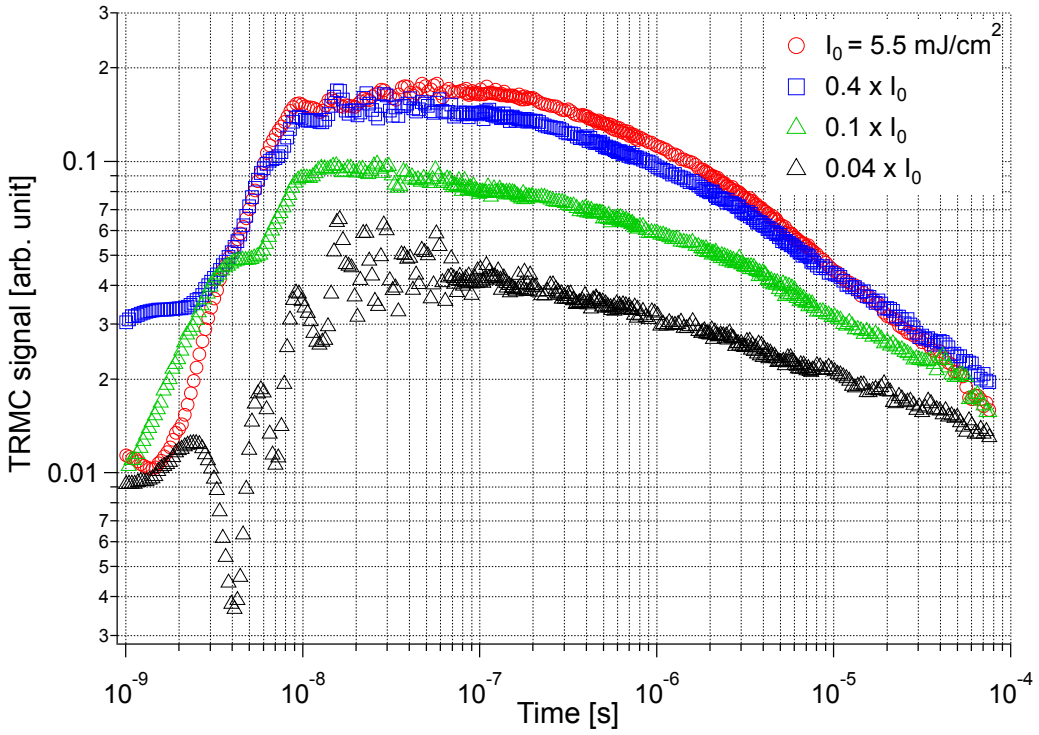

Figure 4.39: TRMC signals of a sensitized ZnO film in a double-logarithmic representation induced by laser pulses at 532 nm and different laser intensities (I_0 = 5.5 mJ/cm^2).

might be due to a reduction of the electron injection efficiency e.g. by a nonlinear absorption at high excitation densities as indicated by the similar amplitudes of the two upper curves in the graph.

4.3.5 Comparison of sensitized and bare ZnO nanorods

Experiments were also performed on nanocolumnar ZnO layers. Nanorod ZnO electrodes have been proposed as an alternative electron conducting material with high internal surface area for DSC. Compared to mesoporous metal oxide films, the ordered arrays of rods provide a direct conduction path for electrons and may offer improved transport compared to films of sintered nanoparticles. However, with increasing rod length, the rod diameter increases accordingly, thus limiting the aspect ratio of the arrays. A low aspect ratio leads to a low light absorption

which currently limits the efficiency of nanorod based DSC [191]. Due to the absence of grain boundaries in the ZnO nanorods, electron mobility was found to be much higher than in TiO_2 based electrodes [192]. Furthermore, the much higher equilibrium electron concentration of 10^{18} - 10^{19} cm^{-3} and the larger diameter of the rods might enable a macroscopic internal electric field which was proposed to assist charge carrier transport by separating injected electrons from the electrolyte and sweeping them towards the collecting electrode [192].

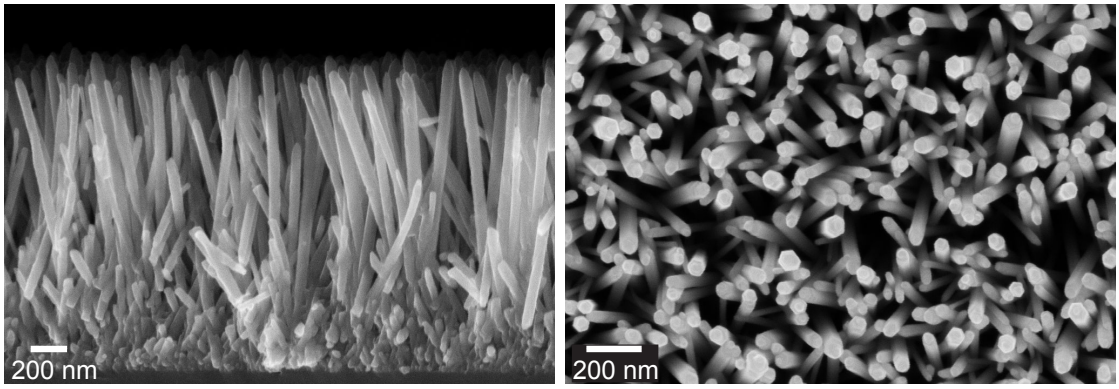

(a) (b)

Figure 4.40: SEM image of an array of bare ZnO nanorods on glass.

Figure 4.40(a) presents a cross section scanning electron microscopy of a ZnO nanorod array. The nanorods were mainly orientated perpendicular to the substrate with an average length of ca. 1.5 μm. The diameter varied from ca. 30 - 100 nm as observed in a magnified view in Figure 4.40(b). Higher magnification revealed its hexagonal faceting and a terraced structure to its slightly tapered tip (Figure 4.41(a)). Sensitization of the nanorods led to a slightly increased roughness of the surface as depicted in Figure 4.41(b). However, form and number of the nanorods appeared to be unaffected by the sensitization process.

The normalized TRMC signals after 355 nm excitation of sensitized and bare ZnO nanorods are presented in Figure 4.42. The lack of significant differences in the decay of the sensitized sample indicates that the dye has no major effect on the recombination of generated charge carriers upon 355 nm excitation.

The intensity dependence of the TRMC amplitude for bare ZnO nanorod electrodes after 355 nm excitation is presented in Figure 4.43. The TRMC signal amplitude showed a superlinear (approaching linear) increase with the excitation

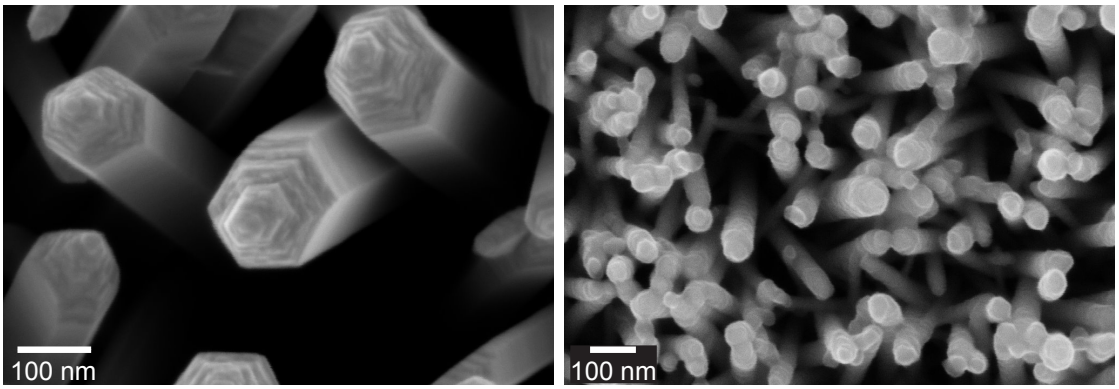

(a) bare (b) sensitized

Figure 4.41: SEM image of bare and sensitized ZnO nanorods on glass.

density. The sublinear intensity dependence for nanoporous ZnO films was explained by a fast initial electron-hole recombination (cf. Figure 4.38). In the case of the nanorods recombination did not seem to play an important role and the weak superlinearity could be explained by the interaction of electrons with traps, in the range where trap saturation (i.e. number of traps and that of excess electrons lie in the same order of magnitude) occurred.

A comparison of the decay in Figure 4.44 (TRMC signals of sensitized ZnO nanorods induced by laser pulses at 532 nm and 355 nm) revealed a slower initial decay rate upon 532 nm excitation, leading to a faster decay after 300 ns. Since the trapping sites were identical for 532 nm and 355 nm excitation, the differences between both signals must be due to recombination. Furthermore, the slower decay after 300 ns upon 355 nm excitation was due to the larger distribution of trapped excess holes. Such behavior is analogous to the one found in sensitized and non-sensitized TiO_2 (Figures 4.32 - 4.33), which was discussed a the end of Section 4.3.3. In the case of excitation with 355 nm, at least two decay channels might attribute to the observed transient: the fast initial recombination of electron-hole pairs upon band gap excitation and the recombination of electrons with the oxidized dye.

For the excitation with 532 nm, the direct recombination of electron-hole pairs could be excluded and the recombination of electrons with the dye cation remained. This indicates that up to 300 ns, the recombination between electrons and holes (probably via defects) is faster than between electrons and dye cations,

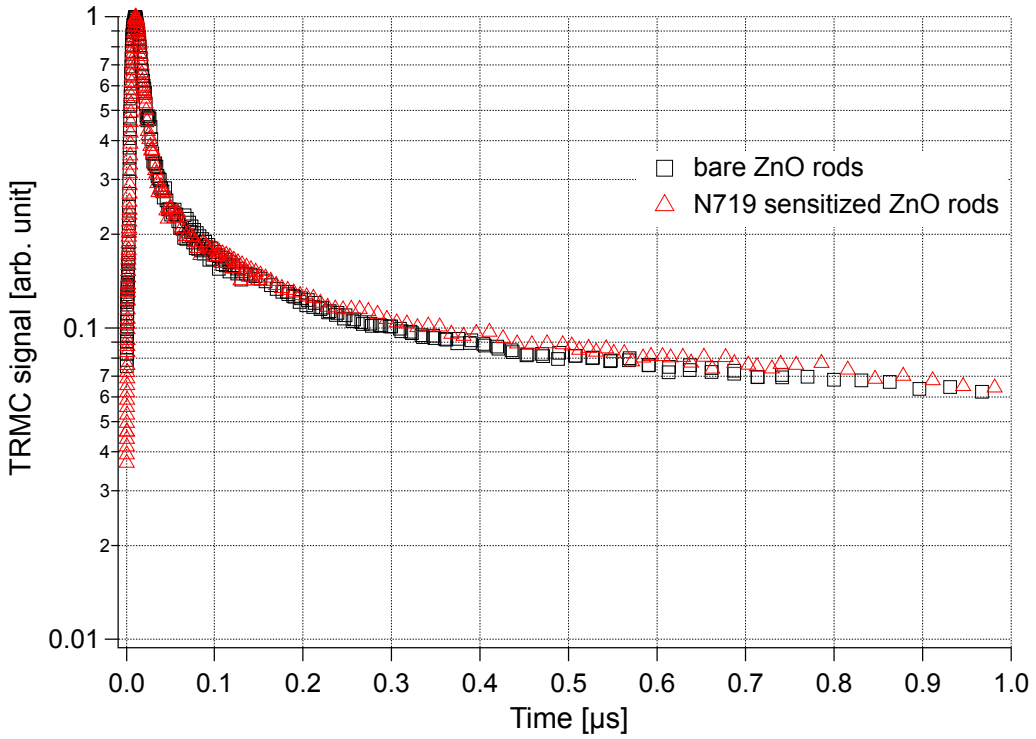

Figure 4.42: Normalized TRMC signals of bare and sensitized ZnO nanorods induced by laser pulses at 355 nm. Laser intensity: 140 μJ/cm^2.

as suggested in Figure 4.44 by the slower initial decay after 532 nm excitation. After 300 ns, this relation changed as the first recombination process became faster than the second one. In view of the observed extended decay, this explanation implies that both recombination processes are highly dispersive. This is clear for the non-sensitized samples where holes can be free (probably not so many) and localized in traps with very different energies and accessibility (i.e. by the presence of space charge regions). For the sensitized samples this indicates that a large range of configurations are present for the dye and the dye cation, where also the presence of a possible space charge region may play a role. Thus, the decay after 355 nm excitation depended mainly on the recombination of electron-hole pairs. The recombination of electrons with the dye cation is preponderant at 532 nm excitation.

A weak superlinear dependence of the excitation density in the TRMC amplitude was also observed for 532 nm illumination of sensitized ZnO nanorods (Figure

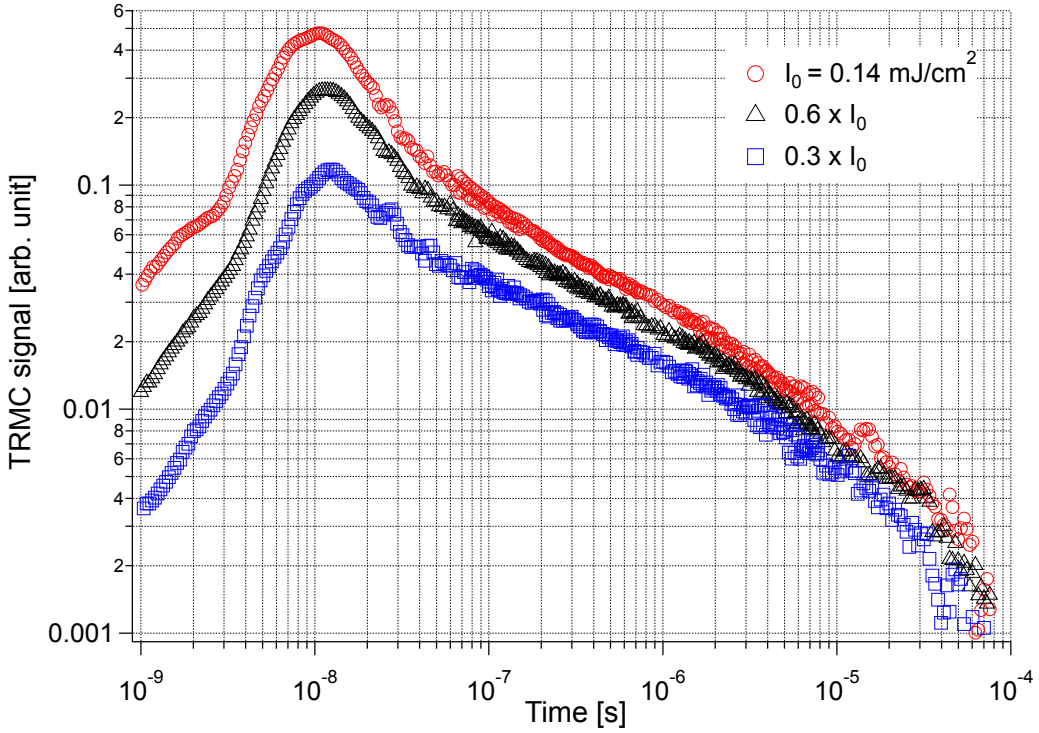

Figure 4.43: TRMC signals of bare ZnO nanorods in a double-logarithmic representation induced by laser pulses at 355 nm and different laser intensities (I_0 = 140 μJ/cm^2).

4.45), which was in contrast to the saturation of the signal for nanoporous ZnO films (Figure 4.39). The fact that superlinearity occurred for both 355 nm (bare ZnO nanorods, Figure 4.43) and 532 nm excitation (sensitized ZnO nanorods, Figure 4.45) led us to conclude that the fast initial decay is independent of the presence of the dye. Therefore, this superlinearity is due to trap saturation. The process of trapping competes with recombination; consequently, the range of the superlinearity depends on the decay rate due to recombination.

4.3.6 Conclusions

The main difference between the colloidal TiO_2 powder and the film prepared by screen-printing was the connectivity between the colloid. Hence, the faster decay in the film (Figures 4.29 - 4.31) was due to the interaction of electrons with defects related to the connection between the particles. The number of these interactions

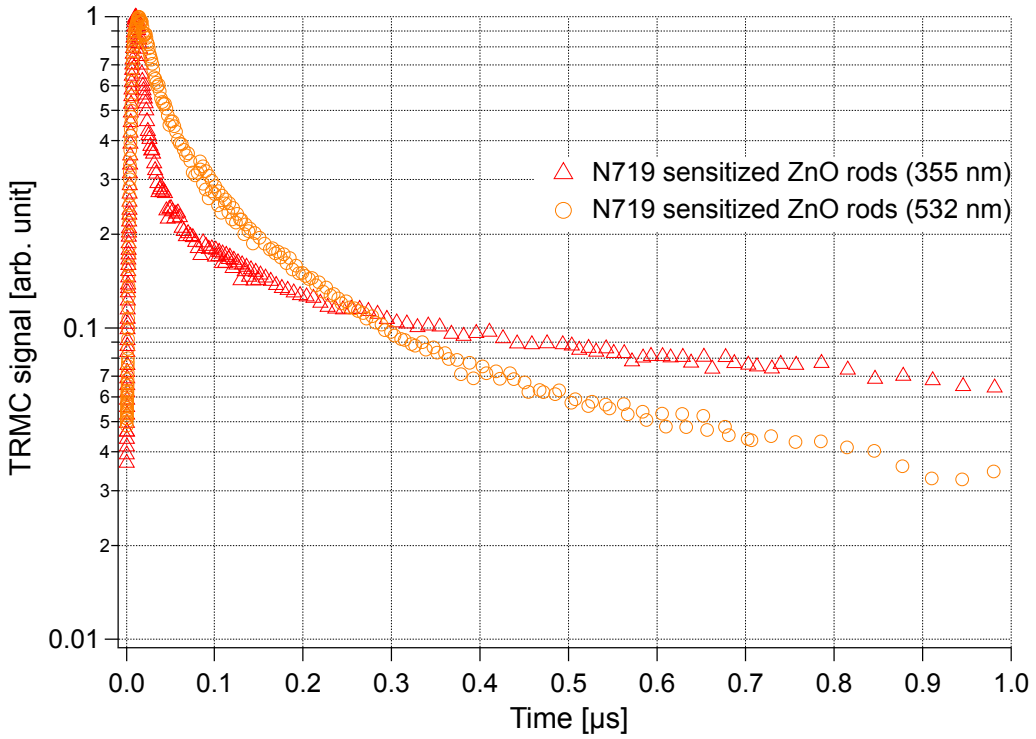

Figure 4.44: Normalized TRMC signals of sensitized ZnO nanorods induced by laser pulses at 355 and 532 nm. Laser intensity: 140 $\mu J/cm^2$ and 1.6 mJ/cm^2, respectively.

was limited; therefore, saturation may have led to the slow final decay in the film at the highest excitation density (Figures 4.30 - 4.31).

In the case of the TiO_2 samples, although the evidence was less convincing when compared to the ZnO samples, recombination might also be the main decay channel.

It is important to note that the TRMC signals displayed an identical behavior in sensitized TiO_2 samples between 1 μs and 100 μs at 532 nm and 355 nm excitation. This effect suggested that adsorbed neutral dye molecules could serve as hole traps. This was not the case for sensitized ZnO, where a large difference between the decay behavior after 532 nm and 355 nm excitation was observed.

The similarities between the decay in sensitized TiO_2 powders and films (Figure 4.34) suggested that intergrain transport did not play an important role in the time range considered. Under our experimental conditions, the driving force for intergrain transport was only the gradient due to inhomogeneous charge carrier

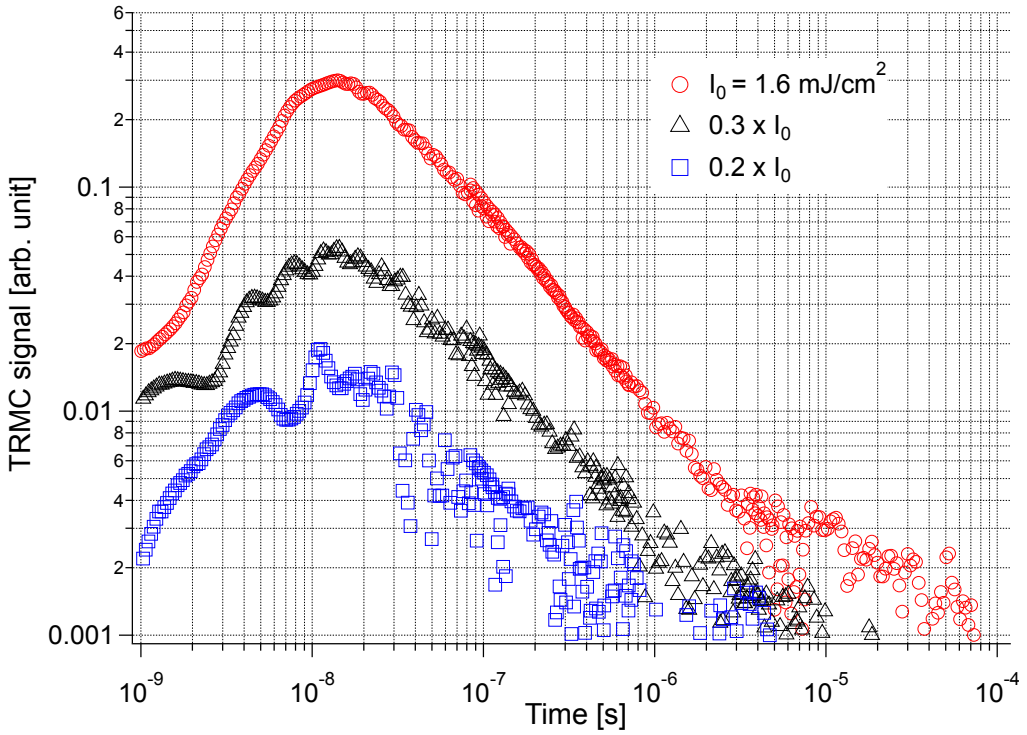

Figure 4.45: TRMC signals of sensitized ZnO nanorods in a double-logarithmic representation induced by laser pulses at 532 nm and different laser intensities (I_0 = 1.6 mJ/cm^2).

generation. Thus, intergrain transport at 532 nm excitation was rather improbable.

The dispersive character of all transients in these colloidal systems led us to interpret them in terms of multiple trapping in analogy to (a-Si:H) [189]. However, the information available did not allow a microscopic interpretation.

As stated above, the interaction of electrons with a wide distribution of both trapping and hole states led to a wide distribution of interaction parameters and thus of decay kinetics. In addition, it must be taken into account (in any case for ZnO with a large concentration of dark charge carriers) that space charge regions were present and strongly modulated the interaction of electrons and holes.

In general, the study of ZnO and TiO_2 colloidal systems revealed interesting differences between these two compounds. In the case of nanoporous ZnO films, the apparent destructive influence of the dye attachment led to a drastically reduced electron lifetime after 355 nm excitation (Figure 4.36). This effect was not as

significant in the case of dye excitation after 532 nm (Figure 4.37); nevertheless, it has to be considered for the application of ZnO e.g. as electrodes in DSC. If the TRMC signal after 532 nm excitation originated at least partially from disconnected Zn^{2+}/dye complexes, then the charge injection and collection in a working DSC might be limited. Another effect found only in TiO_2 was related to the state of the dye at the particle surface and the probability of hole trapping by the neutral dye molecule (Figures 4.32 - 4.33).

For ZnO nanorods, the efficiency of sensitization was clearly improved; thus, the use of nanorods seemed preferable for photovoltaic purposes. In addition, the use of different dyes for sensitization could further improve the ZnO behavior.

5 Summary

The efficiency of the quasi-solid-state dye-sensitized solar cell developed by Junghänel and Tributsch, the so-called Nano Surface Conductivity Solar Cell (NSCSC), was improved from 2% to 3.5% introducing a compact TiO_2 underlayer, modifying the surface of the mesoporous TiO_2 electrode, optimizing the deposition process of the electrolyte film, and replacing the platinum counter electrode by a carbon layer.

Space-resolved photocurrent images revealed the importance of a homogeneous distribution of the electrolyte film. An uneven dispersion led to localized areas of high and low photocurrents, whereas the latter were attributed to an insufficient concentration of the redox couple.

Impedance spectroscopy was performed on cells containing different concentrations of the redox couple. By modeling the spectra using an equivalent circuit with a transmission line of resistive and capacitive elements, the characteristic parameters of electron transport in the TiO_2, such as diffusion length and electron lifetime were obtained. The measurements indicated that the transport of the positive charge to the counter electrode is the main process limiting the efficiency of the cells.

Excess charge carrier decay in functioning devices was analyzed by contactless transient photoconductance measurements in the microwave frequency range (TRMC). The lifetime of the photogenerated charge carriers was observed to decrease with increasing applied potential, reaching its maximum close to the open-circuit potential of the cell, where the photocurrent density was minimal, i.e. the potential dependent decay observed was limited by the injection of electrons into the front contact. The functioning of this NSCSC indicated that the transport of the positive charge occurs by solid-state diffusion at the surface of the TiO_2 particles.

TRMC measurements on subset devices in the form of sensitized TiO_2 layers

revealed charge carrier kinetics strongly dependent on the concentration of the redox species in the electrolyte film, having the fastest decay at the lowest concentration of the redox couple. This was due to the regeneration of the oxidized dye by iodide, screening the positive charge from recombination with injected electrons. The adsorption of cations such as Li^+ led to a relatively weak increase of the electron lifetime, although in combination with a redox couple these effects were less clear.

The replacement of the iodide/iodine redox couple by the kinetically fast ferrocene/ferrocenium system caused a dramatic increase of the decay rates of photogenerated charge carriers in subset devices. This increase was attributed to a large availability of recombination sites introduced by the presence of ferrocene/ferrocenium. Thus, showing the importance of the kinetically slow reduction rates of the oxidized redox couple iodide/iodine, leading to an increase of the electron lifetime by the reduction of the dye cation. For the ferrocene/ferrocenium system the dominant decay channel was ascribed to the fast recombination of injected electrons with ferrocenium.

The analysis of charge carrier kinetics in TiO_2 powders and films displayed a decrease of the decay rate upon dye-sensitization after band-to-band excitation with laser pulses at 355 nm. This was attributed to a reduced recombination rate due to the trapping of excess holes by adsorbed dye molecules.

In the case of ZnO films, the presence of the dye induced a significantly accelerated decay after excitation at 355 nm, which was assigned to a higher electron-hole recombination rate upon dye adsorption and the introduction of additional recombination states through dissolution of the ZnO. However, after exciting the sample at 532 nm the prolonged decay observed is explained by the separation of injected electrons in the ZnO and a positive charge in the form of the dye cation with a relatively low cross section for the recombination between electrons and dye cations.

In contrast to the ZnO films, ZnO nanorods displayed no such destructive influence of the dye adsorption. Furthermore, after exciting the sample at 355 nm, the decay was found to be independent of the dye and mainly depending on the recombination of electron-hole pairs and electrons with the dye cation at 355 nm and 532 nm, respectively.

Zusammenfassung

Der Wirkungsgrad der von Junghänel und Tributsch entwickelten Farbstoffsolarzelle unter Verwendung eines quasi-Festelektrolyten, die sogenannte Oberfächen-Leitfähigkeits-Solarzelle (NSCSC), konnte durch die Einbringung einer kompakten TiO_2 Blockierschicht, einer Oberflächenbehandlung der mesoporösen TiO_2 Elektrode, einer optimierten Elektrolytauftragung sowie dem Ersatz der Gegenelektrode aus Platin durch eine Kohlenstoffschicht von 2% auf 3,5% gesteigert werden.

Ortsaufgelöste Photostrommessungen zeigten die Notwendigkeit einer homogenen Verteilung des Elektrolytfilms. Eine ungleichmäßige Verteilung führte zu lokalisierten Gebieten von hohen bzw. niedrigen Photoströmen, wobei letztere einer ungenügenden Konzentration des Redoxpaares zugewiesen wurden.

Impedanzmessungen wurden in Abhängigkeit der Konzentration des Redoxpaares im Elektrolytfilm der Zellen durchgeführt. Eine Modellierung der Spektren mittels eines Ersatzschaltbildes, bestehend aus Leitungsabschnitten mit resistiven und kapazitiven Elementen, erlaubte die Bestimmung der charakteristischen Parameter des Elektronentransports in der TiO_2 Schicht. Die Messungen deuteten darauf hin, dass der Transport der positiven Ladung zur Gegenelektrode der maßgebliche, die Effizienz der Zelle beschränkende Faktor ist.

Die Kinetik von Überschussladungsträgern in den Solarzellen wurde durch die kontaktlose Methode der transienten Photoleitfähigkeitsmessung im Mikrowellenbereich untersucht. Die Lebensdauer der photogenerierten Ladungsgträger zeigte eine Abnahme mit zunehmenden Potential, wobei das Maximum nahe der Leerlaufspannung der Zelle lag, wo der Photostrom minimal war, d.h. die Injektion von Elektronen in den Frontkontakt beschränkte das Abklingen. Die Funktion der NSCSC deutete darauf hin, dass der Transport der positiven Ladung durch Festkörperdiffusion auf der Oberfläche der TiO_2 Teilchen stattfindet.

TRMC Messungen an Teilsystemen, bestehend aus sensibilisierten TiO_2 Schichten, zeigten eine starke Abhängigkeit der Ladungsträgerkinetik von der Konzen-

tration des Redoxpaares im Elektrolytfilm, wobei das schnellste Abklingen bei der niedrigsten Redoxkonzentration auftrat. Dies wurde der Regeneration des oxiderten Farbstoffes zugewiesen, welche durch die Abschirmung der positiven Ladung die Reduzierung der Rekombinationsrate und somit das verlangsamte Abklingen bewirkt. Die Adsorption von Kationen (z.B. Li^+) führte zu einem geringen Anstieg der Elektronenlebensdauer. Jedoch waren diese Effekte in Kombination mit dem Redoxpaar weniger stark ausgeprägt.

Der Ersatz des Iod/Iodid Redoxpaares mit dem kinetisch schnellen Ferrocen/Ferrocenium Paar führte zu einem starken Anstieg der Abklingraten von photogenerierten Ladungsträgern. Dies wurde durch die durch Anwesenheit von Ferrocen/Ferrocenium bedingte Zunahme von Rekombinationszentren erklärt. Somit konnte die Bedeutung der kinetisch langsamen Reduktionsraten des oxidierten Redoxpaares Iod/Iodid gezeigt werden. Im Falle des Ferrocen/Ferrocenium Paares wurde der wichtigste Abklingkanal der schnellen Rekombination von injizierten Elektronen und Ferrocenium zugesprochen.

Die Untersuchung der Ladungsträgerkinetik in TiO_2 Pulvern und Schichten zeigte eine Verlangsamung der Abklingrate in Folge der Farbstoffsensibilisierung nach Anregung des Halbleiters mit Laserlicht bei 355 nm. Dies wurde durch eine verringerte Rekombinationsrate aufgrund des Einfangens von positiven Überschussladungsträgern (Löchern) durch adsorbierte Farbstoffmoleküle erklärt.

Bei ZnO Schichten konnte ein beschleunigtes Abklingverhalten in Anwesenheit des Farbstoffes nach Anregung mit 355 nm Laserpulsen beobachtet werden, welches sowohl einer höheren Elektron-Loch Rekombinationsrate als auch zusätzlichen Rekombinationszentren, bedingt durch die teilweise Auflösung des ZnO nach Farbstoffadsorption zugeschrieben wurde. Jedoch wurde nach Anregung mit 532 nm Laserpulsen ein verlangsamtes Abklingen beobachtet, welches durch die örtliche Trennung von injizierten Elektronen im ZnO und positiver Ladung in Form des Farbstoffkations erklärt wird.

ZnO Nanorods hingegen zeigten keinen solchen destruktiven Einfluss der Farbstoffadsorption. Darüber hinaus war hier das Abklingverhalten nach Anregung mit 355 nm Laserlicht unabhängig vom Farbstoff und somit hauptsächlich bestimmt durch Elektron-Loch Rekombination im Falle von 355 nm, sowie Rekombination von Elektronen mit dem Farbstoffkation nach 532 nm Anregung.

Bibliography

[1] N. S. Lewis, G. Crabtree (Editors). *Basic Research Needs for Solar Energy Utilization*. Office of Science, U.S. Department of Energy, Washington, DC (2005).

[2] BMU-Publikationen: Erneuerbare Energien 2010. `http://www.erneuerbare-energien.de` (2011).

[3] J. G. Canadell, C. L. Quéré, M. R. Raupach, C. B. Field, E. T. Buitenhuis, P. Ciais, T. J. Conway, N. P. Gillett, R. A. Houghton, G. Marland. *Proc. Natl. Acad. Sci.* **104**, 18866 (2007).

[4] P. Tans. Trends in atmospheric carbon dioxide, NOAA/ESRL. `http://www.esrl.noaa.gov/gmd/ccgg/trends` (2010).

[5] International Panel on Climate Change (IPCC), Fourth Assessment Report: Climate Change. `http://www.ipcc.ch` (2007).

[6] EIA, U.S. Energy Information Administration, International Energy Outlook. `http://www.eia.doe.gov/oiaf/ieo/` (2010).

[7] P. Sirimane, H. Tributsch. *J. Solid State Chem.* **177**, 1789 (2004).

[8] M. Junghänel. *Novel aqueous electrolyte films for hole conduction in dye sensitized solar cells and development of an electron transport model*. Ph.D. thesis, Freie Universität Berlin (2007).

[9] A. E. Becquerel. *Compt. Rend.* **9**, 561 (1839).

[10] D. M. Chapin, C. S. Fuller, G. L. Pearson. *J. Appl. Phys.* **25**, 676 (1954).

[11] J. Moser. *Monatsh. Chem.* **8**, 373 (1887).

[12] H. Kallmann, M. Pope. *J. Chem. Phys.* **30**, 585 (1959).

[13] H. Gerischer, H. Tributsch. *Ber. Bunsenges. Phys. Chem.* **72**, 437 (1968).

[14] H. Tributsch, M. Calvin. *Photochem. Photobiol.* **14**, 95 (1971).

[15] B. O'Regan, M. Grätzel. *Nature* **353**, 737 (1991).

[16] S. M. Sze. *Physics of semiconductor devices.* John Wiley and Sons, New York, 2nd edition (1981).

[17] P. Würfel. *Physics of Solar Cells.* Wiley-VCH, Weinheim, 2nd edition (2009).

[18] K. Kalyanasundaram (Editor). *Dye-Sensitized Solar Cells.* EPFL Press, Lausanne (2010).

[19] N. S. Lewis. *Science* **315**, 798 (2007).

[20] M. A. Green, K. Emery, Y. Hishikawa, W. Warta. *Prog. Photovolt.* **19**, 84 (2011).

[21] M. A. Green. *Third generation photovoltaics: advanced solar energy conversion.* Birkhäuser (2006).

[22] W. Shockley, H. J. Queisser. *J. Appl. Phys.* **32**, 510 (1961).

[23] D. König, K. Casalenuovo, Y. Takeda, G. Conibeer, J. Guillemoles, R. Patterson, L. Huang, M. Green. *Physica E* **42**, 2862 (2010).

[24] R. D. Schaller, M. A. Petruska, V. I. Klimov. *Appl. Phys. Lett.* **87**, 253102 (2005).

[25] R. R. King, D. C. Law, K. M. Edmondson, C. M. Fetzer, G. S. Kinsey, H. Yoon, R. A. Sherif, N. H. Karam. *Appl. Phys. Lett.* **90**, 183516 (2007).

[26] H. Tributsch. *Photochem. Photobiol.* **16**, 261 (1972).

[27] M. T. Spitler, M. Calvin. *J. Chem. Phys.* **66**, 4294 (1977).

[28] H. Tsubomura, M. Matsumura, Y. Nomura, T. Amamiya. *Nature* **261**, 402 (1976).

[29] A. Fujishima, K. Honda. *Nature* **238**, 37 (1972).

[30] R. Wang, K. Hashimoto, A. Fujishima, M. Chikuni, E. Kojima, A. Kitamura, M. Shimohigoshi, T. Watanabe. *Nature* **388**, 431 (1997).

[31] A. Fujishima, T. N. Rao, D. A. Tryk. *J. Photoch. Photobio. C* **1**, 1 (2000).

[32] Y. Paz, Z. Luo, L. Rabenberg, A. Heller. *J. Mater. Res.* **10**, 2842 (1995).

[33] S. N. Frank, A. J. Bard. *J. Phys. Chem.* **81**, 1484 (1977).

[34] H. Gerischer, N. Sorg. *Electrochim. Acta* **37**, 827 (1992).

[35] A. Zaban, S. Ferrere, J. Sprague, B. A. Gregg. *J. Phys. Chem. B* **101**, 55 (1997).

[36] S. Ito, P. Chen, P. Comte, M. K. Nazeeruddin, P. Liska, P. Péchy, M. Grätzel. *Prog. Photovolt.* **15**, 603 (2007).

[37] L. Kavan, M. Grätzel, S. E. Gilbert, C. Klemenz, H. J. Scheel. *J. Am. Chem. Soc.* **118**, 6716 (1996).

[38] J. F. Banfield, B. L. Bischoff, M. A. Anderson. *Chem. Geol.* **110**, 211 (1993).

[39] K. J. MacKenzie. *Trans. J. Brit. Ceram. Soc.* **74**, 29 (1975).

[40] R. N. Blumenthal, J. Baukus, W. M. Hirthe. *J. Electrochem. Soc.* **114**, 172 (1967).

[41] A. V. Hippel, J. Kalnajs, W. B. Westphal. *J. Phys. Chem. Solids* **23**, 779 (1962).

[42] P. Wang, S. M. Zakeeruddin, J. E. Moser, M. K. Nazeeruddin, T. Sekiguchi, M. Grätzel. *Nat. Mater.* **2**, 402 (2003).

[43] M. K. Nazeeruddin, A. Kay, I. Rodicio, R. Humphry-Baker, E. Mueller, P. Liska, N. Vlachopoulos, M. Grätzel. *J. Am. Chem. Soc.* **115**, 6382 (1993).

[44] A. Islam, H. Sugihara, K. Hara, L. P. Singh, R. Katoh, M. Yanagida, Y. Takahashi, S. Murata, H. Arakawa. *J. Photoch. Photobio. A* **145**, 135 (2001).

[45] M. K. Nazeeruddin, P. Péchy, M. Grätzel. *Chem. Commun.* **18**, 1705 (1997).

[46] C. Klein, M. K. Nazeeruddin, D. D. Censo, P. Liska, M. Grätzel. *Inorg. Chem.* **43**, 4216 (2004).

[47] D. Kuciauskas, M. S. Freund, H. B. Gray, J. R. Winkler, N. S. Lewis. *J. Phys. Chem. B* **105**, 392 (2001).

[48] R. Argazzi, G. Larramona, C. Contado, C. A. Bignozzi. *J. Photoch. Photobio. A* **164**, 15 (2004).

[49] A. Islam, H. Sugihara, K. Hara, L. P. Singh, R. Katoh, M. Yanagida, Y. Takahashi, S. Murata, H. Arakawa, G. Fujihashi. *Inorg. Chem.* **40**, 5371 (2001).

[50] E. A. M. Geary, L. J. Yellowlees, L. A. Jack, I. D. H. Oswald, S. Parsons, N. Hirata, J. R. Durrant, N. Robertson. *Inorg. Chem.* **44**, 242 (2005).

[51] G. M. Hasselmann, G. J. Meyer. *Z. Phys. Chem* **212**, 39 (1999).

[52] N. Alonso-Vante, J.-F. Nierengarten, J.-P. Sauvage. *J. Chem. Soc. Dalton* **11**, 1649 (1994).

[53] S. Ferrere, B. A. Gregg. *J. Am. Chem. Soc.* **120**, 843 (1998).

[54] L. Schmidt-Mende, W. M. Campbell, Q. Wang, K. W. Jolley, D. L. Officer, M. K. Nazeeruddin, M. Grätzel. *ChemPhysChem* **6**, 1253 (2005).

[55] W. M. Campbell, K. W. Jolley, P. Wagner, K. Wagner, P. J. Walsh, K. C. Gordon, L. Schmidt-Mende, M. K. Nazeeruddin, Q. Wang, M. Grätzel, D. L. Officer. *The Journal of Physical Chemistry C* **111**, 11760 (2007).

[56] T. Komori, Y. Amao. *J. Porphyr. Phthalocya.* **07**, 131 (2003).

[57] K. Hara, Z. Wang, T. Sato, A. Furube, R. Katoh, H. Sugihara, Y. Dan-oh, C. Kasada, A. Shinpo, S. Suga. *J. Phys. Chem. B* **109**, 15476 (2005).

[58] A. Burke, L. Schmidt-Mende, S. Ito, M. Grätzel. *Chem. Commun.* **3**, 234 (2007).

[59] T. Horiuchi, H. Miura, K. Sumioka, S. Uchida. *J. Am. Chem. Soc.* **126**, 12218 (2004).

[60] Y. Chen, C. Li, Z. Zeng, W. Wang, X. Wang, B. Zhang. *J. Mater. Chem.* **15**, 1654 (2005).

[61] K. R. J. Thomas, J. T. Lin, Y. Hsu, K. Ho. *Chem. Commun.* **32**, 4098 (2005).

[62] K. Hara, M. Kurashige, S. Ito, A. Shinpo, S. Suga, K. Sayama, H. Arakawa. *Chem. Commun.* **2**, 252 (2003).

[63] S. Ardo, G. J. Meyer. *Chem. Soc. Rev.* **38**, 115 (2009).

[64] K. Hara, T. Horiguchi, T. Kinoshita, K. Sayama, H. Arakawa. *Sol. Energy Mater. Sol. Cells* **70**, 151 (2001).

[65] V. Thavasi, V. Renugopalakrishnan, R. Jose, S. Ramakrishna. *Mat. Sci. Eng. R* **63**, 81 (2009).

[66] M. Thomalla, H. Tributsch. *C. R. Chim.* **9**, 659 (2005).

[67] A. Barkschat, T. Moehl, B. Macht, H. Tributsch. *Int. J. Photoenergy* **2008**, 1 (2008).

[68] T. Dittrich, B. Neumann, H. Tributsch. *J. Phys. Chem. C* **111**, 2265 (2007).

[69] H. Tributsch. *Coord. Chem. Rev.* **248**, 1511 (2004).

[70] M. K. Nazeeruddin, R. Humphry-Baker, P. Liska, M. Grätzel. *J. Phys. Chem. B* **107**, 8981 (2003).

[71] R. Grunwald, H. Tributsch. *J. Phys. Chem. B* **101**, 2564 (1997).

[72] B. Macht, M. Turrion, A. Barkschat, P. Salvador, K. Ellmer, H. Tributsch. *Sol. Energy Mater. Sol. Cells* **73**, 163 (2002).

[73] V. K. Thorsmølle, G. Rothenberger, D. Topgaard, J. C. Brauer, D. Kuang, S. M. Zakeeruddin, B. Lindman, M. Grätzel, J. Moser. *ChemPhysChem* **12**, 145 (2011).

[74] W. Kubo, K. Murakoshi, T. Kitamura, S. Yoshida, M. Haruki, K. Hanabusa, H. Shirai, Y. Wada, S. Yanagida. *J. Phys. Chem. B* **105**, 12809 (2001).

[75] M. Junghänel, H. Tributsch. *Photoelectric Solar Cell Comprising a Electrolyte Film and Method for the Production thereof.* WO/2007/107149 (2007).

[76] N. Papageorgiou, W. F. Maier, M. Grätzel. *J. Electrochem. Soc.* **144**, 876 (1997).

[77] E. Olsen, G. Hagen, S. E. Lindquist. *Sol. Energy Mater. Sol. Cells* **63**, 267 (2000).

[78] T. N. Murakami, M. Grätzel. *Inorg. Chim. Acta* **361**, 572 (2008).

[79] T. N. Murakami, S. Ito, Q. Wang, M. K. Nazeeruddin, T. Bessho, I. Cesar, P. Liska, R. Humphry-Baker, P. Comte, P. Péchy, M. Grätzel. *J. Electrochem. Soc.* **153**, A2255 (2006).

[80] A. Hagfeldt, G. Boschloo, L. Sun, L. Kloo, H. Pettersson. *Chem. Rev.* **110**, 6595 (2010).

[81] H. J. Snaith, A. J. Moule, C. Klein, K. Meerholz, R. H. Friend, M. Grätzel. *Nano Lett.* **7**, 3372 (2007).

[82] M. Wang, N. Chamberland, L. Breau, J. Moser, R. Humphry-Baker, B. Marsan, S. M. Zakeeruddin, M. Grätzel. *Nat. Chem.* **2**, 385 (2010).

[83] L. Schmidt-Mende, S. M. Zakeeruddin, M. Grätzel. *Appl. Phys. Lett.* **86**, 013504 (2005).

[84] F. Fabregat-Santiago, J. Bisquert, L. Cevey, P. Chen, M. Wang, S. M. Zakeeruddin, M. Grätzel. *J. Am. Chem. Soc.* **131**, 558 (2009).

[85] L. M. Peter. *Acc. Chem. Res.* **42**, 1839 (2009).

[86] K. Lobato, L. M. Peter. *J. Phys. Chem. B* **110**, 21920 (2006).

[87] P. Salvador, M. G. Hidalgo, A. Zaban, J. Bisquert. *J. Phys. Chem. B* **109**, 15915 (2005).

[88] J. R. Jennings, A. Ghicov, L. M. Peter, P. Schmuki, A. B. Walker. *J. Am. Chem. Soc.* **130**, 13364 (2008).

[89] G. Schlichthörl, S. Y. Huang, J. Sprague, A. J. Frank. *J. Phys. Chem. B* **101**, 8141 (1997).

[90] G. Schlichthörl, N. G. Park, A. J. Frank. *J. Phys. Chem. B* **103**, 782 (1999).

[91] L. M. Peter, K. G. U. Wijayantha. *Electrochem. Commun.* **1**, 576 (1999).

[92] J. Bisquert, A. Zaban, M. Greenshtein, I. Mora-Seró. *J. Am. Chem. Soc.* **126**, 13550 (2004).

[93] E. Hendry, M. Koeberg, B. O'Regan, M. Bonn. *Nano Lett.* **6**, 755 (2006).

[94] M. Bailes, P. J. Cameron, K. Lobato, L. M. Peter. *J. Phys. Chem. B* **109**, 15429 (2005).

[95] N. W. Duffy, L. M. Peter, R. M. G. Rajapakse, K. G. U. Wijayantha. *J. Phys. Chem. B* **104**, 8916 (2000).

[96] L. M. Peter. *J. Phys. Chem. C* **111**, 6601 (2007).

[97] J. Nelson. *Phys. Rev. B* **59**, 15374 (1999).

[98] J. Bisquert, V. S. Vikhrenko. *J. Phys. Chem. B* **108**, 2313 (2004).

[99] L. Dloczik, O. Ileperuma, I. Lauermann, L. M. Peter, E. A. Ponomarev, G. Redmond, N. J. Shaw, I. Uhlendorf. *J. Phys. Chem. B* **101**, 10281 (1997).

[100] J. van de Lagemaat, A. J. Frank. *J. Phys. Chem. B* **104**, 4292 (2000).

[101] A. C. Fisher, L. M. Peter, E. A. Ponomarev, A. B. Walker, K. G. U. Wijayantha. *J. Phys. Chem. B* **104**, 949 (2000).

[102] S. Södergren, A. Hagfeldt, J. Olsson, S. Lindquist. *J. Phys. Chem.* **98**, 5552 (1994).

[103] F. Cao, G. Oskam, G. J. Meyer, P. C. Searson. *J. Phys. Chem.* **100**, 17021 (1996).

[104] K. Schwarzburg, F. Willig. *J. Phys. Chem. B* **103**, 5743 (1999).

[105] K. Kalyanasundaram, M. Grätzel. *Coord. Chem. Rev.* **177**, 347 (1998).

[106] B. O'Regan, J. Moser, M. Anderson, M. Grätzel. *J. Phys. Chem.* **94**, 8720 (1990).

[107] J. E. Moser, M. Grätzel. *Chem. Phys.* **176**, 493 (1993).

[108] S. A. Haque, Y. Tachibana, R. L. Willis, J. E. Moser, M. Grätzel, D. R. Klug, J. R. Durrant. *J. Phys. Chem. B* **104**, 538 (2000).

[109] S. A. Haque, Y. Tachibana, D. R. Klug, J. R. Durrant. *J. Phys. Chem. B* **102**, 1745 (1998).

[110] L. Kavan, M. Grätzel. *Electrochim. Acta* **40**, 643 (1995).

[111] F. Pichot, B. A. Gregg. *J. Phys. Chem. B* **104**, 6 (2000).

[112] P. J. Cameron, L. M. Peter. *J. Phys. Chem. B* **107**, 14394 (2003).

[113] B. A. Gregg, F. Pichot, S. Ferrere, C. L. Fields. *J. Phys. Chem. B* **105**, 1422 (2001).

[114] B. A. Gregg. In *Semiconductor photochemistry and photophysics*, edited by V. Ramamurthy, K. S. Schanze, volume 10 of *Molecular and Supramolecular Photochemistry*, p. 51. CRC Press (2003).

[115] R. Memming. *Prog. Surf. Sci.* **17**, 7 (1984).

[116] R. A. Marcus. *J. Chem. Phys.* **24**, 966 (1956).

[117] R. Memming. *Semiconductor Electrochemistry.* Wiley-VCH, Weinheim (2001).

[118] H. Gerischer. *Z. Phys. Chem.* **26**, 223 (1960).

[119] H. Gerischer. In *Electrochemistry*, edited by H. Eyring, D. Henderson, W. Jost, volume IX A of *Physical Chemistry*, p. 463. Academic Press, New York (1970).

[120] A. J. Bard, L. R. Faulkner. *Electrochemical Methods: Fundamentals and Applications*. John Wiley & Sons, New York, 2nd edition (2001).

[121] R. Memming. *Electroanalytical Chemistry: A Series of Advances*, volume 11. Dekker, New York (1976).

[122] E. M. J. Johansson, M. Hedlund, H. Siegbahn, H. Rensmo. *J. Phys. Chem. B* **109**, 22256 (2005).

[123] E. M. J. Johansson, T. Edvinsson, M. Odelius, D. P. Hagberg, L. Sun, A. Hagfeldt, H. Siegbahn, H. Rensmo. *J. Phys. Chem. C* **111**, 8580 (2007).

[124] N. Papageorgiou, M. Grätzel, P. P. Infelta. *Sol. Energy Mater. Sol. Cells* **44**, 405 (1996).

[125] Y. Liu, A. Hagfeldt, X. Xiao, S. Lindquist. *Sol. Energy Mater. Sol. Cells* **55**, 267 (1998).

[126] A. Hauch, A. Georg. *Electrochim. Acta* **46**, 3457 (2001).

[127] N. Papageorgiou, Y. Athanassov, M. Armand, P. Bonhote, H. Pettersson, A. Azam, M. Grätzel. *J. Electrochem. Soc.* **143**, 3099 (1996).

[128] N. Agmon. *Chem. Phys. Lett.* **244**, 456 (1995).

[129] C. J. T. Grotthuss. *Ann. Chim.* **58**, 54 (1806).

[130] R. Kawano, M. Watanabe. *Chem. Commun.* **3**, 330 (2003).

[131] I. Jerman, V. Jovanovski, A. S. Vuk, S. Hocevar, M. Gaberscek, A. Jesih, B. Orel. *Electrochim. Acta* **53**, 2281 (2008).

[132] S. Licht. *Sol. Energy Mater. Sol. Cells* **38**, 305 (1995).

[133] S. Pelet, J. Moser, M. Grätzel. *J. Phys. Chem. B* **104**, 1791 (2000).

[134] J. N. Clifford, E. Palomares, M. K. Nazeeruddin, M. Grätzel, J. R. Durrant. *J. Phys. Chem. C* **111**, 6561 (2007).

[135] G. Boschloo, A. Hagfeldt. *Acc. Chem. Res.* **42**, 1819 (2009).

[136] A. F. Nogueira, M. D. Paoli, I. Montanari, R. Monkhouse, J. Nelson, J. R. Durrant. *J. Phys. Chem. B* **105**, 7517 (2001).

[137] C. Bauer, G. Boschloo, E. Mukhtar, A. Hagfeldt. *J. Phys. Chem. B* **106**, 12693 (2002).

[138] I. Montanari, J. Nelson, J. R. Durrant. *J. Phys. Chem. B* **106**, 12203 (2002).

[139] A. Y. Anderson, P. R. F. Barnes, J. R. Durrant, B. C. O'Regan. *J. Phys. Chem. C* **114**, 1953 (2010).

[140] A. Hagfeldt, M. Grätzel. *Acc. Chem. Res.* **33**, 269 (2000).

[141] S. N. Mori, W. Kubo, T. Kanzaki, N. Masaki, Y. Wada, S. Yanagida. *J. Phys. Chem. C* **111**, 3522 (2007).

[142] P. R. F. Barnes, A. Y. Anderson, S. E. Koops, J. R. Durrant, B. C. O'Regan. *J. Phys. Chem. C* **113**, 1126 (2009).

[143] H. K. Dunn, L. M. Peter. *J. Phys. Chem. C* **113**, 4726 (2009).

[144] A. Zaban, M. Greenshtein, J. Bisquert. *ChemPhysChem* **4**, 859 (2003).

[145] A. B. Walker, L. M. Peter, K. Lobato, P. J. Cameron. *J. Phys. Chem. B* **110**, 25504 (2006).

[146] J. Bisquert, F. Fabregat-Santiago, I. Mora-Seró, G. Garcia-Belmonte, S. Giménez. *J. Phys. Chem. C* **113**, 17278 (2009).

[147] L. M. Peter. *Phys. Chem. Chem. Phys.* **9**, 2630 (2007).

[148] J. P. Gonzalez-Vazquez, J. A. Anta, J. Bisquert. *J. Phys. Chem. C* **114**, 8552 (2010).

[149] F. Fabregat-Santiago, J. Bisquert, G. Garcia-Belmonte, G. Boschloo, A. Hagfeldt. *Sol. Energy Mater. Sol. Cells* **87**, 117 (2005).

[150] F. Fabregat-Santiago, I. Mora-Seró, G. Garcia-Belmonte, J. Bisquert. *J. Phys. Chem. B* **107**, 758 (2003).

[151] D. J. Fitzmaurice, H. Frei. *Langmuir* **7**, 1129 (1991).

[152] J. van de Lagemaat, N. Park, A. J. Frank. *J. Phys. Chem. B* **104**, 2044 (2000).

[153] B. C. O'Regan, K. Bakker, J. Kroeze, H. Smit, P. Sommeling, J. R. Durrant. *J. Phys. Chem. B* **110**, 17155 (2006).

[154] S. Ito, P. Liska, P. Comte, R. Charvet, P. Péchy, U. Bach, L. Schmidt-Mende, S. M. Zakeeruddin, A. Kay, M. K. Nazeeruddin, M. Grätzel. *Chem. Commun.* **34**, 4351 (2005).

[155] P. M. Sommeling, B. C. O'Regan, R. R. Haswell, H. J. P. Smit, N. J. Bakker, J. J. T. Smits, J. M. Kroon, J. A. M. van Roosmalen. *J. Phys. Chem. B* **110**, 19191 (2006).

[156] J. N. Hart, D. Menzies, Y. Cheng, G. P. Simon, L. Spiccia. *C. R. Chim.* **9**, 622 (2005).

[157] S. Gledhill, A. Grimm, N. Allsop, T. Köhler, C. Camus, M. Lux-Steiner, C. Fischer. *Thin Solid Films* **517**, 2309 (2009).

[158] R. B. Peterson, C. L. Fields, B. A. Gregg. *Langmuir* **20**, 5114 (2004).

[159] J. Tornow, K. Schwarzburg. *J. Phys. Chem. C* **111**, 8692 (2007).

[160] C. Swiatkowski, A. Sanders, K.-D. Buhre, M. Kunst. *J. Appl. Phys.* **78**, 1763 (1995).

[161] M. Kunst, G. Beck. *J. Appl. Phys.* **60**, 3558 (1986).

[162] K.-M. Schindler, M. Kunst. *J. Phys. Chem.* **94**, 8222 (1990).

[163] L. Han, N. Koide, Y. Chiba, A. Islam, R. Komiya, N. Fuke, A. Fukui, R. Yamanaka. *Appl. Phys. Lett.* **86**, 213501 (2005).

[164] Q. Wang, J. Moser, M. Grätzel. *J. Phys. Chem. B* **109**, 14945 (2005).

[165] J. Bisquert, G. Garcia-Belmonte, F. Fabregat-Santiago, N. S. Ferriols, P. Bogdanoff, E. C. Pereira. *J. Phys. Chem. B* **104**, 2287 (2000).

[166] J. Bisquert, M. Grätzel, Q. Wang, F. Fabregat-Santiago. *J. Phys. Chem. B* **110**, 11284 (2006).

[167] F. Fabregat-Santiago, J. Bisquert, E. Palomares, L. Otero, D. Kuang, S. M. Zakeeruddin, M. Grätzel. *J. Phys. Chem. C* **111**, 6550 (2007).

[168] F. Fabregat-Santiago, G. Garcia-Belmonte, J. Bisquert, A. Zaban, P. Salvador. *J. Phys. Chem. B* **106**, 334 (2002).

[169] F. Fabregat-Santiago, J. Bisquert, E. Palomares, S. A. Haque, J. R. Durrant. *J. Appl. Phys.* **100**, 034510 (2006).

[170] J. Bisquert. *Phys. Chem. Chem. Phys.* **5**, 5360 (2003).

[171] F. Fabregat-Santiago, H. Randriamahazaka, A. Zaban, J. Garcia-Cañadas, G. Garcia-Belmonte, J. Bisquert. *Phys. Chem. Chem. Phys.* **8**, 1827 (2006).

[172] M. Turrión, B. Macht, P. Salvador, H. Tributsch. *Z. Phys. Chem.* **212**, 51 (1999).

[173] A. Barkschat. *Bildgebende elektrochemische Untersuchungen an Grenzflächen mit metallzentrierten Elektronenübertragungen.* Ph.D. thesis, FU Berlin (2003).

[174] M. Kunst, F. Goubard, C. Colbeau-Justin, F. Wünsch. *Mater. Sci. Eng., C* **27**, 1061 (2007).

[175] B. C. O'Regan, J. R. Durrant, P. M. Sommeling, N. J. Bakker. *J. Phys. Chem. C* **111**, 14001 (2007).

[176] P. J. Cameron, L. M. Peter. *J. Phys. Chem. B* **109**, 7392 (2005).

[177] B. C. O'Regan, S. Scully, A. C. Mayer, E. Palomares, J. Durrant. *J. Phys. Chem. B* **109**, 4616 (2005).

[178] C. He, L. Zhao, Z. Zheng, F. Lu. *J. Phys. Chem. C* **112**, 18730 (2008).

[179] J. Bisquert. *J. Phys. Chem. C* **111**, 17163 (2007).

[180] A. M. Peiró, C. Colombo, G. Doyle, J. Nelson, A. Mills, J. R. Durrant. *J. Phys. Chem. B* **110**, 23255 (2006).

[181] Y. Tamaki, A. Furube, M. Murai, K. Hara, R. Katoh, M. Tachiya. *J. Am. Chem. Soc.* **128**, 416 (2006).

[182] G. Boschloo, L. Häggman, A. Hagfeldt. *J. Phys. Chem. B* **110**, 13144 (2006).

[183] J. Sun, D. M. Stanbury. *Inorg. Chem.* **37**, 1257 (1998).

[184] R. M. Nielson, G. E. McManis, L. K. Safford, M. J. Weaver. *J. Phys. Chem.* **93**, 2152 (1989).

[185] R. M. Penner, M. J. Heben, T. L. Longin, N. S. Lewis. *Science* **250**, 1118 (1990).

[186] A. N. M. Green, R. E. Chandler, S. A. Haque, J. Nelson, J. R. Durrant. *J. Phys. Chem. B* **109**, 142 (2005).

[187] J. E. Kroeze, T. J. Savenije, J. M. Warman. *J. Am. Chem. Soc.* **126**, 7608 (2004).

[188] R. Katoh, A. Huijser, K. Hara, T. J. Savenije, L. D. A. Siebbeles. *J. Phys. Chem. C* **111**, 10741 (2007).

[189] T. Tiedje, A. Rose. *Solid State Commun.* **37**, 49 (1981).

[190] M. Kunst, R. Schwarz. In *Recent research developments in science and technology of semiconductors*, edited by S. G. Pandalai, volume 1, pp. 93–110. Trivandrum, Kerala, India (2002).

[191] K. Keis, E. Magnusson, H. Lindström, S. Lindquist, A. Hagfeldt. *Sol. Energy Mater. Sol. Cells* **73**, 51 (2002).

[192] M. Law, L. E. Greene, J. C. Johnson, R. Saykally, P. Yang. *Nat. Mater.* **4**, 455 (2005).

[193] K. Tennakone, G. R. R. A. Kumara, I. R. M. Kottegoda, V. P. S. Perera. *Chem. Commun.* **1**, 15 (1999).

[194] K. Kakiuchi, E. Hosono, S. Fujihara. *J. Photoch. Photobio. A* **179**, 81 (2006).

[195] H. Rensmo, K. Keis, H. Lindström, S. Södergren, A. Solbrand, A. Hagfeldt, S. Lindquist, L. N. Wang, M. Muhammed. *J. Phys. Chem. B* **101**, 2598 (1997).

[196] K. Keis, J. Lindgren, S. Lindquist, A. Hagfeldt. *Langmuir* **16**, 4688 (2000).

List of Abbreviations

AM1.5G	Air Mass 1.5 Global
CB	Conduction Band
dcbpy	4,4'-dicarboxylic acid-2,2'-bipyridine
DSC	Dye-Sensitized Solar Cell
DSL18NR-AO	Titania paste from Dyesol containing both ∼20 nm and ∼400 nm particles
DSL18NR-T	Titania paste from Dyesol containing ∼20 nm particles
FTO	Fluor-doped Tin Oxide, F:SnO_2
FWHM	Full Width at Half Maximum
HOMO	Highest Occupied Molecular Orbital
IPCE	Incident Photon-to-Electrical Conversion Efficiency
IR	Infrared
IS	Impedance Spectroscopy
ITO	Indium-doped Tin Oxide, In:SnO_2
I-V	Current-Voltage
LUMO	Lowest Unoccupied Molecular Orbital
MLCT	Metal-to-Ligand Charge Transfer
N3	*cis*-bis(isothiocyanato)*bis*(2,2'-bipyridyl-4,4'-dicarboxylato)ruthenium(II)
N719	*cis*-di(thiocyanato)*bis*(2,2'-bipyridyl-4,4'-dicarboxylate)ruthenium(II)bis(tetrabutylammonium)

N749	tri(thiocyanato)(2,2':6',6"-terpyridyl-4,4'4"-tricarboxylate)ruthenium(II)tris(tetrabutylammonium) ("black dye")
NSCSC	Nano Surface Conductivity Solar Cell
OD	Optical Density
P25	Comercially available titanium dioxide powder (Degussa)
PET	Polyethylene
PI	Polyimide
PV	Photovoltaics
RT	Room Temperature
SMSC	Scanning Microscope for Semiconductor Characterization
TCO	Transparent Conducting Oxide
TiO_2	Titanium dioxide
TRMC	Time Resolved Microwave Conductivity
UV	Ultraviolet
VB	Valence Band
Z907	*cis*-di(thiocyanato)(2,2'-bipyridyl-4,4'-dicarboxylate)-(2,2'-bipyridyl-4,4'-dinonyl)-ruthenium(II)
ZnO	Zink oxide

List of Symbols

Symbol	Term	Units
α	Absorption coefficient	cm^{-1}
A_{10ns}	Amplitude of the TRMC signal	
C_μ	Chemical capacitance	F/cm^2
d	Thickness	μm
D_0	Free electron diffusion coefficient	cm^2s^{-1}
D_n	Effective electron diffusion coefficient	cm^2s^{-1}
D^+	Oxidized state of the dye	
D^*	Excited state of the dye	
E	Energy	eV
E_C	Conduction band energy	eV
E_{VB}	Valence band energy	eV
E_F	Fermi energy	eV
$E_{F,redox}$	Fermi level in the electrolyte	eV
${}_nE_F$	Quasi-Fermi level of electrons in TiO_2	eV
e^-	Electron	
$e^-_{TiO_2}$	Electron in the conduction band of TiO_2	
η	Conversion efficiency	
η_{inj}	Injection efficiency	
η_{lh}	Light harvesting efficiency	
$f(E)$	Boltzman distribution function	
FF	Fill factor	

Symbol	Term	Units
$g(E)$	Density of states function	
h^+	Hole	
I_{OC}	Open circuit photocurrent	mA/cm^2
I_{SC}	Short circuit photocurrent	mA/cm^2
I_0	Irradiance (light "intensity")	W/m^2
J	Flux	$cm^{-2}s^{-1}$
J_{ph}	Photocurrent density	mA/cm^2
k	Reaction rate constant	
k_B	Boltzmann constant	eV/K
λ	Wavelength	nm
L_n	Diffusion length	cm
N_c	Density of conduction band states	cm^{-3}
n_c	Density of conduction band electrons	cm^{-3}
n_c^0	Density of conduction band electrons in the dark	cm^{-3}
N_t	Density of trap states	cm^{-3}
n_x	Concentration of species x	cm^{-3}
$\Delta P(t)$	Change of the reflected microwave power	
ϕ	Radiant flux	W/cm^2
P_{in}	Solar power input	W
P_{max}	Maximum power output	W
p	Porosity	
q	Elementary charge	C
R_{ct}	Charge-transfer resistance	Ω
R_{tr}	Electron-transport resistance	Ω
R^+	Oxidized redox species	
$\Delta S(t)$	Change of the photoconductance	
σ	Electrical conductivity	$\Omega^{-1}cm^{-1}$

Symbol	**Term**	**Units**
$\Delta\sigma(t)$	Photogenerated change of the conductivity	
τ_0	Free electron lifetime	s
τ_n	Effective electron lifetime	s
τ_{trans}	Electron transit time	s
T	Temperature	K
u_x	Mobility of species x	$\text{cm}^2\text{V}^{-1}\text{s}^{-1}$
U_{photo}	Photovoltage	V
μ	Electrochemical potential	J/mol
V_{OC}	Open circuit photovoltage	V
V_{SC}	Short circuit photovoltage	V

List of Figures

Curriculum Vitae

Dennis Friedrich

friedrich@helmholtz-berlin.de

Education

Dipl. Phys., December 2007
Technische Universität Berlin, Germany

Thesis: *Untersuchung der elektronischen Eigenschaften von bio-molekül-modifizierten Halbleiteroberflächen ("A study of the electronic properties of semiconductor-surfaces modified with bio-molecules")*

Advisers: Prof. H. Tributsch, Dr. M. Kunst

Research Experience

6/2008–5/2011	Ph.D. student, Helmholtz-Zentrum Berlin für Materialien und Energie and Freie Universität Berlin
2/2008–6/2008	Research Associate, Helmholtz-Zentrum Berlin für Materialien und Energie, Department Solar Energetics, Prof. H. Tributsch. Research in the area of (photo)-electrochemistry, solar energy and bionics.
5/2002–12/2007	Research Assistant, Hahn-Meitner Institute Berlin, Department Solar Energetics, Prof. H. Tributsch. Research in the area of solar energy conversion and bio-analogue systems.

Scholarships

6/2008–5/2011	Doctoral program of the Deutsche Bundesstiftung Umwelt (DBU).